Efficient nonlinear compression of a high-power Yb:YAG oscillator to the sub-10 fs regime and its applications

Gaia Barbiero

München 2021

Efficient nonlinear compression of a high-power Yb:YAG oscillator to the sub-10 fs regime and its applications

Gaia Barbiero

Dissertation
an der Fakultät für Physik
der Ludwig–Maximilians–Universität
München

vorgelegt von
Gaia Barbiero
aus Segrate (MI), Italien

München, den 01.07.2021

Erstgutachter: Prof. Dr. Matthias F. Kling

Zweitgutachter: Dr. Hanieh Fattahi

Tag der mündlichen Prüfung: 23.09.2021

Zusammenfassung

Der Fortschritt in der Femtosekunden- und Attosekundenspektroskopie hängt unter anderem von der Verfügbarkeit von ultrakurzen Pulsen mit hoher Spitzen- und Durchschnittsleistung ab, da hiermit die Bandbreite erweitert sowie die Detektionsempfindlichkeit verbessert werden kann. Darüber hinaus sind Quellen mit hoher Wiederholrate vorteilhaft, um das Signal-zu-Rausch Verhältnis zu erhöhen und die Zeit für die Datenerfassung zu reduzieren. Heutzutage sind Yb:YAG basierte Laserquellen in der Lage, Pulse mit hoher Spitzenleistung direkt aus einem Oszillator zu erzeugen, mit deutlich höherer Ausgangsleistung als beispielsweise in Ti:Saphir basierten Quellen. Demgegenüber stehen jedoch die schmalen Emissionsquerschnitte von Yb:YAG, welche den direkten Einsatz in der ultraschnellen Spektroskopie begrenzen.

Diese Dissertation behandelt die Entwicklung und die Anwendung von effizienten, mehrstufigen, nichtlinearen Kompressions-Konzepten, mit welchen sub-10 fs Pulse aus einem Yb:YAG Dünnscheiben basierten, Kerr-Linsen modengekoppelten Oszillator erzeugt werden.

Der verwendete Oszillator erzeugt Pulse mit einer Wiederholrate von 16 MHz, einer Pulsdauer von 220 fs, einer zentralen Wellenlänge von 1030 nm sowie einer Energie von 6.3 µJ. Eine nichtlineare Kompressionsstufe, basierend auf dem mehrfachen Durchgang durch eine abbildende, Herriott-artige Anordnung, verkürzt die Oszillatorpulse zunächst auf unter 20 fs. Derartig kurze Pulse mit hoher Durchschnittsleistung sind vorteilhaft für Experimente mit nichtlinearer Frequenzumwandlung. Dies wurde zum Beispiel durch die Erzeugung von intensiver und breitbandiger Terahertzstrahlung mit Hilfe der optischen Gleichrichtung in Galliumphosphid Kristallen demonstriert.

Des Weiteren wurden zwei verschiedene Ansätze untersucht, um die Pulsdauer auf unter 10 fs zu verkürzen. Der erste Ansatz nutzt eine gasgefüllte Einzelring, Hohlkern, phototonische Kristallfaser, um Pulse mit einer Dauer von 9 fs zu erzeugen. Aufgrund der begrenzten Stabilität dieses ersten Ansatzes verfolgt der zweite Ansatz eine alternative Kompressionsstufe, welche auf der Selbstfokussierung in dünnen Saphirscheiben als Quasi-Wellenleiter basiert. Mit dieser vollständig auf Festkörpern basierten Kompression wurden Pulse mit hoher Leistung und einer Dauer von 8.5 fs erzeugt. Die Nutzbarkeit dieser intensiven Pulse und die Zuverlässigkeit der Kompression mittels Saphirscheiben wurde demonstriert, indem ultra-breitbandige Strahlung im mittleren Infrarot mit Hilfe der Intra-Puls Differenzfrequenzerzeugung in Lithiumjodat generiert wurde.

Das entwickelte, kompakte und zuverlässige Lasersystem für ultrakurze Pulse mit hoher Leistung, welches intensive Pulse über einen Bereich von der sichtbaren Strahlung bis zur Terahertzstrahlung mit Megahertz Wiederholrate erzeugen kann, ist ideal für die verschiedensten Anwendungen in der ultraschnellen Spektroskopie geeignet.

Abstract

Advancements in femtosecond and attosecond spectroscopy benefit directly from the availability of ultrashort pulses at high peak and average power to extend the bandwidth coverage and to enhance the detection sensitivity. Moreover, sources at high repetition rate are desirable to increase the signal-to-noise ratio and reduce data acquisition time. Nowadays, Yb:YAG-based lasers sources are capable of delivering pulses at high peak power directly from the oscillator, with much higher output power compared to Ti:Sapphire-based sources. However, the narrowband emission cross-section of Yb:YAG limits their direct applicability for ultrafast spectroscopy.

This thesis describes experimental work in the development and in the applications of an efficient, multi-stage nonlinear compression scheme to reach sub-10 fs pulses from an Yb:YAG, thin-disk, Kerr-lens mode-locked oscillator.

The oscillator, operating at 16 MHz, delivers 220 fs-long pulses with central wavelength 1030 nm and 6.3 µJ energy. A nonlinear compression stage, based on multipass imaging cells in Herriott type configuration, is used to efficiently reduce the pulse duration of the source to sub-20 fs. The high average power combined with the short pulse duration of this frontend greatly benefits nonlinear frequency conversion, which was demonstrated by the generation of intense and broadband terahertz radiation via optical rectification in gallium phosphide crystals.

Additionally, two different approaches are investigated for the further compression towards the sub-10 fs regime. Firstly, a gas-filled, single-ring, hollow-core photonic crystal fiber is used to generate pulses with a pulse duration of 9 fs. Secondly, due to the limited stability of the previous approach an alternative compression stage based on self-focusing in a quasi-waveguide of sapphire thin plates is developed. With this all-bulk based compression, high-power, 8.5 fs-long pulses are obtained. The advantage of these intense pulses and the reliability of the frontend with the thin-plate compression setup are demonstrated by the generation of intense, ultra-broadband mid-infrared radiation via intra-pulse difference-frequency generation in lithium iodate crystals.

The compact and reliable high-power ultrashort laser system able to generate intense pulses from visible to terahertz range at megahertz repetition rate holds the promise to pave the way towards many different ultrafast spectroscopic applications.

Contents

List of Figures

List of Tables

List of Abbreviations

AR	anti-reflective
BBO	beta barium borate β-$Ba(BO_2)_2$
CEP	carrier-envelope phase
CM	chirped mirrors
DFG	difference-frequency generation
EOS	electro-optic sampling
FTL	Fourier transform limited
FWHM	full-width-at-half-maximum
GDD	group delay dispersion
HD	high-dispersive
HR	high-reflective
KLM	Kerr-lens mode-locking
$LiIO_3$	Lithium iodate
MIR	mid-infrared
MPC	multipass imaging cell
Nd:YAG	neodymium-doped yttrium aluminum garnet
NLSE	nonlinear Schrödinger equation
OPA	optical parametric amplification
OR	optical rectification
PCF	photonic crystal fibers
RMS	root mean square
ROC	radius of curvature
SESAM	semiconductor saturable absorber mirrors
SF	self focusing
SFG	sum-frequency generation
SH-FROG	second-harmonic frequency-resolved optical gating
SHG	second-harmonic generation
SPM	self-phase modulation
SVEA	slowly varying envelope approximation
TD	thin-disk
Ti:Sa	titanium-doped sapphire
Yb:YAG	ytterbium-doped yttrium aluminum garnet

1 Introduction

Since its first demonstration by Theodore Maiman in 1960 [1], laser sources became essential tools for exploring the fundamental constituents of nature. Nowadays, the study of light-matter interaction is a powerful way to explore the world around us: from the study of the macroscopic universe, as in LIGO's laser interferometer [2], to the study of microscopic bio-chemical processes in the human body [3, 4], even further to study the motion of electrons and atomic nuclei, as in femtochemisty and attosecond metrology [5].

The invention of Kerr-lens mode-locking (KLM) [6] in combination with titanium-doped sapphire (Ti:Sa) as gain medium [7] was a milestone for lasers in the femtosecond regime. The Ti:Sa gain medium, with its uniquely broadband emission bandwidth in the visible spectral region, is nowadays the working horse for many applications [8]. While Ti:Sa-based laser systems routinely deliver pulse durations well below 100 fs, they are typically limited to few watts in average power. Chirped-pulse amplification opened the way to increase the energy and, hence, the average power of these sources to an unprecedented frontier. However, with this approach only a limited repetition rate, in the kilohertz regime, can be achieved due to the damage threshold of the optical components [9].

Femtosecond and attosecond spectroscopy benefit directly from the availability of ultrashort, high-power lasers at megahertz repetition rates [10]. High repetition rates allow decreasing the measurement's acquisition time and thus enhancing the signal-to-noise ratio. Moreover, efficient extension of the spectral bandwidth of those sources to beyond one octave paves the way for novel broadband spectroscopy techniques, such as molecular fingerprinting [3] or femtosecond fieldoscopy [11] or THz spectroscopy [12, 13].

Yb-based laser systems can reach many hundreds of watts in average power at megahertz repetition rate [14–16], but they are limited to pulse durations of several hundreds of femtoseconds by their gain bandwidth [17]. However, highly nonlinear applications rely on ultrashort pulses durations and would benefit from the higher power and

higher repetition rate, enabled by Yb-based laser systems [18]. This applications includes: single-pass [19] or resonator-enhanced [20] high-harmonic generation [21], THz [12] and MIR generation [3].

Among other Yb-based systems, a novel class of lasers able to deliver short, high-peak power pulses in the MHz regime has gained importance in the recent years: KLM ytterbium-doped yttrium aluminum garnet (Yb:YAG) thin-disk (TD) oscillators. With this technology, pulses with average power above 100 W and pulse duration below 200 fs are obtained directly from oscillators without the involvement of any external amplification [22]. From this perspective, these lasers represent a unique class, combining high peak and high average powers in a relatively compact setup [8]. However, the pulse duration of KLM TD-oscillators is limited by the narrowband emission cross-section of Yb:YAG [23].

For high-power laser systems employing Yb-doped gain medium, a route to shorter pulse durations, which are not supported by the gain bandwidth, is nonlinear pulse compression in a medium with $\chi^{(3)}$ nonlinearity [18]. Nonlinear pulse compression setups suitable for high average power lasers can be distinguished by the nonlinear media: dielectric materials and noble gases, which are suitable for different pulse energies and peak power regimes [24].

For laser systems with low pulse energy, dielectric materials and especially fused silica have been extensively used as nonlinear media for spectral broadening. For moderate peak powers, in the order of few megawatts, exceptional results have been demonstrated with fibers [25, 26] and passive waveguides [20, 27–29]. The main limitation for the peak power scaling of these schemes is catastrophic self-focusing, which occurs at around 4 MW in the case of fused silica. Pulses with higher pulse energies, typically above 100 µJ, are commonly compressed in gas-filled hollow-core capillaries [30]. Here, the medium is a noble gas, which exhibits approximately three orders of magnitude higher threshold for catastrophic self-focusing. For moderate pulse energies and high peak powers, in the range between 5 µJ to 100 µJ, with tens of megawatts peak power, compression with neither scheme is possible. In recent years, much effort has been made to upscale dielectric-based schemes and to downscale noble gas-based schemes [24].

To downscale pulse compression in noble gases, gas-filled hollow-core Kagome and single-ring photonic crystal fibers (PCF) are promising approaches. These types of fibers allow smaller core diameters than capillaries and have been used to demonstrate nonlinear pulse compression in the aforementioned energy gap [31, 32]. Despite providing efficient pulse compression with excellent beam quality, fiber-based spectral broadening is

alignment sensitive and couples pointing-drifts to laser power fluctuations [33]. Moreover, photoionization in gas-filled hollow-core PCFs might limit their use in high-average power systems at high repetition rates [34, 35].

For upscaling dielectric-based pulse compression schemes, different concepts have been introduced. Firstly, splitting of the incident pulse, prior to the spectral broadening, into several copies with peak powers below the threshold for catastrophic self-focusing. After the nonlinear medium, all the copies are coherently re-combined [36]. However, this approach can result in complex and cumbersome optical setups. Secondly, nonlinear spectral broadening in a single bulk dielectric instead of waveguides has been demonstrated [37]. In this technique, the length of the nonlinear medium, the input beam diameter and divergence are precisely adjusted to avoid catastrophic self-focusing. However, this scheme suffers from beam quality degradation and spatially inhomogeneous spectral broadening. Therefore, the necessitary of spatial filtering limits the achievable optical efficiency. Thirdly, by passing through several nonlinear elements [38, 39]. In this scheme, catastrophic self-focusing is avoided by reducing the nonlinear phase shift in each element and carefully adjusting the input beam parameters. However, this scheme commonly relies on strong self-focusing and slight ionization of the bulk elements [38] and this compromises the beam quality and the homogeneity of the broadening as for a single-element approach [18].

In the recent years, a nonlinear pulse compression scheme relying on a waveguide-like periodic assembly consisting of focusing elements (concave dispersive mirrors) and nonlinear media was demonstrated [12, 17, 24, 33, 40]. This scheme, commonly called MPC mitigates the disadvantage of spatially inhomogeneous broadening by splitting the nonlinear phase shift into many steps with linear re-compression in between. MPCs are optically efficient compression schemes and are insensitive to fluctuations of the impinging beam pointing or profile [18]. These characteristics make MPCs especially suited for high-power operation and even for pulses with imperfect beam quality [41, 42]. Bulk- and gas-filled MPCs were, both, successfully implemented for high average and peak power regimes. Additionally, the robust design of this scheme allowed the rapid implementation for different frontends [12, 40, 43–47].

For KLM Yb:YAG TD oscillators many of these approaches have been employed to further extend the spectral bandwidth and overcome the main limitation of these unique class of frontends. Tab. 1.1 summarizes the achievements in nonlinear pulse compression for KLM TD Yb:YAG oscillators.

Kagomè PCF offered extreme temporal compression, to 3.5 fs Fourier-limit, in

two subsequent stages [48]. Nevertheless, this nonlinear pulse compression scheme suffered from the aforementioned instabilities already at moderate input peak power. The difficulty in beam in-coupling and the low damage threshold made this compression scheme a very challenging approach for power scaling at high repetition rate with KLM Yb:YAG systems [37].

Extreme efficiency was achieved in distributed waveguides [49]. In each pass the pulse is nonlinearly broadened in a fused silica plate and then re-compressed and re-collimated by a chirped curved mirror. Despite the high efficiency and the possibility to control the broadening in each pass, to achieve sufficient pulse compression, two stages each with 4 and 5 media, respectively, and intermediate re-compression were required. Due to the large amount of optical elements implemented in this approach, problems as errors in control of dispersion, degradation in the beam quality as well as sensitivity to misalignment can be encountered. This approach was able to deliver 32 fs pulses but for further compression a more versatile and compact scheme was required.

Broadening in multiple plates of bulk material [37, 50], proved to be a valuable alternative to reach 15 fs. However, the aforementioned problem about beam quality and the necessity of spatial filtering are present also in this approach with two stages each formed by a single bulk element and a compressor [37]. On contrary, MPCs offered a valid alternative and proved to be an efficient and robust compression scheme also for this type of frontends [33, 40]. However, the damage threshold of the optical elements and the control of linear dispersion limited this approach to the generation of 15 fs pulses. For lower pulse durations an approach without dispersive optics is required.

A novel class of hybrid nonlinear compression schemes, mixing different approaches in different compression stages, can benefit from the advantages of different techniques and also overcome their limitations. For this reason, and all the ones outlined above, the work in this thesis relies on the implementation of an efficient hybrid-nonlinear compression scheme to compress the over 200 fs-long pulses from a KLM Yb:YAG TD oscillator to the sub-10 fs regime. This allowed to use this novel source as reliable and ultra-broadband frontend for spectroscopic applications that benefited from the high repetition rate and the high intensity of the source.

Scheme	Average power [W]		Pulse duration [fs]		Peak power [MW]		Number of stages	Optical efficiency [%]
	In	Out	In	Out	In	Out		
Kagomè PCF [48]	50	20.5	250	3.5	4.8	143	2	41
Distributed waveguides [49]	155	147	170	32	48	251	2*	95
Multiple plates [37]	50	20	250	15	4.8	32.6	2	40
Multipass cells [33, 40]	100	45	220	16	15	94	3	45
This work	84	54	220	8.5	22.5	383.7	3	64

Table 1.1 Summary of different nonlinear compression schemes for Kerr-lens mode-locked Yb:YAG thin-disk oscillators. * indicates two stages each with 4 and 5 media, respectively.

Thesis outline

In this thesis, the temporal compression of 220 fs pulses from a 100 W Yb:YAG TD oscillator to sub-10 fs in a hybrid-nonlinear pulse compression scheme is presented. In the first broadening stage two consecutive MPCs are implemented to compress the pulse to 18 fs. In order to further extend the spectral bandwidth towards the few-cycles regime, two approaches are demonstrated. Firstly, a compression stage based on gas filled single-ring hollow-core PCF is developed. Due to the limitations encountered on the long term reliability of this particular broadening scheme, another compression scheme based on sapphire thin plates and relying on an improved version of the first broadening stage, able to reach sub-10 fs is also developed.

To prove the reliability of this system as frontend for experimental application, different studies are conducted. Firstly, broadband THz-radiation is generated and detected employing the first generation of the multipass-cell-based broadening. The relatively high power and the broad bandwidth of the generated THz pulses proved the beneficial effects of using an high power, oscillator as well as an efficient broadening scheme for spectroscopic applications. Consistently the high repetition rate of the source allowed efficient detection of small signals.

Another demonstration of the applicability of the system, especially of the stability of the all-bulk based compression scheme including two improved MPCs and the thin-plates frontend, was carried out. This novel frontend was able to efficiently generate 2-octave spanning pulses from $LiIO_3$.

The thesis is outlined among the chapters as following:

Chapter 2: the Yb:YAG TD KLM that served as frontend is presented and characterized.

Chapter 3: the development of the first generation of MPC-based frontend is outlined. The optical and opto-mechanical improvement that made possible the development of an improved generation of this compression scheme are also outlined and the results are discussed.

Chapter 4: is devoted to the development of a hybrid nonlinear compression scheme to reach the sub-10 fs regime. Firstly, the results obtained with the single-ring hollow-core PCF are presented. Secondly, the all-bulk based scheme relying on 4 sapphire plates is discussed.

Chapter 5: presents the results obtained in the generation of THz-radiation in gallium phosphide crystals and mid-infrared radiation in lithium iodate cystals.

Chapter 6: summarises the results and concludes the thesis with future developments and improvements.

2 Yb:YAG thin-disk fronted

In this chapter, a brief overview about the main properties of Yb:YAG TD KLM oscillators is outlined. Following, a detailed description and characterization of the experimental setup is given. For further reading, several excellent classical textbooks and review articles providing a thorough and insightful overview about solid-state lasers and their technological evolution can be found, some examples are [51, 52].

2.1 Theory

The laser system used as frontend for the experiments outlined in this thesis is a Yb:YAG TD KLM oscillator. As discussed in the introductory chapter 1, oscillators based on TD geometry represent, nowadays, the state-of-the-art of solid-state oscillators. These systems pose a valuable alternative to Ti:Sa lasers for spectroscopic applications thanks to their ability of delivering pulses with a duration of hundreds of femtoseconds at energies up to tens of microjoules with a repetition rate in the MHz range. The resulting peak power, on the order of several tens of MW, enables the utilization of nonlinear effects for extra-cavity spectral broadening, compensating the limited emission bandwidth of Yb:YAG, without the need of further amplification [37, 40, 49].

In the following paragraphs brief descriptions of the Yb:YAG gain material, the TD technology and the solitonic KLM are presented.

2.1.1 Yb:YAG gain material

The quantum defect, defined as the fractional difference of energy between absorbed pump photons and emitted laser photons $1 - \mathcal{E}_{\text{pump}}/\mathcal{E}_{\text{laser}}$, is the most influential parameter for heat production in a lasing material. For Yb^{3+} doped materials this parameter is

particularly low. As an example, the quantum defect for Yb:YAG is approximately 9 % and for neodymium-doped yttrium aluminum garnet (Nd:YAG) is approximately 24 %, which makes them suitable candidates for high-power solid-state lasers.

Among Yb^{3+}-doped materials, Yb:YAG is a quasi-three-level laser medium with a long upper-state lifetime, approximately 1 ms, and a maximum doping concentration near 10 % [53]. As shown in Fig. 2.1, Yb:YAG has a predominant emission line at 1030 nm with a bandwidth of approximately 8 nm corresponding to a Fourier transform limited (FTL) pulse duration of 140 fs, ignoring the effects of gain narrowing [54]. Two possible pumping lines are evident in the absorption spectrum of Yb:YAG: a broad absorption line at 940 nm (quantum defect $\approx$ 9 %) with full-width-at-half-maximum (FWHM) $\approx$ 18 nm and a zero-phonon line at 969 nm (quantum defect $\approx$ 6 %) with FWHM $\approx$ 3 nm. Although pumping the lasing material at a low quantum defect is desired for easier heat management, as explained earlier, the narrow absorption cross-section at 969 nm would require a costly laser diode with a stabilized emission wavelength. Instead, the absorption band at 940 nm has a sufficient spectral bandwidth to pump the lasing material with cost-effective industrial diode lasers [55].

For the mentioned reasons as well as the relatively broad bandwidth, the extremely low quantum defect, and the availability of cost-effective pump diodes, Yb:YAG is currently the work-horse for the development of high-power oscillators and amplifiers [56].

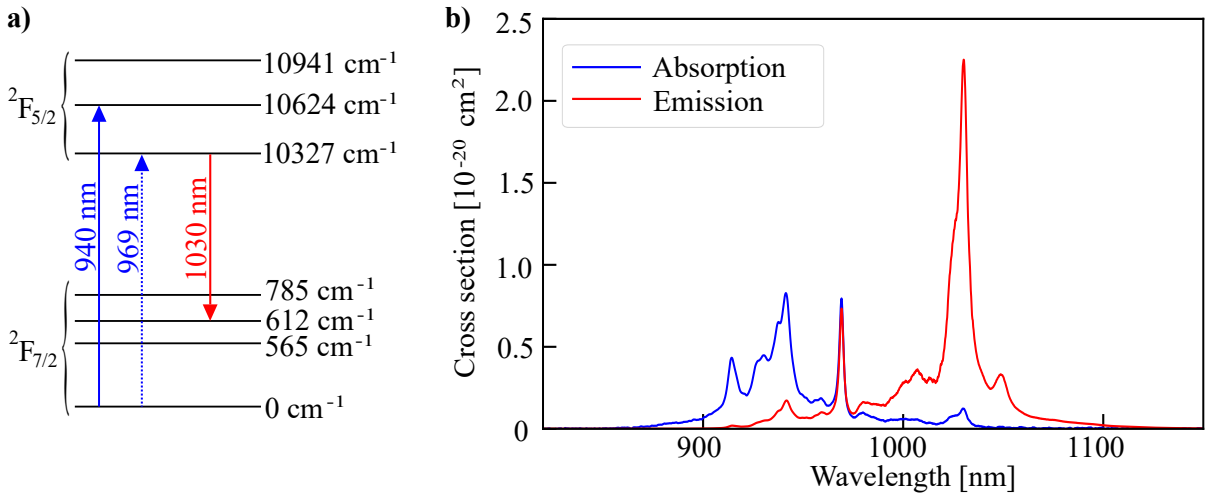

Figure 2.1 **a)** Energy level diagram of Yb^{3+} in yttrium aluminium garnet. **b)** Emission and absorption cross section of Yb:YAG at room temperature. Adapted from [23].

2.1.2 Thin-disk geometry

In the development and in the power scaling of solid-state lasers, thermal management has one of the strongest impacts. For this reason, in addition to the choice of the material itself, the geometry of the gain medium as well as the interaction with the cooling system are of great importance in the development of solid-state lasers. Intuitively, an efficient cooling geometry has a large ratio between cooling area and pumped volume. In this way, effects such as deterioration of beam quality due to temperature gradients, thermal lensing, thermal-dependent changes in the refractive index, depolarization caused by thermal-induced birefringence and other thermally-induced effects can be largely reduced. Numerous designs have been developed in this respect and Yb:YAG has been employed as gain medium in different geometries such as rod, slab, fiber and TD [51].

In 1994 Giesen et al. [57] introduced the TD geometry for an efficient cooling of the gain medium. This geometry relies on maximizing the ratio between surface and volume of the laser medium by shaping it as a thin cylindrical plate, Fig. 2.1.2a. Typically the thickness is 100 - 200 µm and the diameter is several mm. In order to minimize the gain losses, the front and the back surfaces of the disk have anti-reflective (AR) and high-reflective (HR) coating depositions for the spectral range of the seed and pump beams, respectively, as shown in Fig. 2.2b. The TD geometry is intended for pumping on a large area with inexpensive, high power laser diodes. To reach high pump absorption, the TD is placed in a customized structure with a multi-pass arrangement. In this structure the pump beam is re-imaged onto the disk by a combination of a parabolic mirror and prism retro-reflectors, resulting in absorption efficiencies as high as 90 %.

Not every material has proven to be suitable for the TD geometry, due to the high mechanical stress during high-power pumping and during the manufacturing of a thin but comparably large disk. The performance of Yb:YAG as gain material in the TD geometry is remarkable due to the efficient cooling of the gain medium and the high resistance to mechanical and thermal stress. Consequently, the combination of TD technology with the Yb:YAG material made possible the simultaneous scaling of average and peak power in both oscillators and amplifiers. It allowed to reach energies and average powers up to joule-level and kilowatt-level, respectively, while maintaining an almost diffraction-limited beam quality via tens of multi-passes through one or two disks [52, 54, 58, 59].

In terms of ultra-short pulse generation the thin-disk geometry has proven to be very beneficial [60]. Power scaling generally demands for large mode areas in a thin gain medium. These requirements also reduce nonlinear phase accumulation during the

generation of intense, short pulses. As a consequence, the thin gain medium greatly relaxes the demand on pre-chirping in regenerative amplifiers and enables more precise nonlinear-phase control in soliton mode-locked oscillators. Together with the excellent heat management, Yb:YAG thin-disk technology offers a particularly suited starting point for the generation of ultra-short pulses with high peak and average power.

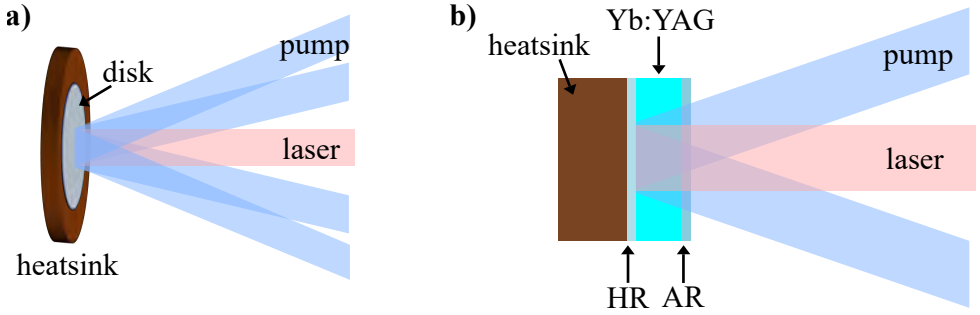

Figure 2.2 Thin-disk concept (not to scale). **a)** The heat sink is water cooled from the backside. The pump-light is folded and imaged several times onto the thin-disk to maximize the absorption. The laser emission is perpendicular to the disk. **b)** The gain material, Yb:YAG, has a HR coating on the back side and an AR coating on the front side to minimize the gain losses.

2.1.3 Soliton Kerr-lens mode-locking of resonating cavities

Laser pulses are formed inside the resonating cavity of an oscillator. In the simplest case it consists of two mirrors that trap light and shape the longitudinal and transversal modes. Between them a gain medium transfers power into the modes and replenishes losses, e.g. due to an output-coupler that transmits a portion of the circulating light. This simple scheme is suitable for the generation of continuous-wave laser radiation. Considerably shorter pulses are obtained with mode-locking. During mode-locking the oscillator can be forced to concentrate the energy of the circulating light into a short time window by modulation of the intra-cavity losses. This modulation can occur in different time scales. For a time scale longer than a round-trip time, q-switching methods are commonly used, which allow to reach pulse durations in the order of ns to µs. On the time scale of a round trip, switches and saturable absorbers are alternatively used to reach pulse durations in the order of hundreds of fs. Electro- or acousto-optical switches are used in active mode-locking techniques, saturable absorbers such as in semiconductor saturable absorber mirrors (SESAM) or KLM are used in passive mode-locking techniques.

The first mode-locked Yb:YAG TD oscillator was demonstrated by Aus der Au et al. in 2000 [61] with the aid of a SESAM. The same group, as well as other groups, advanced this technology during the next decade and reached unprecedented results in terms of peak power, pulse energy and average power [15, 62]. An alternative implementation of a passive saturable absorber for mode-locking of an oscillator cavity is based on the

Kerr-effect. For intense laser beams, the refractive index of a material depends on the intensity of the incident electric field. For example, a Gaussian intensity distribution causes an increase of the refractive index in the central part of the beam relative to its outer regions therefore forming a nonlinear lens. The higher the light intensity, the stronger the action of such a lens becomes. For high-intensity pulsed laser beams, self focusing occurs following the intensity distribution of the spatial beam profile. In other words, the outer parts of the spatial beam profile experience less self-focusing in comparison to the inner part. A hard aperture can be implement to block the propagation of lower intensity parts of the beam, which experienced less self-focusing, see Fig. 2.3. In a resonator-cavity, this mechanism initiates mode-locking and acts as an artificial saturable absorber [8]. The discovery of the possibility to generate the shortest possible pulses from the compensation of nonlinearities and dispersion to form so-called soliton pulses, preceded the invention of KLM. For this reason a precise compensation of the induced Kerr-nonlinearity inside the cavity can be obtained with the aid of chirped-mirrors [63] (for more details about self-focusing see section 4.2.1).

For power scaling of soliton mode-locked oscillators both the nonlinear and the thermal instabilities are needed to be considered. A TD-shaped gain medium is, in both cases, an ideal solution as explained in section 2.1.2. Although the key ingredients were well known, the obvious merge of the solitonic KLM technique with the TD technology was demonstrated only many years later than SESAM, by Pronin et al. in 2012 [64]. In the years following its discovery, reproducing the advancement of SESAM-TD oscillators, the limits of this new technology were investigated and many records in terms of pulse duration, average power and energy were achieved also with KLM-TD oscillators [22, 54, 65]. A more detailed description about the evolution of both those technologies can be found in [8, 60].

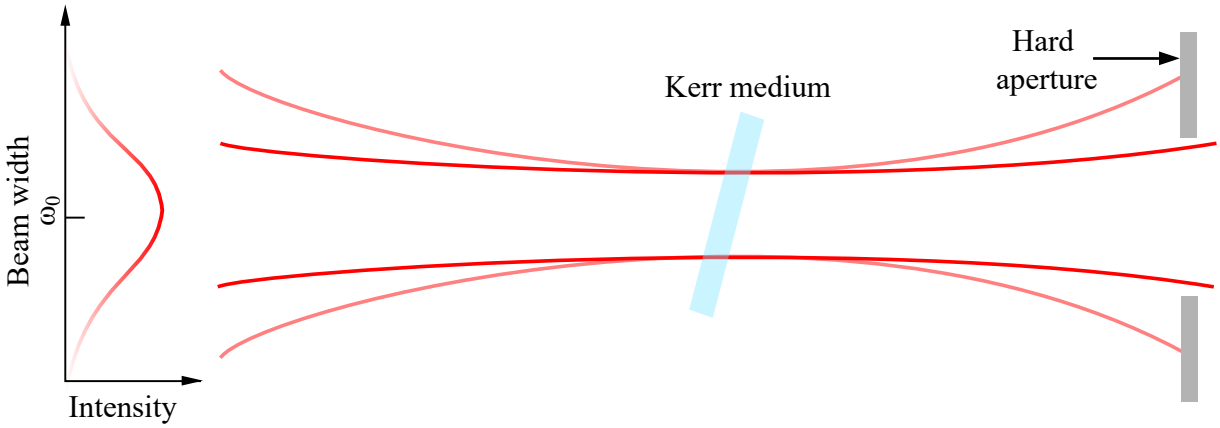

Figure 2.3 Basic principle of Kerr-lens mode-locking. The high intensity beam (dark red) experiences stronger self-focusing than the low intensity beam (bright red). A reduction of the cavity losses can be obtained via a hard aperture (represented in gray) blocking the low intensity beam. This mechanism initiates mode-locking and acts as an artificial saturable absorber.

2.2 Experimental setup

The following paragraphs describe the TD Yb:YAG KLM oscillator used as frontend for the experiments in the later chapters. The design of this oscillator cavity is based on [22, 33, 49]. Minor modifications are performed to better suite the different experimental setups for which this source is used as driving laser. These improvements include a water-cooled custom-design housing for increased thermal stability and a different Kerr-medium to allow, if required, carrier-envelope-phase-stabilization for future applications (for more details, see [33]).

2.2.1 Cavity design

The layout of the oscillator is depicted in Fig. 2.4. The standing waves are formed in a linear cavity, confined between a wedge-shaped output coupler (Layertec GmbH) with transmission of 19 % (OC), and a highly reflective flat end-mirror (EM). The amplifying medium is a nearly flat Yb:YAG thin-disk (TRUMPF Scientific Lasers GmbH) with a thickness of approximately 100 µm, which acts as an active mirror and is optically pumped by fiber-coupled diodes (Laserline GmbH, LDM3000-100), in the broad absorption band at 940 nm (as in Fig. 2.1b). Short pulses at a wavelength of 1030 nm are obtained by balancing the nonlinear effects and the dispersion in the resonator (i.e. soliton condition). Two 15 nm-bandwidth, high-dispersive (HD) mirrors with a total group delay dispersion (GDD) of $-6000\,\mathrm{fs}^2$ per round trip are implemented in the cavity for dispersion compensation [63].

The Kerr lensing occurs in two different plates of crystalline quartz in c-cut with a total thickness of 6 mm placed at Brewster's angle around the focus of a telescope consisting of two concave HR mirrors (F_1 and F_2) with radius of curvature (ROC) = -2000 mm. Spanning over 2 m from mirror F_1 to mirror F_2 this section of the cavity has to be folded twice with plane HR mirrors [13, 33]. In order to enable KLM operation, the cavity is adjusted to the edge of its stability zone [66]. For this purpose, a translation stage is placed at the folding mirrors of the focusing cavity. This provides tunability along the stability zone while keeping the optical axis aligned. For initiating the mode-locking, this translation stage is manually perturbed. An additional low noise, 100-mm travel-range translation stage allows to shift the Kerr medium along the optical axis. This is necessary to find the mode-locking threshold and to allow power optimization of the Kerr-medium position over the relatively long Rayleigh range of the focusing cavity [49].

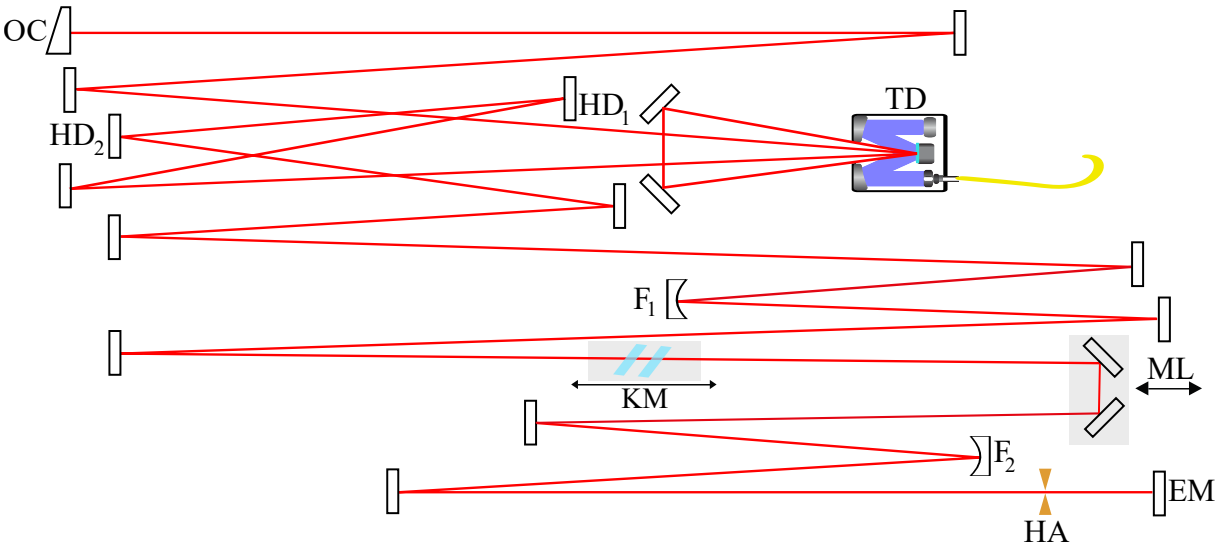

Figure 2.4 Schematic layout of the Kerr-lens mode-locked Yb:YAG thin-disk oscillator used as frontend for the experimental work. The linear cavity of the oscillator consists of a 19 % transmission output coupler, two high-dispersive mirrors with a group delay dispersion of $-3000\,\mathrm{fs}^2$ each, two 3 mm c-cut crystalline quartz Kerr media, and a copper hard aperture. Output coupler (OC), high-dispersive mirrors (HD_1, HD_2), Kerr medium (KM), hard aperture (HA), end mirror (EM), focusing mirrors (F_1, F_2), thin-disk (TD), mode-locking stage (ML).

Figure 2.5 shows the calculated mode radius along the oscillator cavity, which has a total length of approximately 10 m. The software *ReZonator2* [67] was used to simulate the mode radius along the cavity and the stability regions of the oscillator [66]. The separation distance between the cavity components and their curvature values are summarized in Table 2.1.

As evident from Fig. 2.5 and Tab. 2.1, the relatively large focal spot defined by the mirrors F_1 and F_2 is accomplished by a long Rayleigh range. This increases the interaction length of the focused oscillator mode with atmospheric air. As a result the contribution of air to the accumulated nonlinear phase shift in the oscillator becomes comparable to that of the Kerr medium. The evacuation of the oscillator housing to 160 mbar residual air pressure enables the control of all the effects connected to the interaction with atmospheric air. A detailed description of these effects and a discussion of their influence on the cavity design can be found in [49].

Component	**OC**	**TD_1**	**TD_2**	**F_1**	**KM**	**F_2**	**EM**
ROC (mm)	∞	-27000	-27000	-2000	∞	-2000	∞
Distance (mm)	0	1865	2755	6203	7280	8353	9370

Table 2.1 Oscillator cavity fundamental elements with radius of curvature (ROC) and distance from the first element (output coupler) in mm. Output coupler (OC), thin-disk first and second pass (TD_1 and TD_2), focusing mirrors (F_1 and F_2), Kerr medium (KM) and end mirror (EM).

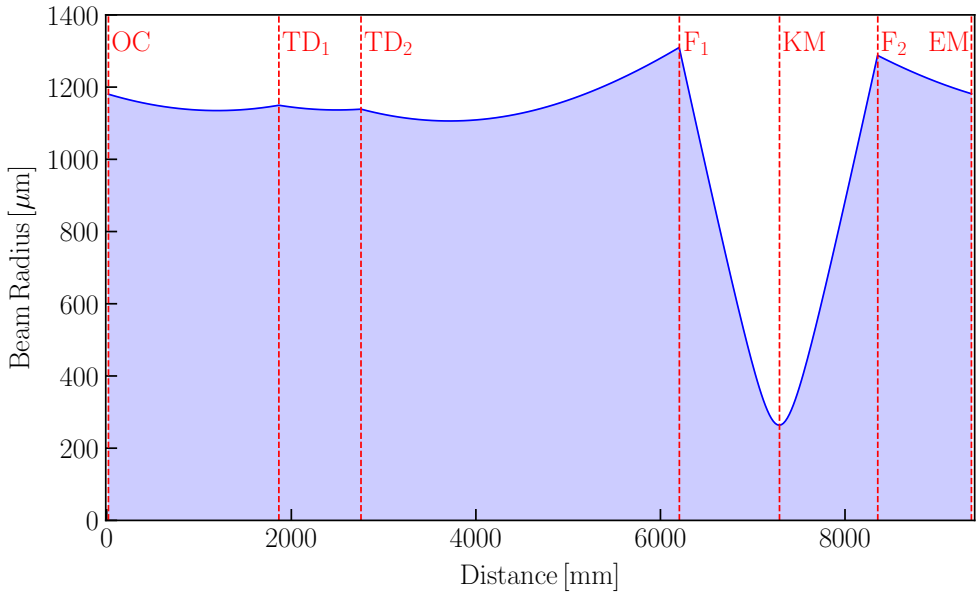

Figure 2.5 Mode radius along the oscillator cavity as function of the distance from the output couples (OC), simulated with *ReZonator2* software [67]. The dotted red vertical lines mark the position of the fundamental cavity components: output coupler (OC), thin-disk first and second pass (TD_1 and TD_2), focusing mirrors (F_1 and F_2), Kerr medium (KM) and end mirror (EM).

2.2.2 Characterization

The oscillator routinely delivers pulses with approximately 6.3 µJ energy, with an average power of 100 W, at 16 MHz repetition rate.

For the characterization of the oscillator pulses a second-harmonic frequency-resolved optical gating (SH-FROG) measurement is performed [68]. The measurement is carried out with a home-built setup employing a 10 µm-thick beta barium borate β-$Ba(BO_2)_2$ (BBO) crystal. The measured spectrogram as well as the retrieved spectrogram, spectrum and temporal profile can be seen in Fig. 2.6. The residual chirp, noticeable from the spectral phase in Fig. 2.2.2c, arises from material dispersion. After the oscillator chamber, several optical elements are used to optimally distribute the laser energy into different experiments and diagnostic setups: after the vacuum window closing the laser chamber a series of two attenuators, each formed by a half-wave plate and a thin-film polarizer (Layertec GmbH), are implemented. The retrieved pulse duration of the oscillator is 215 fs, with an FTL pulse duration of 192 fs as reported in the related figures.

The oscillator shows root mean square (RMS) average power fluctuations below 0.2 %, Fig. 2.7, and RMS beam-pointing deviations of approximately 2.3 µrad (without active beam stabilization), Fig. 2.8, over a period of 1 h. A drift of the beam can be seen from the tangential beam pointing measurement. This drift is related to warming up

of the optical components after the laser vacuum chamber. A beam stabilization system (MRC Systeme GmbH) has been installed to overcome this instability. In addition to these excellent stability performances, the spatial profile of the laser beam shows a remarkable M^2 value of 1.174 and 1.126, in x and y axis, respectively (ISO 11146 measured with M^2-200s, Ophir-Spiricon LLC). cf. Fig. 2.9.

The turn-key operation of the oscillator is obtained by the optimum heat management along all main components of the oscillator including the water-cooled laser housing, hard aperture and thin-disk heat-sink. The output parameters of the oscillator are reproducible on a daily basis, without the need of additional alignment or optimization.

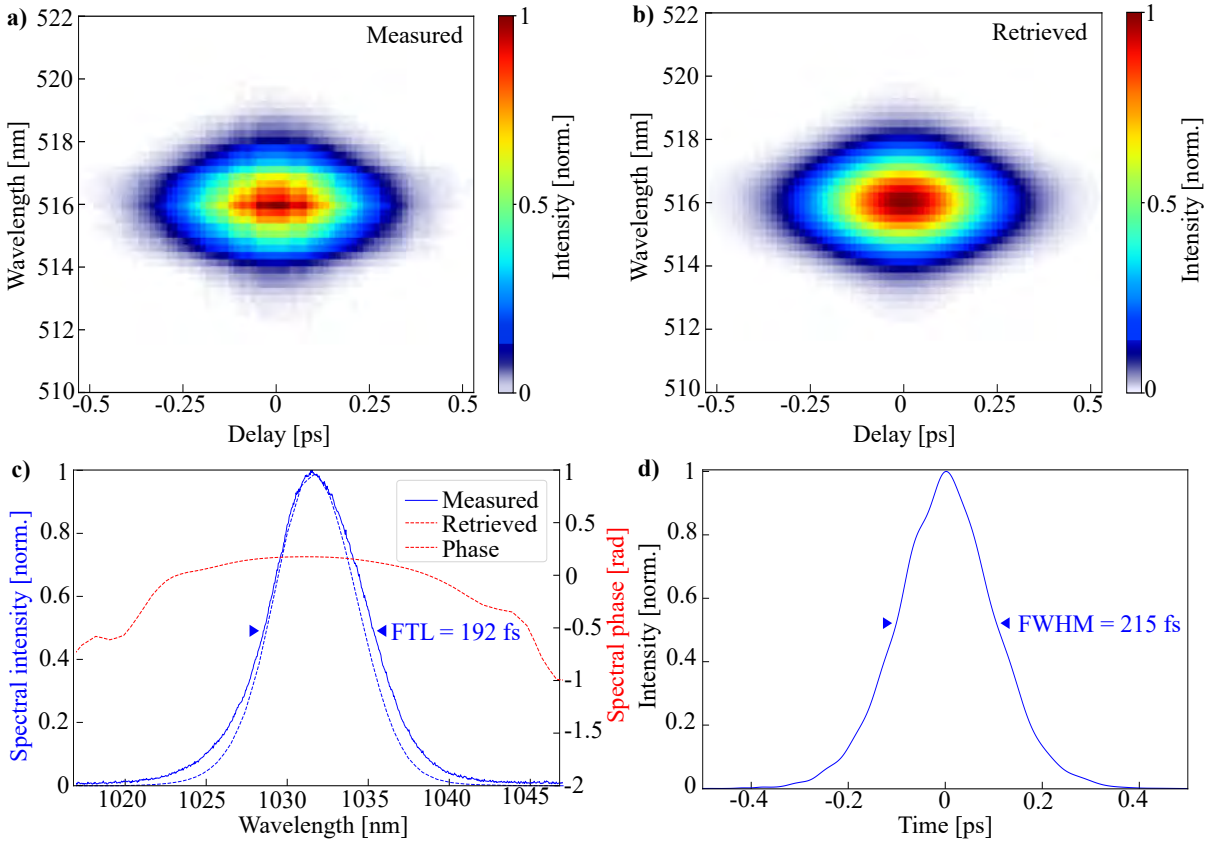

Figure 2.6 a) Measured and **b)** retrieved SH-FROG spectrograms of the oscillator output (G-error = 0.26 % [69]). **c)** Measured (solid blue line) and retrieved spectrum (dashed blue line). The FTL reported in the graph is calculated from the FWHM of this spectrum and reported in the graph. The red dashed line represents the spectral phase. **d)** Retrieved temporal profile. The FWHM of this curve, corresponding to the effective pulse duration, is reported in the graph.

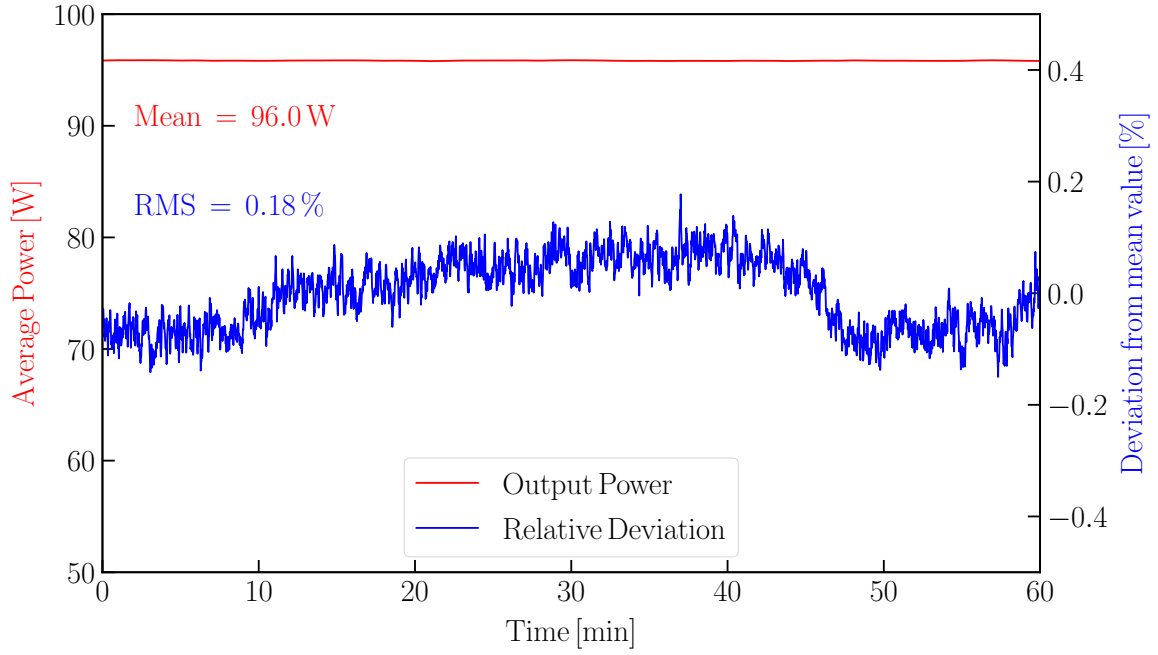

Figure 2.7 Average power fluctuations and relative deviation from mean value of the oscillator output over a time frame of 1 h.

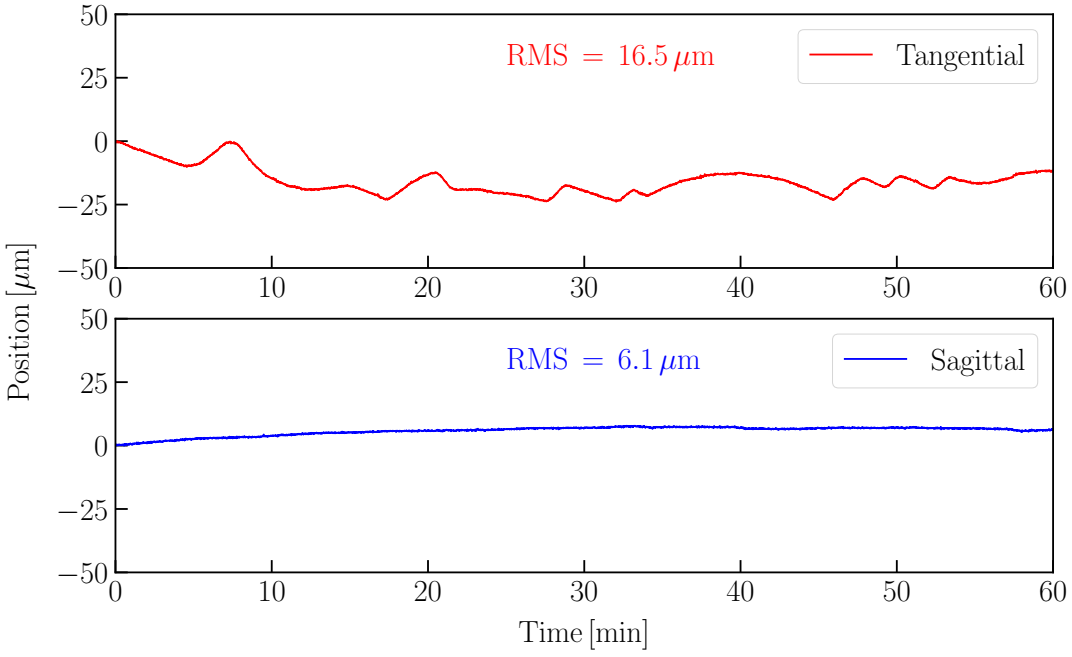

Figure 2.8 Sagittal and tangential positional beam pointing fluctuations for oscillator output measured over a time frame of 1 h.

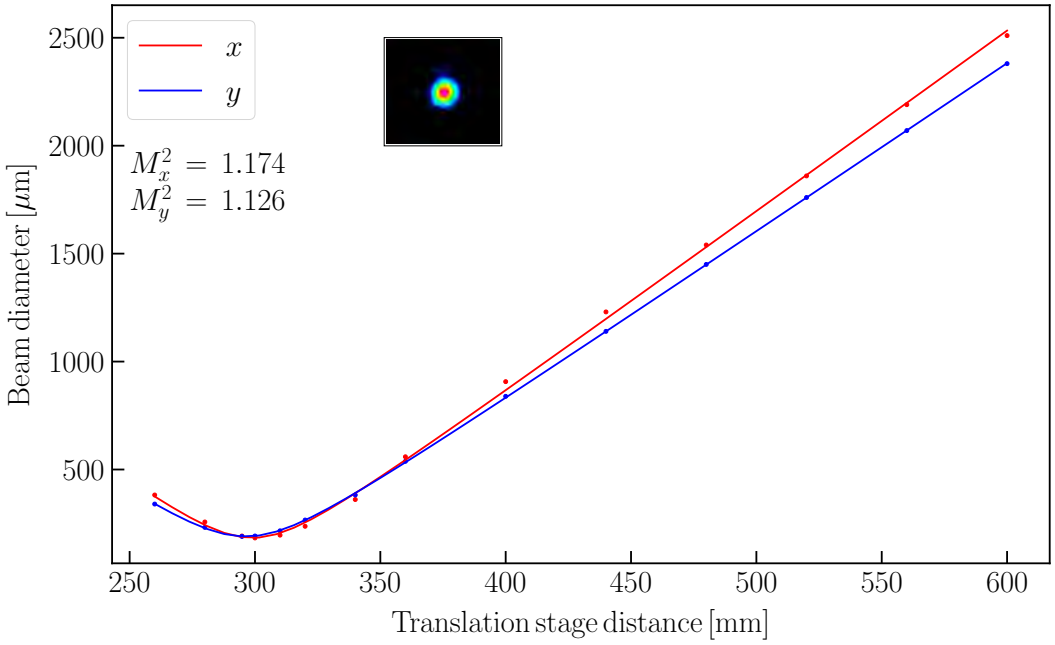

Figure 2.9 M^2 measurement for the oscillator setup. The measurement is carried out with ISO 11146 norm (M^2-200s, Ophir-Spiricon LLC). As reported in the graph, the values are 1.174 and 1.126, in x and y axis respectively.

2.3 Conclusion

To conclude, an Yb:YAG TD oscillator that served as frontend for the experiments and the applications outlined in the following chapters is presented. This system delivers pulses with 6.3 µJ energy, 100 W average power, at 16 MHz repetition rate. A pulse duration of 215 fs is achieved via KLM. In table 2.2 the relevant parameters for the characterization of the oscillator pulses and stability are summarized.

Average power	100 W
Average power fluctuations (RMS)	0.18 % (1 h)
Repetition rate	16 MHz
Pulse duration	215 fs (FTL ≈ 192 fs)
Energy	6.3 µJ
$\mathbf{M}^2_{x,y}$	1.174, 1.126
Beam-pointing deviations (RMS)	11 µm (1 h)

Table 2.2 Summary of the most relevant oscillator parameters.

The high extra-cavity peak power and the short pulses directly from the oscillator, achieved with the TD geometry in combination with Yb:YAG gain material and solitonic KLM, has proven to be an ideal starting point for efficient extra-cavity spectral broadening [70]. Moreover, the remarkable stability and the high repetition rate,

pose the basis for further spectroscopic applications [13], where reproducibility and high signal-to-noise ratio within a reasonable measurement time are crucial.

3 Compression to the sub-20 fs regime with multipass cells

As explained in the introductory chapter, in the last years bulk-based MPCs became a common extra-cavity pulse compression scheme to extend the bandwidth of Yb:YAG-based laser systems. These cells involve, generally, self-phase modulation (SPM)-based nonlinear broadening in combination with chirped mirrors (CM)-based linear temporal re-compression.

In this chapter, initially, the theory of light propagation in dielectric media is outlined followed by the description of the main nonlinear effects occurring in MPCs. The emphasis lies on SPM. Other third-order effects as self-steepening and Raman effects are also described. Afterwards, detailed illustration and characterization of the experiments are given. Here, two generations of setups, each based on two subsequent MPCs, are presented and compared. The first generation, proved the feasibility and the reliability of broadening technique for spectroscopic applications [13] and as fronted for subsequent compression stages [70]. The second generation, optically and opto-mechanically improved in comparison to the precedent, served as reliable frontend for a subsequent compression stage (section 4.2.2) used in the generation of ultra-broadband mid-infrared radiation (section 5.2.2).

For further reading, several excellent textbooks and review articles providing a thorough and insightful overview about nonlinear pulse propagation in dielectric media and nonlinear effects can be consulted, some examples are [71–73]. Other very insightful references about SPM-based broadening setups and MPCs are, for example, [24, 74].

3.1 Theoretical description

Light-matter interaction can be described with many different theoretical approaches. They range from a very simplified description, in which light is interpreted as rays obeying geometrical constraints, to a very detailed description, in which perturbation theory is used to account for quantum mechanical effects. For the experimental part of this work, a simplified approach is used. In the following description, light is treated as electromagnetic radiation and the interaction with a material is described as a function of the nonlinear polarization response.

The nonlinear polarization response of a material to an intense electromagnetic field can lead to the generation of polarization components at frequencies not present in the incident radiation field. Maxwell's equations describe the generation of these new components of the field [71]. In the following, a detailed description of light propagation in dielectric media and nonlinear effects relevant for the broadening schemes in the experimental setups is given.

3.1.1 Light propagation in dielectric media

Light can be described as an electromagnetic field using the electric field vector $\mathbf{E}$ and the magnetic field vector $\mathbf{B}$. The response of a dielectric medium to an applied light field can be described using the electric flux density $\mathbf{D}$ and magnetic flux density $\mathbf{H}$. The mentioned quantities depend on the space vector $\mathbf{r} = (x, y, z)$ and on the time scalar variable t. These dependencies are considered implicit and omitted in the following equation. The propagation of light in a dielectric medium can be described by Maxwell's equations

$$\nabla \cdot \mathbf{D} = \rho \tag{3.1a}$$

$$\nabla \cdot \mathbf{B} = 0 \tag{3.1b}$$

$$\nabla \times \mathbf{E} = -\frac{\partial \mathbf{B}}{\partial t} \tag{3.1c}$$

$$\nabla \times \mathbf{H} = \frac{\partial \mathbf{D}}{\partial t} + \mathbf{J} \tag{3.1d}$$

where ρ is the charge density and $\mathbf{J}$ is the current density vector. For a dielectric medium with no free charges and currents, as the crystals and the fibers which will be discussed in this and the next chapters, these two densities vanish. Thus, $\mathbf{J} = 0$ and $\rho = 0$. In addition, the medium is assumed to be non-magnetic. Therefore, the relations between

field vectors and flux density can be re-written as

$$\mathbf{B} = \mu_0 \mathbf{H}, \tag{3.2a}$$

$$\mathbf{D} = \epsilon_0 \mathbf{E} + \mathbf{P}\,, \tag{3.2b}$$

where ϵ_0 is the vacuum permittivity, μ_0 is the vacuum permeability and $\mathbf{P}$ is the electric polarization. Using equations 3.1 and 3.2, it is possible to derive the vector wave equation for an isotropic, nonmagnetic, and source-free medium

$$\nabla \times \nabla \times \mathbf{E} = -\frac{1}{c^2}\frac{\partial^2 \mathbf{E}}{\partial t^2} - \mu_0 \frac{\partial^2 \mathbf{P}}{\partial t^2} \tag{3.3}$$

where c is the speed of light in vacuum, given by $c = \sqrt{\frac{1}{\mu_0 \epsilon_0}}$.

The mathematical identity

$$\nabla \times \nabla \times \mathbf{E} = \nabla \cdot (\nabla \cdot \mathbf{E}) - \nabla^2 \mathbf{E} \tag{3.4}$$

can be used to rewrite Eq. 3.3. If only the linear response of an isotropic source-free medium is considered, the term $\nabla \cdot \mathbf{E}$ vanishes due to the Maxwell's equation 3.1a. For most cases we will consider in this paragraph, the nonlinear polarization is weak and the approximation $\nabla \cdot \mathbf{E} \approx 0$ is valid. For this reason, the vector wave equation can be written as the simplified wave equation

$$\nabla^2 \mathbf{E} = \frac{1}{c^2}\frac{\partial^2 \mathbf{E}}{\partial t^2} + \frac{1}{\epsilon_0 c^2}\frac{\partial^2 \mathbf{P}}{\partial t^2}\,. \tag{3.5}$$

The most common procedure for describing nonlinear optical phenomena is based on expressing the polarization in terms of the applied field strength. The reason why the polarization plays a key role in the description of nonlinear optical phenomena is that a time-varying polarization can act as a source of new components of the electromagnetic field. It is convenient, to begin with the generalization of Eq. 3.2b to include the different contributions to $\mathbf{P}$. The nonlinear response of a material system under an applied external electromagnetic field can be described by a series expansion of the polarization

$$\mathbf{P} = \mathbf{P}^{(1)} + \underbrace{\mathbf{P}^{(2)} + \mathbf{P}^{(3)} + \ldots}_{\mathbf{P}^{(\mathrm{NL})}} \tag{3.6a}$$

$$= \epsilon_0 \chi^{(1)} \mathbf{E} + \epsilon_0 \chi^{(2)} \mathbf{E}^2 + \epsilon_0 \chi^{(3)} \mathbf{E}^3 + \ldots \tag{3.6b}$$

where $\chi^{(1)}$ is the linear electric susceptibility, $\chi^{(2)}$ and $\chi^{(3)}$ are higher order susceptibilities and similarly $\mathbf{P}^{(2)}$ and $\mathbf{P}^{(3)}$ are higher order polarization responses. $\mathbf{P}^{(1)}$ linearly depends

on the electric field strength $\mathbf{E}$ and $\mathbf{P}^{(\mathrm{NL})}$ depends nonlinearly on the electric field strength $\mathbf{E}$. As the polarization order increases, the number of the frequency components involved in the nonlinear process increases. For example, in a second-order nonlinear process two frequency components interact to create a new frequency. Consequently, a process in which three frequency components interact to create a new frequency, is described by the third-order polarization. A more detailed explanation can be found in [71].

The nonlinear propagation in dielectric media can be described, in first approximation, considering only the linear polarization response $\mathbf{P} = \epsilon_0 \chi^{(1)} \mathbf{E}$. As explained previously, if only linear polarization is considered, the identity $\nabla \cdot \mathbf{E} = 0$ is valid [73]. Therefore, Eq. 3.5 can be further simplified to

$$\nabla^2 \mathbf{E} = \frac{\epsilon_r}{c^2} \frac{\partial^2 \mathbf{E}}{\partial t^2} \tag{3.7}$$

where $\epsilon_r(\omega) = 1 + \chi^{(1)}(\omega)$ is the frequency-dependant relative permittivity of the medium. For simplicity, it is useful to write this expression in the frequency domain

$$\nabla^2 \tilde{\mathbf{E}}(\mathbf{r}, \omega) = -\epsilon_r(\omega) \frac{\omega^2}{c^2} \tilde{\mathbf{E}}(\mathbf{r}, \omega) \tag{3.8}$$

where $\tilde{\mathbf{E}}(\mathbf{r}, \omega)$ is the Fourier transform of $\mathbf{E}(\mathbf{r}, t)$. When an intense laser pulse is used as light source, it is necessary to include the nonlinear effects in Eq. 3.8. Following the same procedure as before, the Fourier transform of Eq. 3.6 is applied. Thus, it is possible to write the wave equation for a nonlinear medium as

$$\nabla^2 \tilde{\mathbf{E}}(\mathbf{r}, \omega) + \epsilon_r(\omega) k^2 \tilde{\mathbf{E}}(\mathbf{r}, \omega) = -\mu_0 \omega^2 \tilde{\mathbf{P}}^{(\mathrm{NL})}(\mathbf{r}, \omega) \tag{3.9}$$

where $k = \omega / c$ is the wave number [72].

To solve the previous equation it is necessary to computationally model the fast oscillating electric field. However, this approach can be computationally very demanding as very high temporal resolution is needed to sample the rapidly oscillating carrier wave. Alternatively, it is possible to express the electric field as the product of the slowly oscillating envelope $\mathbf{A}$ and the fast-oscillating carrier field $e^{i\omega_0 t + \phi}$ as

$$\mathbf{E}(\mathbf{r}, t) = \mathbf{F}(x, y) \mathrm{A}(z, t) \, e^{i\omega_0 t + \phi} \tag{3.10}$$

here, $\mathbf{F}(x, y)$ is the transverse field profile and ϕ is the time-dependent phase. If the peak of the pulse envelope is at $t = 0$, as the gray curve in Fig. 3.1a, φ corresponds to the phase of the carrier field with respect to the envelope peak, also called carrier-envelope phase (CEP) or absolute phase. If $\varphi = 0$, a maximum of the carrier field corresponds to

the peak of the envelope, red curve in Fig. 3.1a. If $\varphi = \pi/2$, the carrier field at the peak of envelope is zero, blue curve in Fig. 3.1a. Femtosecond laser sources typically generate pulse trains in which the CEP varies from pulse to pulse. Therefore, the generation of light pulse with pre-determined and reproducible electric field profile, otherwise named CEP-stable pulses, is of great interest nowadays. This capability, has paved the way to the synthesis of optical waveforms for strong-field physics applications as high harmonic generation [75].

For the scope of this chapter, it is sufficient to employ an envelope model, in which the slowly oscillating envelope is decoupled from the fast-oscillating carrier field. Thus, only the envelope needs to be sampled and the computational costs are greatly reduced. This approximation is called slowly varying envelope approximation (SVEA). This approximation is valid when the duration of the envelope functions in time should be significantly greater than the optical period

$$\left|\frac{\partial^2 A}{\partial z^2}\right| \ll 2k \left|\frac{\partial A}{\partial z}\right| \ll k^2 |A|. \tag{3.11}$$

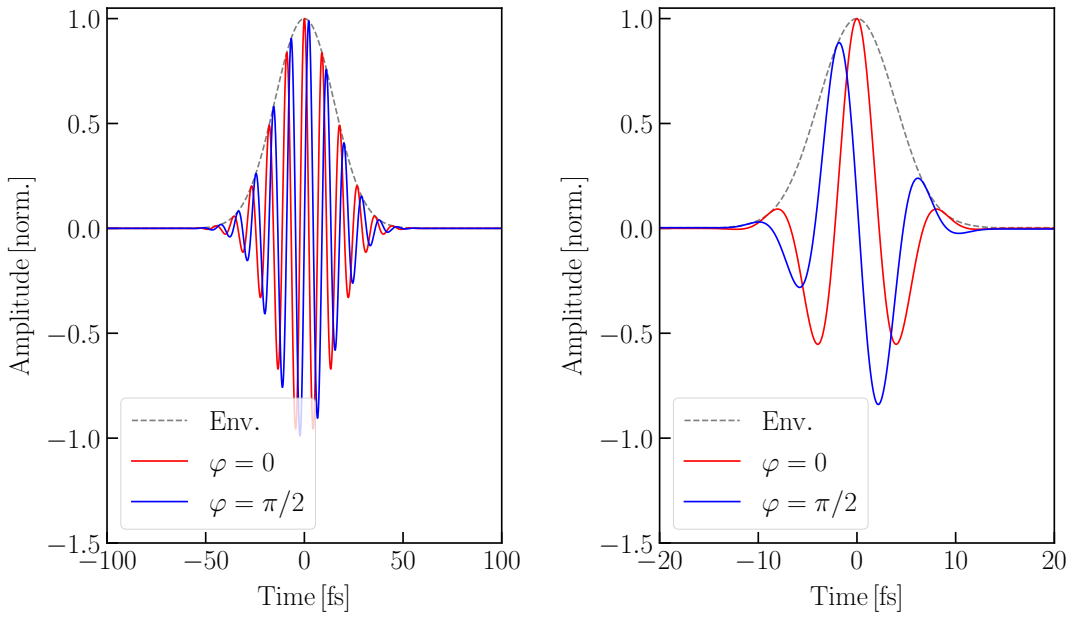

Figure 3.1 Depiction of the slowly-varying envelope (grey) and of the fast-oscillating carrier fields with different absolute phases (red and blue) for **a)** multi-cycle pulses and for **b)** few-cycle pulses.

This approximation has proven to be valid over a remarkably broad range of conditions in ultrafast nonlinear optics. Especially when the nonlinearities remain within the limits of a perturbative treatment and the width of the incident and generated pulses exceed several optical periods [72]. Fig. 3.1 shows the carrier field (red and blue) and the envelope (dashed gray) of multi-cycle pulses on the left and of few-cycle pulses on the

right. The SVEA approximation lacks of accuracy once the few-cycle regime is reached. For the multi-cycle pulse the envelope gives a sufficient approximation of the pulse, while for the few-cycle pulse this description is not sufficient anymore and the CEP should take into account. A small variation in the CEP phase of a few-cycle pulse can drastically change the solution of the wave equation for nonlinear phenomena, while this effect is mitigate for multi-cycle pulses.

Eq.3.10 can be further simplified by applying the following assumptions. Firstly, as mentioned above, in this thesis all the broadening media are crystals or single mode fibers supporting only the fundamental mode. For this reason $F(x, y)$ can be approximated by a Gaussian distribution

$$\mathrm{F}(x, y) \approx e^{\frac{-\left(x^2+y^2\right)}{w^2}} \tag{3.12}$$

with the width parameter w depending on the guiding structure. Secondly, in most cases an exact functional form of the wave number k is not known and the Taylor series expansion is used

$$k(\omega) = k_0 + k_1(\omega - \omega_0) + \frac{1}{2}k_2(\omega - \omega_0)^2 + \frac{1}{6}k_3(\omega - \omega_0)^3 + \cdots \tag{3.13}$$

where different orders of k are related to different physical phenomena. For example, k_0 describes the phase shift between the envelope of the pulse and the rapidly oscillating electric field. In other words, it is connected to CEP, Fig. 3.1. k_1 describes the group velocity $v_g = \frac{1}{k_1}$. k_2 describes the GDD, $k_2 = \frac{d}{d\omega}\frac{1}{v_g}$. If $k_2 > 0$, lower frequencies travel faster than higher frequencies and accumulate at the leading edge of the pulse. This is known as normal GDD regime and the resulting pulse is called positively chirped. The opposite case, where $k_2 < 0$, is referred to as anomalous GDD regime and the pulses as negatively chirped pulses. k_3 is relevant for third order phenomena, which causes satellite pulses in the temporal domain. For most experiments, it is favorable to concentrate all the energy in a single peak and avoid side features.[72]. For this reason, high order dispersion effects should be avoided. A practical example can be found in paragraph 3.2.1.

At this point, it is possible to write the propagation equation for the pulse envelope $A(z, t)$. Higher order terms such as $\partial^2 A/\partial z^2$ can be neglected by applying the SVEA. Assuming no Kerr-nonlinearities (see Section 3.1.2) k is only expanded till the second order. The resulting equation is the nonlinear Schrödinger equation (NLSE)

$$\frac{\partial \mathrm{A}}{\partial z} + k_1\frac{\partial \mathrm{A}}{\partial t} + i\frac{k_2}{2}\frac{\partial^2\ \mathrm{A}}{\partial t^2} + \frac{\alpha}{2}\ \mathrm{A} = i\gamma|\mathrm{A}|^2\ \mathrm{A} \tag{3.14}$$

where α is the loss parameter and γ is the nonlinear parameter, defined as

$$\gamma = \frac{n_2 \omega_0}{c A_{\text{eff}}} \tag{3.15}$$

where n_2 is the nonlinear refractive index. A_{eff} is the local effective area, which is defined as $A_{\text{eff}} = \pi\omega^2(z)$ for a Gaussian beam [74]. It is worth mentioning here, that in practice it is difficult to strictly satisfy the plane-wave approximation, which allowed us to eliminate any transverse spatial derivatives in the wave equation. For example, the usual Gaussian spatial profile of a propagating beam leads to a Gaussian nonlinear refractive index profile, which acts as a nonlinear lens. This leads to self focusing (SF). For ultrashort pulses, the time dependence of this nonlinear lens couples the temporal and spatial coordinates. Further details about SF can be found in Chapter 4.

Using Eq. 3.14 it is possible to describe the light propagation in a single-mode fiber or in a crystal by studying the compensation effects between linear dispersion described by k and nonlinear effects described by γ.

3.1.1.1 Computational approach

Although in some cases an exact solution of the NLSE is possible, in most cases a numerical analysis of the nonlinear propagation is required. One of the most popular computational approaches is the *split-step Fourier method* [72]. In this method linear and nonlinear contributions to the propagation equation are handled separately, with nonlinear terms computed in the time domain and linear terms in the frequency domain. Because the fast Fourier transform algorithm is used to convert between time and frequency domain, this method is computationally efficient.

A basic description of the split-step Fourier method is given in the following. The propagation equation, Eq. 3.14, is evaluated along a step of size Δz. These steps are the discrete lengths in which the nonlinear medium is divided for calculation. Firstly, the electric field amplitude is Fourier-transformed to the frequency domain and the dispersion effects along Δz are calculated. Secondly, the resulting amplitude is Fourier-transformed back into the time domain and the nonlinearity is taken into account for the same distance Δz. For the subsequent interval Δz, the initial amplitude is replaced by the result of the first iteration. Thus, the output amplitude after $n\Delta z$ can be calculated by repeating this procedure.

Some errors can occur due to the simplification introduced by this computational method. To reduce these errors to an acceptable amount, a sufficiently small step size Δz

must be selected. As a rough guide, it should be small compared to both L_D and L_{NL}. L_D is the characteristic dispersion length scale describing the distance at which dispersion will significantly broaden a bandwidth-limited input pulse in the absence of nonlinearity. L_{NL} gives the distance at which the nonlinearity will significantly broaden the spectrum of a bandwidth-limited input pulse in the absence of dispersion. Another problem can arise when time and frequency vectors are not sampled adequately. To avoid inadequate sampling, the pulse and its spectrum must be completely represented within the time and frequency vectors used for the computation otherwise numerical instabilities can occur. Such instabilities are linked to the periodicity introduced by the discrete Fourier transform modellization of a pulse. For example, a portion of a pulse extending further than the latest time extreme reappears at the earliest times [72, 73].

For this thesis, the *Python* [76] distribution and in particular the package *pyNLO* is used for simulations. This open-source package employs the split-step Fourier method to simulate nonlinear pulse propagation in different materials with focus on single-mode fibers and, in general, in wave-guiding structures. With a few changes, this package can be easily extended to the bulk-based qausi-waveguides described in the experimental part of this thesis [77]. Possible errors arising from the simplifications explained above are avoided by accurately choosing the step-size and the time-window for the computation. Due to the high efficiency of the fast Fourier transform algorithm, the interaction of 250 fs-long pulses with 6.35 mm of material could be simulated in less than 4 seconds, using a windows of up to 8 ps and a step size smaller than 10 µm.

3.1.2 Relevant nonlinear effects

In the previous paragraphs, a general approach to describe propagation of a light pulse in a dielectric material was introduced. For high electric field strengths the polarization response is nonlinear and can be described by Eq. 3.6. For a material with spatial inversion symmetry, such as liquids, gases and amorphous solids, the second order nonlinear susceptibility $\chi^{(2)}$, as all even order susceptibilities, vanishes [71]. Thus, second order effects can not occur in such materials. All of the noble gases and crystals, in the work presented in this chapter and in the following, exhibit inversion symmetry. Therefore, the most important nonlinear effects result from third order polarization response.

The contribution of third-order effects to the nonlinear polarization response in an isotropic medium is given by

$$\mathbf{P}^{(3)} = 3\epsilon_0 \chi^{(3)} |\mathbf{E}|^2 \mathbf{E}\,. \tag{3.16}$$

In the spectral region in which the majority of optical materials are transparent, $\chi^{(3)}$ can be approximated by its real part. Therefore, the nonlinear polarization results in an index of refraction which depends nonlinearly on the electric field

$$n = n_0 + 2\overline{n}_2 \langle \mathbf{E}^2 \rangle \tag{3.17a}$$

$$= n_0 + n_2 I(t) \tag{3.17b}$$

where n_0 is the weak-field refractive index or simply linear refractive index, $\langle \mathbf{E}^2 \rangle$ is the time averaged electric field and $\overline{n}_2 = n_2 n_0 \epsilon_0 c$ is the second order index of refraction. The quantity $\overline{n}_2$ describes the strength of the relation between the electric field and the refractive index or, in other words, gives the rate at which the refractive index increases with increasing the optical intensity. The change in refractive index is called *optical Kerr effect*. The optical Kerr effect occurs in gases, liquids, and solids regardless of their symmetry. The magnitude of the nonlinear refractive index depends on the material, e.g. fused silica exhibits $n_2 = 3 \times 10^{-16}\,\mathrm{cm^2\,W^{-1}}$.

The total polarization for linear and third order interactions, as for the experiments described later in this chapter, can be written as

$$\mathbf{P} = \epsilon_0 \chi^{(1)} \mathbf{E} + 3\epsilon_0 \chi^{(3)} |\mathbf{E}|^2 \mathbf{E}\,. \tag{3.18}$$

Introducing the effective susceptibility

$$\chi_{\mathrm{eff}} = \chi^{(1)} + 3\epsilon_0 \chi^{(3)} |\mathbf{E}|^2. \tag{3.19}$$

it is possible to relate the third-order nonlinear susceptibility $\chi^{(3)}$ to the nonlinear refractive index by

$$n_0^2 = 1 + \chi_{\mathrm{eff}}\,. \tag{3.20}$$

inserting Eq. 3.17a on the left side, Eq. 3.19 on the right side and using the relation between n_2 and $\overline{n}_2$, the following equivalences are found

$$n_0 = \sqrt{1 + \chi^{(1)}} \tag{3.21a}$$

$$\overline{n}_2 = \frac{3\chi^{(3)}}{4n_0} \tag{3.21b}$$

$$n_2 = \frac{3}{4n_0^2 \epsilon_0 c} \chi^{(3)}\,. \tag{3.21c}$$

In general the intensity dependence of the refractive index implies its variation in time and space. The temporal variation leads to pulse chirp and the (transverse) spatial variation leads to lensing effects. These processes are called SPM and SF, respectively.

3.1.2.1 Self-phase modulation

SPM is the phenomenon in which an intense pulse transiently modifies the refractive index through the optical Kerr effect. This modification in turn affects the temporal phase of the pulse and is the origin of spectral broadening.

It is possible to begin the description of SPM considering the propagation of an optical pulse

$$E(z,t) = A(z,t)e^{i(k_o z - \omega_0 t)} + \text{c.c.} \tag{3.22}$$

through a medium characterized by a nonlinear refractive index $n(t) = n_0 + n_2 I(t)$ where $I(t) = 2n_0\epsilon_0 c|A(z,t)|^2$. The assumptions made for the description of this phenomenon are: (i) the SVEA is valid; (ii) the medium responds instantaneously to the pulse intensity; (iii) the length of the medium is sufficiently small so that no reshaping of the optical pulse can occur within the medium. Propagation of the pulse inside the medium results in a phase change equal to

$$\Phi_{NL}(t) = -\frac{\omega_0 L n_2}{c} I(t). \tag{3.23}$$

Thus, the spectrum of the transmitted pulse is broader than the incident pulse spectrum. To describe the effect on the spectral content, it is useful to introduce the instantaneous frequency

$$\omega(t) = \omega_0 + \delta\omega(t) \tag{3.24}$$

where $\delta\omega(t) = \frac{d}{dt}\Phi_{NL}(t)$ denotes the temporal variation of the instantaneous phase. The instantaneous frequency is modulated according to the time derivative of the intensity. Thus, the magnitude of the frequency modulation scales with the magnitude of the peak nonlinear phase shift. For a Kerr-medium with $n_2 > 0$, at the leading edge of the pulse the change in phase is negative ($dI/dt > 0$) and the spectrum is red shifted. At the trailing edge the change in phase is positive ($dI/dt < 0$) and the spectrum is blue shifted [72]. This is illustrated in Fig. 3.2, which depicts a Gaussian input pulse on the left and the corresponding phase shift on the right.

Either SPM or normal dispersion acting on a pulse lead to a frequency chirp. For sufficiently intense input pulses, SPM lead to spectral broadening in the form of a positive chirp. If the material dispersion in the medium is significant, besides the pulse spectrum also the temporal profile is modified. A dispersive delay line can be used to compress the pulse and synchronize its frequency components, as explained in Fig. 3.3. Normally, a waveguide geometry is used to obtain the SPM necessary for pulse broadening. Waveguiding prevents self-focusing and ensures that the nonlinear phase shift and the spectral broadening are uniform across the transverse spatial beam profile.

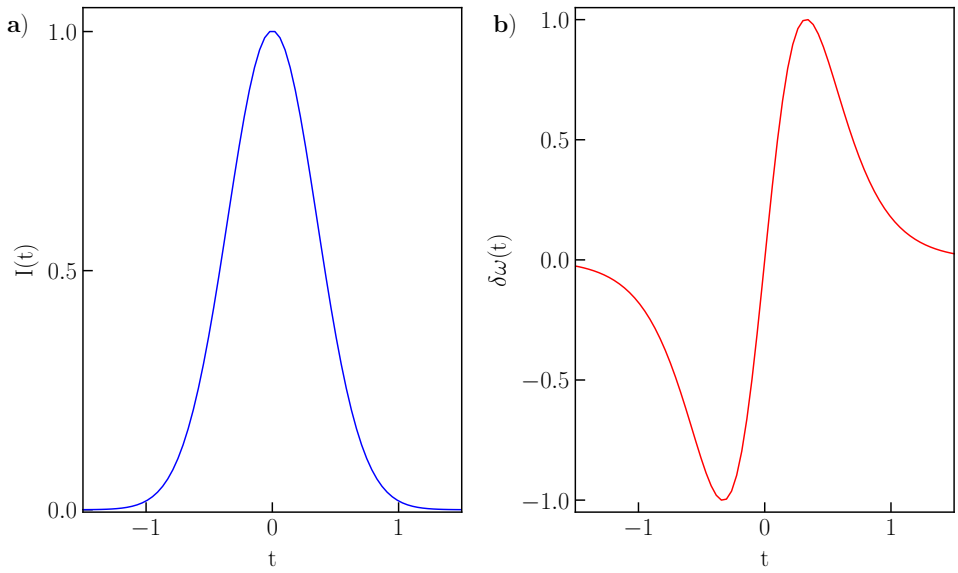

Figure 3.2 Self-phase modulation of a pulse with Gaussian intensity profile. **a)** Time dependant intensity of a Gaussian pulse and **b)** corresponding change in instantaneous frequency. The leading edge is shifted to lower frequencies while the trailing edge is shifted to higher frequencies.

Similarly to fiber waveguides, bulk-based quasi-waveguides can be used. Similar to laser cavities and regenerative amplifiers, the nonlinearity in bulk-based quasi-waveguides is distributed over a large number of passes. Each pass in the MPC arrangement comprises transmission through a bulk-medium for SPM followed by a reflection off a curved dispersive mirror. The nonlinear phase shift accumulated by SPM in the medium is compensated by the negative GDD of the dispersive mirror after each pass [72]. The curvature of the dispersive mirror leads to periodic refocusing such that the confocal parameter remains unchanged. The propagation in the MPC cavity plays the same spatial homogenizing role, as a series of successive lenses or as a waveguide. A high number of passes is accomplished by mode matching the input beam and injecting it along a specific off-axis path of the cell. This scheme was first described for stable symmetric resonator configurations by Herriott et al. 1964 [78]. Through careful a priori calculations and optical alignment, a circular pattern of equally spaced spots on each mirror is assured. The Herriott geometry also requires that the beam pattern close on itself after an even number of passes, which guarantees optimum utilization of the MPC volume [79]. Figs. 3.7 and 3.11 show four examples of MPC in Herriott geometry. This concept, and in general a MPC, offers additional robustness compared to hollow waveguides: it is less sensitive to beam pointing instabilities; it offers additional control on the nonlinear pulse propagation through the medium; its only limitations are related to the optical damage threshold of the mirrors, bulk media and coatings, which can be engineered by cavity design [74].

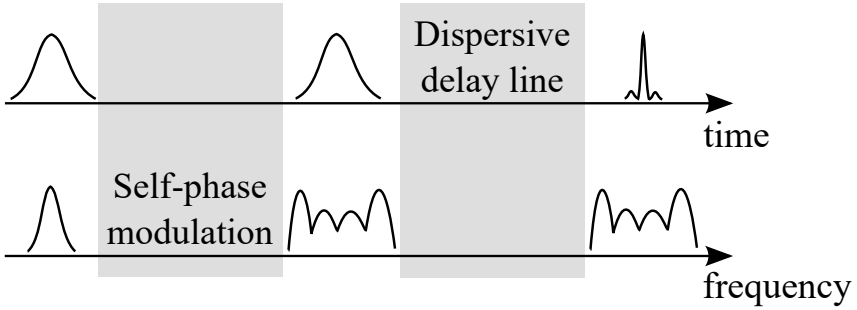

Figure 3.3 Graphical depiction of a pulse compression scheme. For intense input pulses, self-phase modulation in a bulk material leads to a spectral broadening in the frequency domain. If the material dispersion is significant, the pulse is typically positively chirped in the time domain. A dispersive delay line can be used to achieve pulse compression and synchronize different optical frequency components.

As explained above, dispersive mirrors can be used in pulse compression schemes. Chirped mirrors are a dielectric multi-layer system consisting of a sequence of films characterized by a certain refractive index n_i and thickness d_i. A defined sequence of (n_i, d_i) combinations representing individual films can closely reproduce a predefined reflection and phase behavior in a certain spectral range. This idea was first pursued by Szipöcs et al. in 1994 [80]. As the amplitude and phase responses become more and more complicated, this technology gained importance. In many cases, a constant reflectivity and certain dispersive behavior in a defined spectral region is desired for chirped mirrors, i.e. a constant amount of GDD within a predefined spectral range or to compensate a certain amount of material dispersion [81]. In this thesis chirped mirror compressor were extensively used, not only for the case of MPCs, where they play a major role, but also for compression to sub-10 fs regime (chapter 4) and as already mentioned in the previous chapter for solitonic Kerr-lens mode locking [63, 82], (see Section 2.1.3).

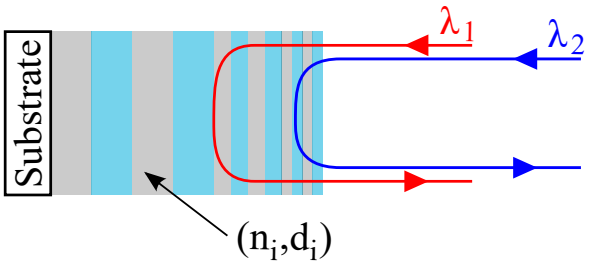

Figure 3.4 Graphical depiction of a chirped mirror. A dielectric multi-layer system is deposited on a substrate. The multi-layer consist of a sequence of films, each of them characterized by a certain refractive index n_i and thickness d_i. Each layer reflects different wavelengths of the incident beam, such that each wavelength, as λ_1 and λ_2, experiences different optical path lengths. A defined sequence of (n_i, d_i) combinations representing individual films can closely reproduce a predefined reflection and phase behavior in a certain spectral range.

3.1.2.2 Self-steepening

From the time derivative term in the NLSE, Eq. 3.14, an effect distorting the pulse amplitude during propagation can be calculated. This effect is termed self-steepening. In the following, only a qualitative description will be outlined. For further reading a detailed mathematical derivation can be found in most classical nonlinear optics textbooks and references, as [71–73, 83].

Physically, the distortion arises from an intensity-dependent group velocity

$$\frac{1}{v_g(t)} = \frac{\partial k}{\partial \omega} = \frac{2\pi}{\lambda_0}\frac{\partial n(I(t))}{\partial \omega} \,. \tag{3.25}$$

$v_g(t)$ creates an asymmetry in the temporal pulse shape with a steepening of the trailing edge, cf. Fig. 3.5a. This asymmetry, in combination with self-phase modulation, causes the generation of an asymmetric spectrum. This can be clarified considering the generated frequencies $\omega(t)$ of an asymmetric temporal pulse shape, cf. Fig. 3.5b. Correspondingly in the frequency domain, the broadened spectrum exhibits a stronger peak shifted towards longer wavelengths and a weaker blue shifted pedestal.

In the extreme case, self steepening results in the formation of an optical shock wave, the effects of which are similar to an acoustic shock wave. At the shock point, the intensity-dependent slope of the trailing edge approaches infinity and the intensity changes instantaneously [83].

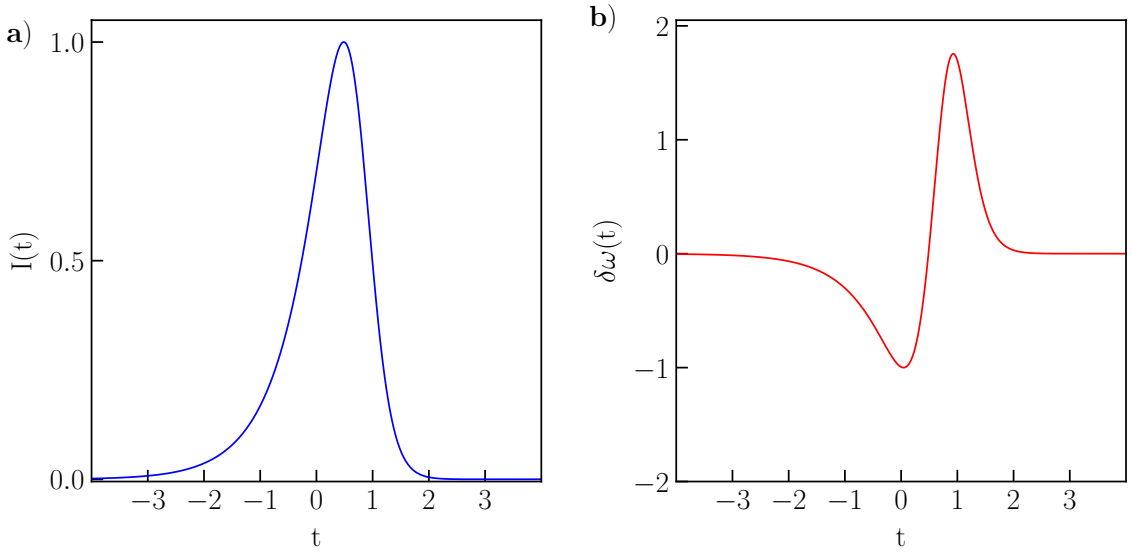

Figure 3.5 Graphical depiction of self-steepening for a Gaussian pulse. **a)** For positive values of the nonlinear refractive index, the peak of the intensity profile of a Gaussian pulse is progressively delayed during propagation. **b)** The corresponding change in instantaneous frequency lead to a spectrum that exhibits a stronger peak shifted towards to longer wavelengths.

It is important to mention that as long as the pulse duration is much greater than an optical cycle (SVEA is valid), the self-steepening is weak compared to self-phase modulation. In the experiments, direct observation of self-steepening is difficult since its effect is usually strongly intermixed with group velocity dispersion. However, it was shown numerically and experimentally that the self-steepening process has an important influence on experiments in nonlinear fiber optics, white light continuum generation in bulk transparent media and especially on soliton formation and propagation [71].

3.1.2.3 Raman effect

Raman scattering results from the interaction of light with the vibrational modes of the molecules constituting the medium. The energy diagram for a generic Raman transition is shown in Fig. 3.6. An incident photon at frequency ω_p, named pump photon, is absorbed by the molecules in the medium to transition into a virtual state. If the molecule does not transition back to its ground state, but to a vibrational state, a photon with lower frequency ω_s, named Stokes photon, is emitted. Similar to laser emission, the transition to a vibrational state can be amplified by the presence of an optical field with frequency ω_s. This effect is called stimulated Raman scattering [71].

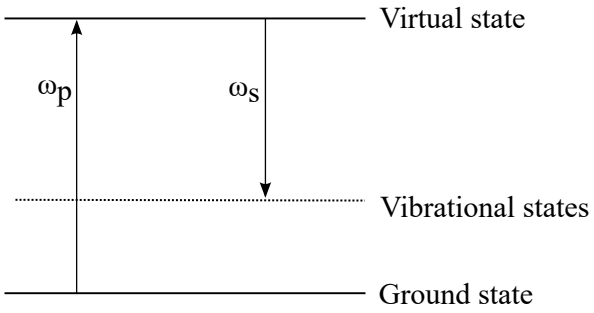

Figure 3.6 Energy diagram for Raman scattering. An incident photon at frequency ω_p, named pump photon, is absorbed by the molecules in the medium to transition into a virtual state. If the molecules does not transition back to its ground state, but to a vibrational state, a photon with lower frequency ω_s, named Stokes photon, is emitted.

For sufficiently-intense and broadband beams, intra-pulse stimulated Raman scattering results in a self-frequency shift. The high frequency components of the pulse act as pump to amplify lower frequencies, leading to a red shift in the spectrum. For the bulk-based broadening described in this thesis, the propagation length is too short for the Raman effect to have a significant influence on the pulse. Additionally, the noble gases used for the fiber-based compression are monoatomic, they do not exhibit vibrational states. Therefore, the Raman effect can be neglected for the presented simulations and experiments but can be mentioned as effect relevant for SPM-based broadening schemes [84]. Detailed descriptions of the Raman scattering can be found in [71, 85, 86].

3.2 Experimental setups

The home-built Yb:YAG TD KLM oscillator described in Chapter 2, is used as direct source for the first stage in the nonlinear pulse compression scheme. To achieve sub-20 fs pulses with high optical efficiency, two external nonlinear compression stages based on MPCs, in Herriott geometry, are used. Two generations of setups are presented and compared. The first generation, allowed important initial investigations about THz generation [13] and about subsequent compression stages [70]. The second generation is optically and opto-mechanically improved in comparison to the precedent. This upgraded setup is employed as reliable frontend for a subsequent compression stage (section 4.2.2) used for the generation of ultra-broadband mid-infrared radiation (section 5.2.2).

3.2.1 First generation

For the first generation of nonlinear compression scheme for the generation of sub-20 fs pulse durations, two consecutive MPCs are used. Each of them is followed by a chirp-mirrors compressor to compensate the accumulated phase. The schematic of the setup is shown in Fig. 3.7.

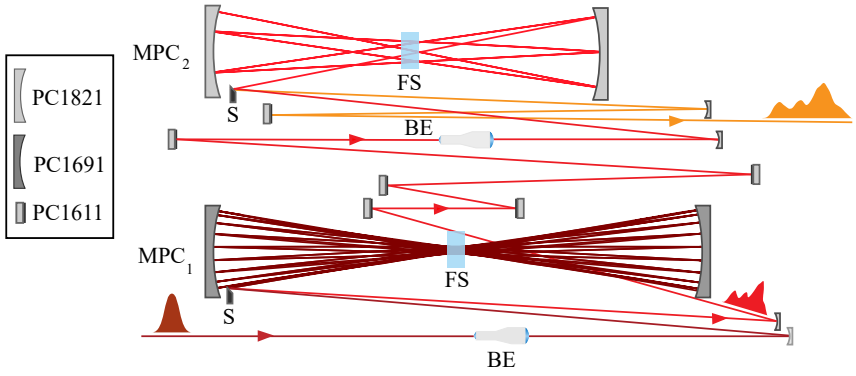

Figure 3.7 Schematic layout of the first generation of compression scheme based on multipass cells in Herriott type geometry. The output of the oscillator is coupled into a first MPCs containing 6.35 mm fused silica (FS) as nonlinear medium and two curved dispersive mirrors (PC1691). The mode matching is achieved via a beam expander (BE), a focusing mirror and a scraper (S). After 38 passes through the medium the beam is coupled out and re-collimated. The broadened output is temporally re-compressed by a chirped mirror compressor containing 7 mirrors (PC1611). After the first cell, the beam is mode-matched into a second MPCs also containing 6.35 mm fused silica as nonlinear medium (FS) and two curved dispersive mirrors (PC1821). The beam is coupled out after 6 passed through the medium and re-collimated. The broadened output is temporally re-compressed by a chirped mirror compressor containing 3 mirrors (PC1611).

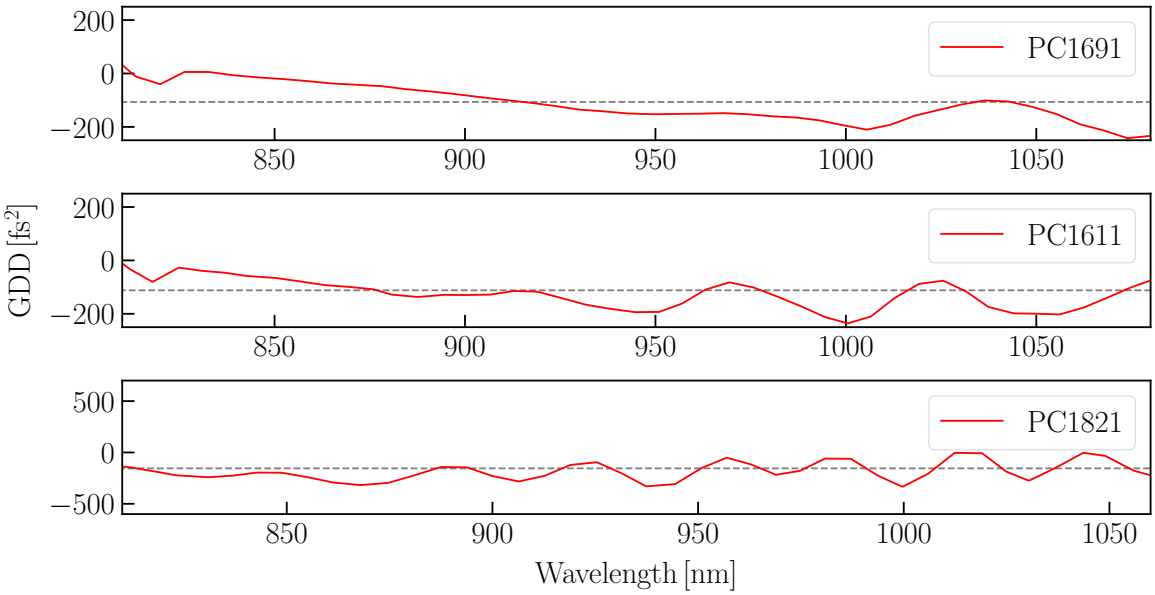

Figure 3.8 Group delay dispersion curves (red) and relative average (gray) for the different dispersive mirrors used in the first generation of MPCs-based compression: the coating named PC1691 is used in the first cell, the coating PC1611 is used for the compressor after the first and the second cell, the coating PC1821 is used in the second cell. The dispersive coating PC1821 is a complementary-pair type of chirped mirrors, the oscillations of the dispersion curve of one mirror have opposite phase in comparison to the complementary mirror. Therefore, the average dispersion curve can better approximate the design. In the figure only the average dispersion is reported for clarity.

In the first stage, the 6.3 µJ pulses from the oscillator are first sent to a mode-matching setup. The mode-matching setup includes a zoom beam expander (165-1181, EKSMA Optics UAB) and a focusing HR concave mirror with ROC = 1500 mm. With the aid of a scraper mirror, the beam is couple into and focused in the middle of a MPC containing two curved dispersive mirrors with ROC = 300 mm and average GDD = $-100\,\mathrm{fs}^2$ for 350 nm spectral bandwidth centered at 1030 nm. The dispersion curve of these mirrors, named PC1691, is reported in Fig. 3.8. A 6.35 mm-thick, anti-reflection coated fused-silica plate is used as the nonlinear medium. An additional curved dispersive mirror is used to re-collimate the beam reflected back to the scraper after 38 passes through the medium. The output spectrum after this initial stage is shown in Fig. 3.9c. The optical efficiency in this stage is 82 %. Increasing the number of passes does not lead to a higher factor of spectral broadening, due to the accumulated uncompensated linear and nonlinear phase at each round trip. The output pulses of the first stage are coupled out and compressed to 46 fs by using 7 additional dispersive mirrors, PC1611 in Fig. 3.8, compensating the total residual dispersion of approximately $840\,\mathrm{fs}^2$ around 1030 nm. A home-built, SH-FROG employing a 10 µm BBO crystal was used to characterize the

pulses. The spectrograms are shown in Figs. 3.9a and 3.9b, the G-error is 1.5 % [69]. For this cell, it is clear from the spectral phase, Fig. 3.9c (red), and from the satellite pulses in the retrieved temporal profile of the pulse, Fig. 3.9d, that uncompensated third order dispersion effects are dominant. This arises not only from the limitations of the chirped mirrors PC1691 used in the cell but also from the high nonlinear-phase-shift in each pass of the cell, which cannot be compensated by the GDD of the dispersive mirrors.

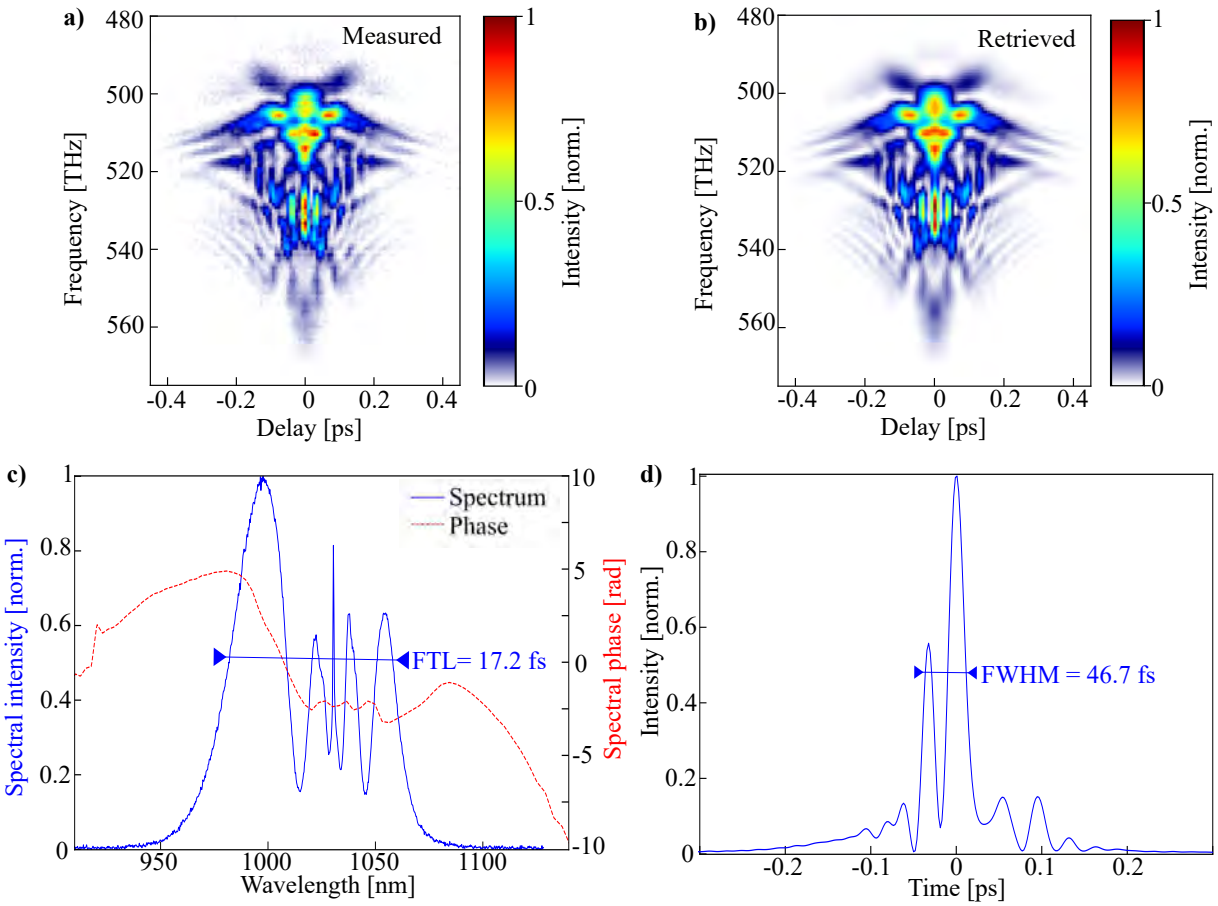

Figure 3.9 **a)** Measured and **b)** retrieved SH-FROG spectrograms of the first generation, first multipass cell output (G-error = 1.5 %). **c)** Measured spectrum (blue) and retrieved spectral phase (dashed red). The FTL reported in the graph is calculated from the FWHM of this spectrum. **d)** Retrieved temporal profile. The FWHM of this curve, corresponding to the effective pulse duration, is reported in the graph.

After the first MPC, the compressed pulses are sent to a second mode-matching setup with similar configuration: a beam expander, (165-1181, EKSMA Optics UAB) and a focusing concave mirror with ROC = 1200 mm. The setup of this second cell is similar to the first one. With the aid of a scraper mirror, the beam is coupled into and focused in the middle of a MPC containing two curved dispersive mirrors with ROC = 250 mm and a 6.35 mm-thick, anti-reflection coated, fused-silica plate as the nonlinear medium. The concave mirrors in this stage, PC1821 in Fig. 3.8, have an average GDD of $-150\,\mathrm{fs}^2$ over 450 nm spectral bandwidth. A curved dispersive chirped mirror is used to re-collimate the beam reflected back to the scraper. The output spectrum after 6 passes through

the nonlinear medium is shown in Fig. 3.10c. At this stage the accumulated linear and nonlinear phases are negligible as the number of passes is small compared to the previous cell. The output pulses are sent to a chirped mirror compressor containing only 3 mirrors with the same dispersive design as the previous compressor, PC1611 reported in Fig. 3.8.

The characterization of the output pulses is carried out via SH-FROG. The spectrograms of the output pulses are shown in Fig. 3.10a and 3.10b. The G-error is 1.3 %. In Fig. 3.10d, a single satellite pulse is noticeable in the time domain. Thus, the uncompensated third order dispersion effects from the first cell are drastically reduced after the second cell. Nevertheless, the spectral bandwidth is comparable with the previous stage. Stated otherwise, this second cell is mainly employed to re-compression stage to mitigate the uncompensated nonlinear dispersion from the previous stage.

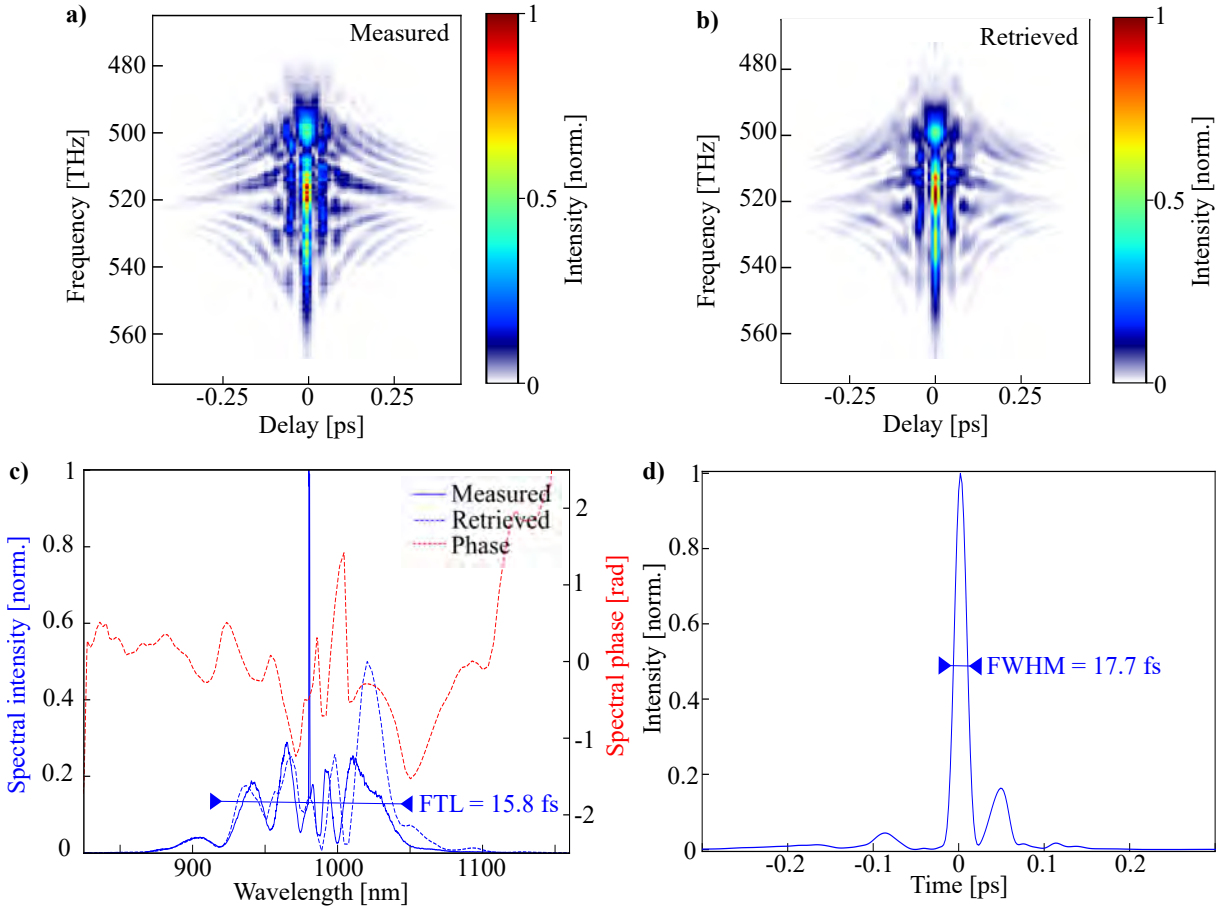

Figure 3.10 **a)** Measured and **b)** retrieved SH-FROG spectrograms of the first generation, second multipass cell output (G-error = 1.3 %). **c)** Measured (solid blue line) and retrieved spectrum (dashed blue line). The FTL reported in the graph is calculated from the FWHM of this spectrum and reported in the graph. The red dashed line shows the spectral phase. **d)** Retrieved temporal profile. The FWHM of this curve, corresponding to the effective pulse duration, is reported in the graph.

In summary, the described compression scheme delivers 18 fs pulses with a total energy of 3.8 µJ, corresponding to 60 % optical efficiency. The temporal domain shows a not-optimal compression but the high intensity and the large spectral bandwidth allowed already important investigations, in particular regarding further compression [70] (Chapter 4) and spectroscopic applications [13] (Chapter 5).

3.2.2 Second generation

Although, the first generation of MPCs-based compression scheme was used for some important investigations [13, 70], the stability of the system and the temporal re-compression were not optimal. Substantial improvements were made in order to employ this compression stage as stable and reliable frontend for the generation of ultrashort pulses and for the final achievement of spectroscopic applications, as can be seen in the following chapters.

Fig. 3.11 shows the layout of the improved nonlinear compression scheme for the generation of sub-20 fs pulse durations based on two consecutive MPCs in Herriott geometry.

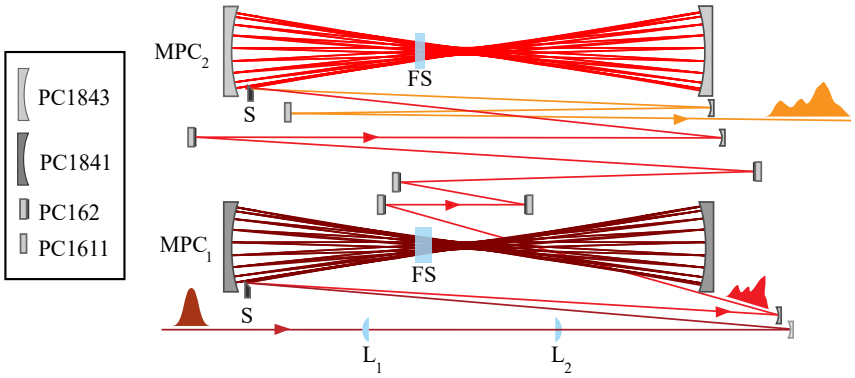

Figure 3.11 Schematic layout of the second generation of compression scheme based on multipass cells in Herriott type geometry. The 5.2 µJ beam from the oscillator is coupled into a first MPCs containing 6.35 mm fused silica medium (FS) and two curved dispersive mirrors (PC1841). The mode matching is achieved via two lenses (L_1 and L_2), a focusing mirror and a scraper (S). After 34 passes through the medium the beam is coupled out and re-collimated. The broadened output is compressed via 8 passes on a chirped mirrors (PC162). After the first cell, the beam is mode-matched into a a second MPCs containing 3 mm fused silica medium (FS) and two curved dispersive mirrors (PC1843). It is coupled out after 22 passes. The broadened output is compressed via 2 bounces on a chirped mirror compressor (PC1611).

Before the first MPC, 5.2 µJ, 84 W pulses of the oscillator are first sent to a mode-matching setup. The remaining available power from the oscillator is employed for other experiments and a small portion for diagnostics of the oscillator. For this setup, the mode matching scheme includes two plano-convex lenses (NIR-II, Edmund Optics Inc) and a focusing concave mirror with ROC = 1500 mm. This new scheme for mode-

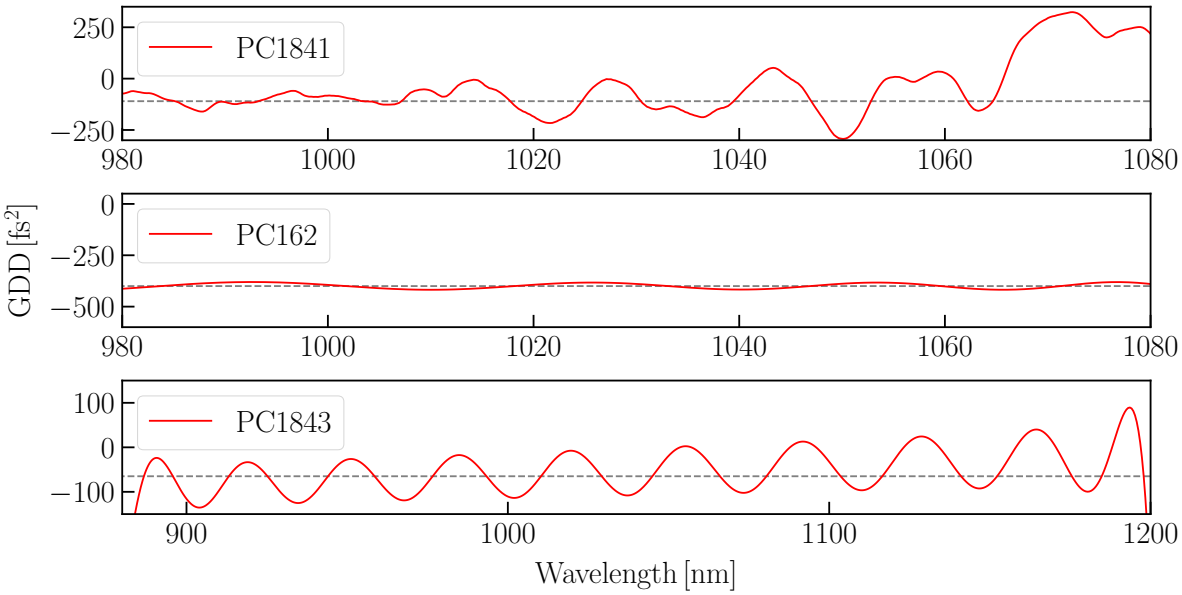

Figure 3.12 Group delay dispersion curves (red) and relative average (gray) for the chirped mirror used in the second generation of MPCs-based compression: the coating named PC1841 is used in the first cell, the coating PC162 is used for the compressor after the first cell, the coating PC1843 is used in the second cell. For compressor after the second cell, mirror with coating PC1611 are used.

matching avoids possible beam distortions due to the fixed and closed geometry of the beam expander. Generally, the beam expander allows for an easier and faster tunability. However, the closed structure and the limited aperture of the lenses inside the beam expander can cause spatial distortion of the beam profile. An impeccable beam profile is a fundamental prerequisite for imaging systems, especially for MPCs where the beam path extends for almost 20 m. In the previous generation of the multipass cell-based compression scheme, a careful positioning of the beam expander was required. This, however, could still result in imperfections in the output beam. Thus, for the new generation a two-lens system was preferred. The longer time required for adjustment was compensated with an always impeccable output beam profile. This can be seen from a comparison of the M^2 parameters for the two generations of compression schemes, Figs. 3.13 and 3.14.

After the mode-matching setup, the beam is coupled into the MPC. The coupling is achieved with a scraper mirror as for the other cells. This cell contains two curved dispersive mirrors with ROC = 300 mm, and average GDD = $-110\,\mathrm{fs}^2$ for 200 nm spectral bandwidth centered at 1030 nm. This GDD curve of the dispersive coating, PC1841, is shown in Fig. 3.12. A 6.35 mm-thick, anti-reflection coated, fused-silica plate is used as the nonlinear medium. After 34 passes through the medium, the beam is coupled out by the scraper and re-collimated by a dispersive curved mirror. The output of this stage is shown in Fig. 3.15c. In contrast to the first generation setup, the first MPC here

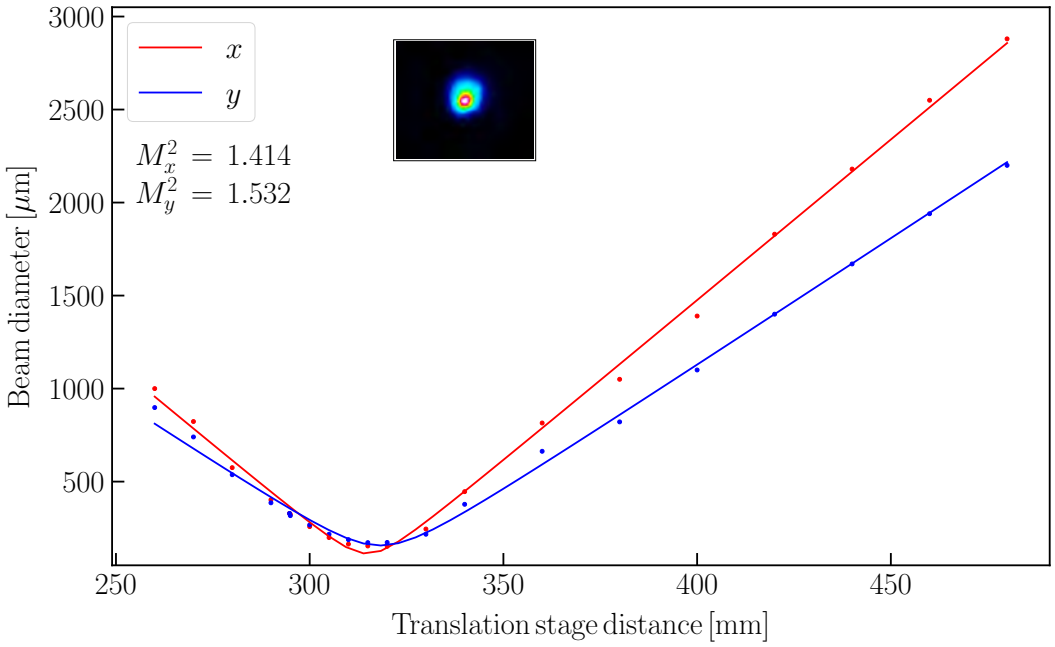

Figure 3.13 M^2 measurement for the first generation of multipass-cells based braodening. As reported in the graph, the values are 1.414 and 1.532, in x and y axis respectively. The measurements are performed after the second cell.

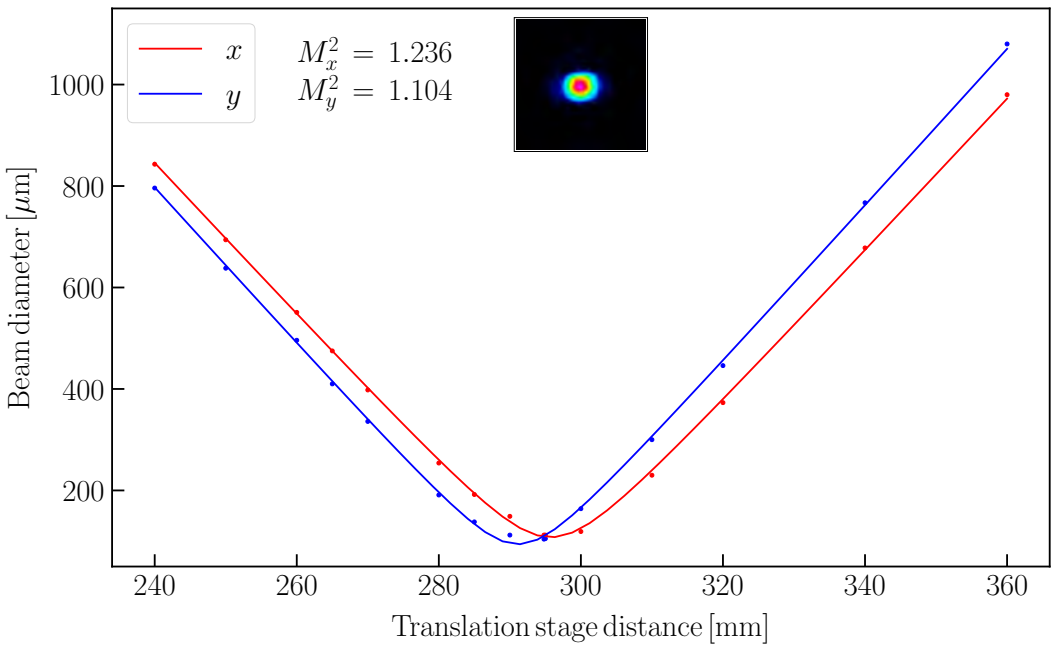

Figure 3.14 M^2 measurement for the second generation of multipass-cells based broadening. As reported in the graph, the values are 1.236 and 1.104, in x and y axis respectively. The measurements are performed after the second cell.

carries out just a partial broadening of the input pulses. As in the previous generation, at this point increasing the number of passes in this stage does not lead to higher spectral

broadening, due to the accumulation of uncompensated linear and nonlinear phase at each round trip. The output pulses of this first stage are coupled out and compressed to 49 fs by using 8 additional dispersive mirrors (PC162, cf. Fig. 3.12) compensating the total residual dispersion of 2400 fs^2 around 1030 nm. The characterization of the output pulses is performed via SH-FROG. Figs. 3.15a and 3.15b show the measured and retrieved spectrograms, with G-error of 0.4 %. The lower shift-per-pass and the improved design of the dispersion curve for the mirrors PC1841 in the cell ensured a much more accurate re-compression of the output pulse in temporal domain. This can be seen from the pulse profile in the temporal domain, Fig. 3.15d. Additionally the flat, smooth phase in the spectral domain, Fig. 3.15c, shows the perfect compensation of the residual chirp from the compressor after the cell. Moreover, the limited bandwidth of the chirped mirrors provided a higher throughput in this stage. This is a direct consequence of the lower numbers of layers used to fabricate the chirped mirrors for the cell. The optical efficiency in this stage is 84 %.

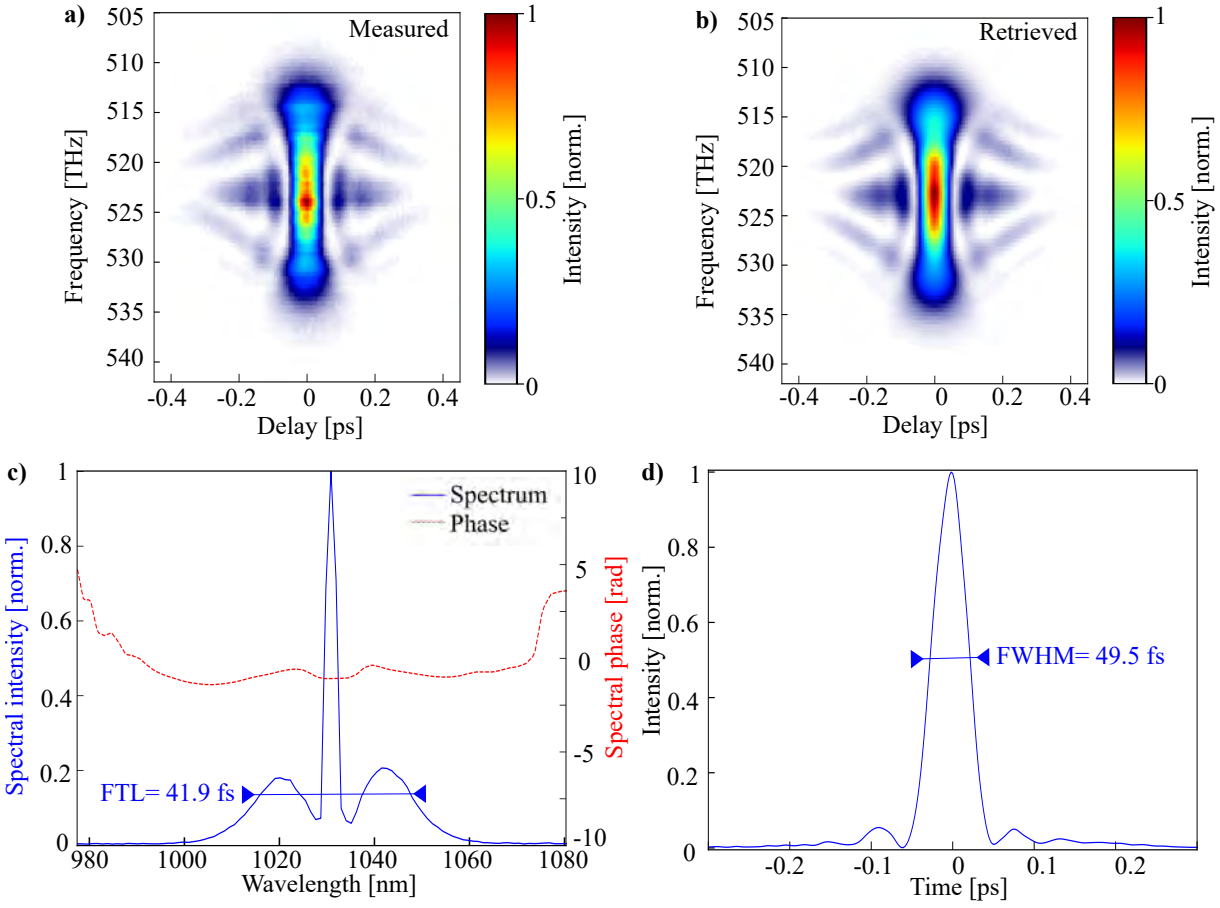

Figure 3.15 a) Measured and **b)** retrieved SH-FROG spectrograms of the second generation, first multipass cell output (G-error = 0.4 %). **c)** Measured spectrum (blue) and retrieved spectral phase (red). The FTL reported in the graph is calculated from the FWHM of this spectrum and reported in the graph. **d)** Retrieved temporal profile. The FWHM of this curve, corresponding to the effective pulse duration, is reported in the graph.

In contrast to the previous generation, the compressed pulses from the first cell are focused into the second cell with the aid of only a dispersive concave mirror with ROC = 1200 mm. This was possibile because the re-collimation beam after the first MPC has a beam waist equal to the one for correct mode-matching. As discussed before the mode-matching can degrade the output beam, especially in this case where also the second MPC has a long propagation length. With the aid of a scraper mirror, the beam is coupled into and focused in the middle of a MPC containing two curved chirped mirrors PC1843 with ROC = 300 mm, and an average GDD of $-60\,\mathrm{fs}^2$ for 350 nm spectral bandwidth, Fig. 3.12. A 3 mm-thick, anti-reflection coated fused-silica plate is used as the nonlinear medium. The beam is reflected back to the scraper and re-collimated after 22 passes through the medium.The output spectrum is shown in Fig. 3.16c. The output pulses are sent to a compressor containing 2 dispersive chirped mirrors, PC1611 in Fig. 3.8, with $-110\,\mathrm{fs}^2$ GDD per bounce. Fig. 3.16d shows the temporal profile of the re-compressed pulses, measured via SH-FROG. The measured and retrieved spectrograms are shown

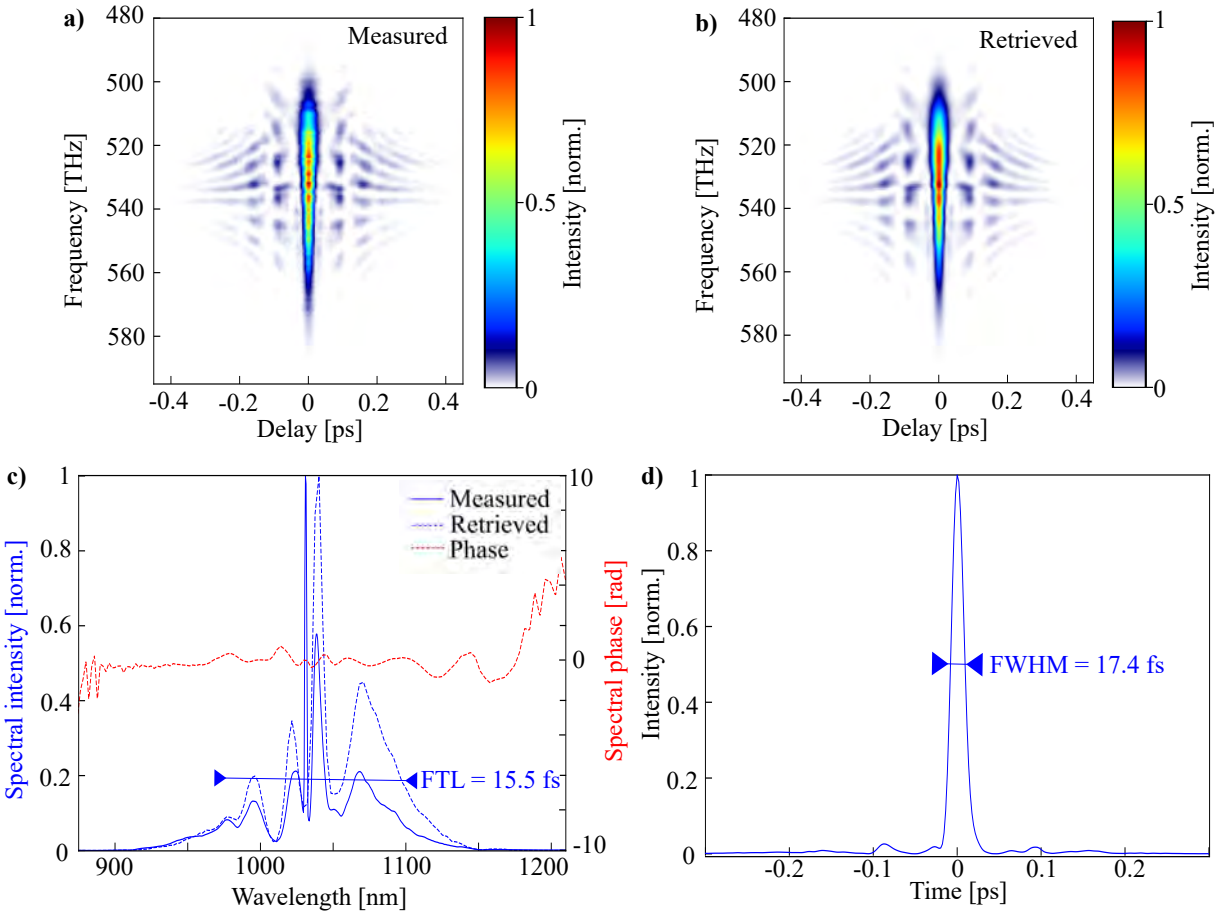

Figure 3.16 a) Measured and **b)** retrieved SH-FROG spectrograms of the second generation, second multipass cell output (G-error = 0.5 %). **c)** Measured (solid blue line) and retrieved spectrum (dashed blue line). The FTL reported in the graph is calculated from the FWHM of this spectrum and reported in the graph. The red dashed line represents the spectral phase. **d)** Retrieved temporal profile. The FWHM of this curve, corresponding to the effective pulse duration, is reported in the graph.

in Figs. 3.16a and 3.16b, respectively. The G-error is 0.5 %. From the comparison with the output pulses of the previous generation, it can be stated that the total bandwidth is maintained while the quality of the compression is drastically improved. The total optical efficiency is also improved to above 80 %.

In summary, the described frontend delivers 17 fs pulses with the total energy of 4.5 µJ, and a total average power of 72 W corresponding to 80 % optical efficiency. The compression is optimized and served to improve the reliability of the following stage of pulse compression scheme for the generation of sub-10 fs pulses (see Chapter 4).

3.2.3 Comparison

For the second generation of MPC-based spectral broadening and pulse compression substantial optimizations has been made. The improvements are both optical and opto-mechanical.

Among the optical upgrades, the major improvement can be understood from the output temporal profile comparing Figs. 3.10d and Fig. 3.16d. An optimized design of the linear, from the chirped mirrors design, and nonlinear phase along the MPCs is the key of this improvement. To obtain the dispersion curve for the design of the chirped mirrors, the measured temporal profile of the oscillator, Fig. 2.6d, has been used as input for simulations based on the split-step Fourier method developed from the *PyNLO* package described earlier (see section 3.1.1.1). The output temporal profile as well as the output spectrum for each cell in the second generation is a priori simulated using theoretical curves for the GDD of the chirped mirrors. After mirrors, with suitable design, had been fabricated and characterized [77], the simulations are repeated with the measured GDD curve. A comparison of simulated and measured output can be seen in Fig. 3.17 for the second cell of the new generation. The figure as well as the calculated pulse durations show excellent agreement between experimental data and simulations. This proves that this simulation algorithm is a valid tool for the design of efficient extra-cavity nonlinear broadening based on MPCs.

Furthermore, the second MPC of the second generation setup is designed to have a reduced nonlinear-phase-shift in each pass through the medium. This is obtained by reducing the thickness of the medium from 6.35 mm to 3 mm. Taking into account the higher intensity in the second cell, which has an input pulse duration almost 5 times shorter than the first one, the reduction of the shift per pass leads to an easier pulse re-compression after the cell, a more robust setup against self-focusing effects and avoided

frequent damages of the medium.

In addition, a better distribution of the broadening between two cells is achieved. For the first generation, the majority of the spectral broadening was achieved in the first cell and the main function of the second cell was to mitigate uncompensated third order phase effects. In the second generation, both cells broaden the pulses and compress them. This advancement also made possible a reduction in required bandwidth of the chirped mirrors used in the MPCs. Not all the mirrors are required to have a GDD and reflectivity curve as broad as the final output pulses. This greatly reduced the demands on the multi-layer structure of the chirped mirror and for this reason a curve closer to desired design is achieved. This also significantly improved the reflectivity of the mirrors, where the optical throughput was increased from 60 % to 80 %.

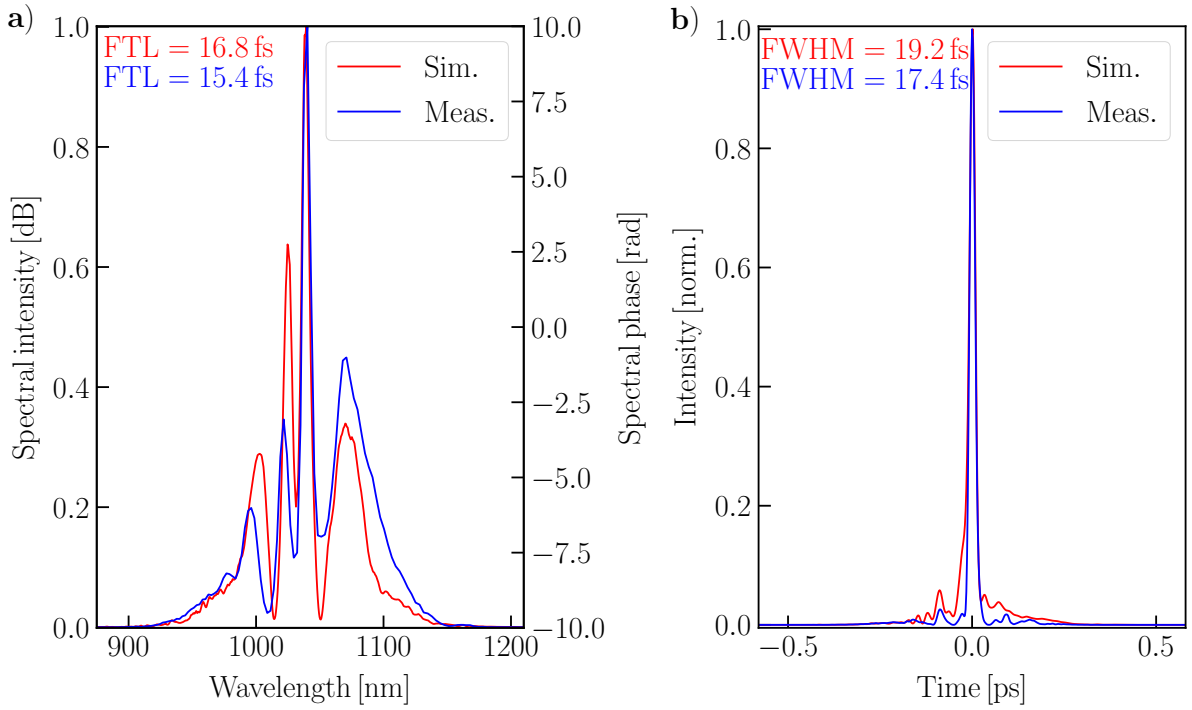

Figure 3.17 a) Measured (blue) and simulated (red) spectrum of the second MPC output for the second generation of sub-20 fs pulses. The FTL is calculated from the FWHM of this spectrum and reported in the graph. **b)** Measured (blue) and simulated (red) temporal profile. The FWHM of this curve, corresponding to the effective pulse duration, is reported in the graph.

About the optomechanical improvements two major changes were made. Firstly, a custom air-tight chamber is employed. A better long-term stability and a reduction of air fluctuations are ensured by this chamber. Additionally, the possibility to water-cool the breadboard of the chamber and the medium of each MPC drastically reduces the thermal drifts. Secondly, two different beam pointing stabilization systems (MRC Systems GmbH) have been used. In the first generation only a simple setup, after the second cell, was implemented (MRC Systems GmbH). The pronounced and continuous thermal drift

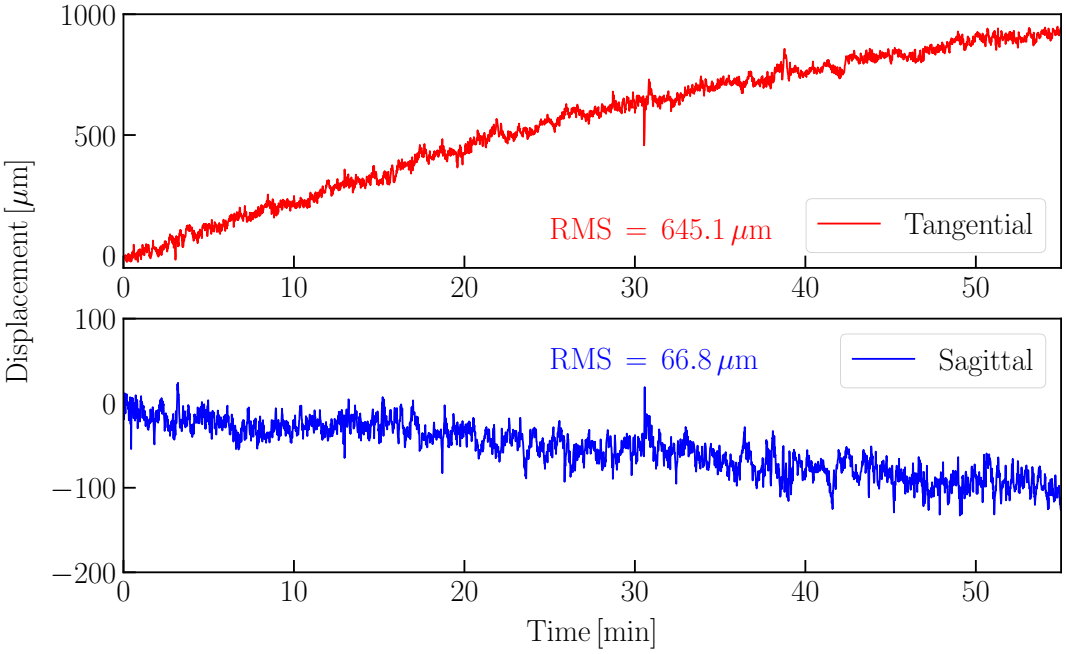

Figure 3.18 Sagittal and tangential position beam pointing deviations for the first generation of multipass cells-based compression scheme output measured over a time frame of approximately 1 h.

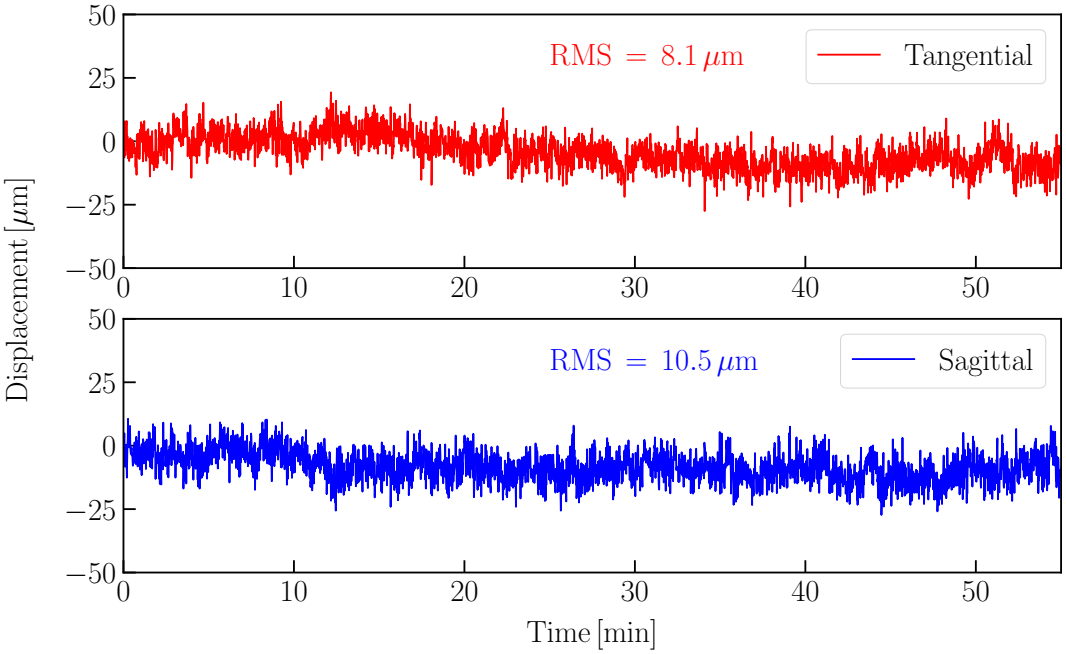

Figure 3.19 Sagittal and tangential position beam pointing deviations for the second generation of multipass cells-based compression scheme output measured over a time frame of approximately 1 h.

could not be compensated within the range of that beam stabilization system. For the second generation, two independent beam stabilization systems are used. The first beam

stabilization system is placed at the oscillator output, i.e. before the first cell. The second beam stabilization systems is placed after the chamber, i.e. after the second cell. In combination, these two stabilization systems and the better cooling drastically improved the beam pointing stability of the second generation of MPCs [84]. This improvement is shown by the comparison of the positional beam pointing fluctuations, in both generations, for approximately one hour, cf. Figs. 3.18 and 3.19. In the first generation a pronounced and uncompensated drift, especially along the tangential axis, not present in the second generation can be seen. Moreover, considering a longer time scale, the day-to-day performances and stability are more reproducible and less damages occurs, so less frequently realignment of the system is required for the second generation.

3.3 Conclusion

In conclusion, two different generations of MPC-based spectral broadening and pulse compression setups were presented. A summary of the most relevant parameters of each generation can be found in Tab. 3.1. Both of these frontends could routinely deliver sub-20 fs pulses at high power. For the first generation an optical efficiency of 60 %, corresponding to 3.8 µJ per pulse, and with durations reaching 18 fs was achieved. The second generation was optically and opto-mechanically improved to reach 80 % optical efficiency, corresponding to 4.5 µJ per pulse, and with durations reaching 17 fs. Another remarkable improvement of the second generation is the pulse compression quality. The pulses after the second cell are re-compressed at almost the FTL pulse duration, making this new generation the perfect input for a second nonlinear compression stage to reach into the sub-10 fs regime.

	First generation	**Second generation**
Average power	60.5 W	72 W
Pulse duration	18 fs	17 fs
Energy	3.8 µJ	4.5 µJ
$\mathbf{M}^2_{x,y}$	1.414, 1.532	1.236, 1.104
Beam-pointing deviations (RMS)	356 µm (1 h)	9.3 µm (1 h)

Table 3.1 Summary of the most relevant parameters for each generation of multipass cells-based broadenings.

Although this type of broadening requires long beam paths and high intensities, both generations of pulse compression schemes show high stability and reliability. This efficient extra-cavity broadening based on pulse compression schemes in bulk material, proved once more, in the experiments outlined here, to be suitable for extending the bandwidth of Yb:YAG-based laser systems while maintaining high optical efficiency. The

limitations in manufacturing multi-layer optics remain the main restrictions for extending the bandwidth of this broadening scheme. For further pulse compression, different techniques can be used to overcome these limitations, as can be seen in the next chapter.

4 Compression to the sub-10 fs regime with different schemes

In the previous chapter, the generation of sub-20 fs pulses with a high optical efficiency in a MPC-based compression scheme is presented. The limitations in manufacturing dispersive optics are the main restrictions for extending the bandwidth of this type of compression. To overcome these restrictions and reach the few- and even single-cycle regime, different techniques can be used.

One promising approach to generate few-cycle pulses from femtosecond lasers at microjoule energy level is nonlinear pulse compression in gas-filled PCFs [31, 87]. The key feature of nonlinear fibers, is the possibility to generate and propagate a soliton, by the simultaneous occurrence of nonlinearity and anomalous dispersion. Although, fiber-based techniques can reach the few cycle regime, they come with several disadvantages. In case of small core diameters, ionization can easily occur and damage the fiber tip. In case of a fiber damage, replacement and coupling can be time consuming [84]. Additionally, fibers are very sensitive to incoupling and misalignments. If the final pulse parameters can only be reached after several compression stages, insensitivity to alignment becomes a key requirement. Alternatively, bulk-based compression schemes have some major advantages such as simple operation, high reproducibility and compact design [49].

Different bulk-based compression schemes can be used to overcome the limitations of dispersive optics [36, 38]. Among them, the compression based on SF in thin plates pose several advantages. The compact and relatively simple setup required gives great adaptability to this compression scheme. Additionally, the simple operation and high reproducibility are key advantages for day-to-day use of the setup. Moreover, beam quality degradation and spatially inhomogeneous spectral broadening can be overcome with a precise adjustment of the length of the nonlinear medium and the input beam diameter and divergence.

This chapter discusses two compression schemes, which are capable of generating few-cycle pulses from the frontend presented previously. In the first part, optical fiber technology is used to generate sub-5 fs pulses by soliton self-compression. In the second part, self-focusing is exploited to generate sub-10 fs pulses in bulk-based quasi-waveguides. In the following, both compression schemes are presented after a brief theoretical introduction.

4.1 Fiber-based compression

In the last decades, many developments in nonlinear optics have strongly benefited from the use of fibers. Optical fibers can be fabricated in a great variety of designs: they can be made from silica glass, soft glass, a combination of them or even polymers; they can be step-index or microstructured; the core can be solid or hollow [88].

Optical fibers which provide guidance for broadband pulses and weak dispersion, are of great interest in nonlinear optics [89]. Fibers with a hollow core can be filled with different media to tailor their linear and nonlinear characteristics [90]. The dispersion control is possible through the waveguide dispersion imposed by the geometry of the fiber and the material dispersion imposed by the material in which the light propagates [88]. Relevant for this work are gas-filled hollow-core fibers. Two main categories of hollow-core fiber with their main characteristics and limitation will be briefly and qualitatively summarized in the following.

Hollow-core capillaries. In the last decades, capillaries, whose structure is shown in Fig. 4.1a, have been vastly used in the field of nonlinear optics. They are mainly used in combination with millijoule-level femtosecond pulses [91]. The light guidance in capillaries is due to grazing incidence reflection [91]. Thus, in capillaries, the loss of the fundamental mode scales as the inverse cube of the core diameter [92], becoming high for diameters smaller than 150 µm. Typically core diameters around 250 µm are used for light at ≈1 µm wavelength. The loss for these capillaries is approximately $1\,\mathrm{dB\,m^{-1}}$. Whereas for capillaries with core diameter of 50 µm the loss is $120\,\mathrm{dB\,m^{-1}}$ [93]. This limitation has an important consequence for the application in this work: because of the large core, equivalent to loose focusing of the input beam, high energy, above 100 µJ, is needed to achieve significant intensity (hence significant nonlinearities). At the same time, the large core allows the capillaries to handle very high energy pulses [88]. Femtosecond pulses at multi-mJ level are commonly used without inducing damage. This feature makes capillaries suitable for applications like spectral broadening of highly energetic pulses [94], high-harmonic generation [91] and laser plasma acceleration [95]. Nevertheless, this type

of fibers are not suited for the relatively low pulse-energy of the frontend used in this work.

Photonic crystal fibers. Gas-filled hollow-core PCFs are a promising approach to overcome the limitations imposed by hollow-core capillaries for pulses at lower energy. This type of fibers allows smaller core diameters than capillaries and has been used to demonstrate nonlinear pulse compression at tens of microjoules [31, 32]. Widely used examples of PCF are hollow-core Kagomé and single-ring PCF. Their structures are shown in Fig. 4.1b and 4.1c, respectively. Despite their different structure, Kagomé and single-ring PCFs have the same guidance mechanism based on anti-resonant reflection and similar dispersion properties [96]. In contrast to capillaries, PCFs can provide low-loss guidance for broadband pulses for smaller core size. Their core diameter is typically in the range between 20 µm to 100 µm [32]. In both designs, the hollow core is surrounded by a periodic cladding structure formed by thin silica elements. In the Kagomé PCF, the cladding is formed by a star-of-David pattern, while in the single-ring PCF, it is formed by thin-walled capillaries. In both fibers, mechanical stability is provided by a thick outer glass tube, called jacket [88]. Kagomé PCF was the first hollow-core PCF reported for guidance of broadband pulses [31]. Single-ring PCFs [97] have gained popularity in the recent years, due to their excellent guidance properties and simple structure. The linear and nonlinear response of these fibers can be altered by filling its hollow-core with various types of gas at different pressures. This design decreases the required pump energies to the microjoule level, which means that megahertz repetition rates can be employed at moderate average power. These versatile structure make them an ideal platform for ultrafast nonlinear optics at megahertz repetition rate [98].

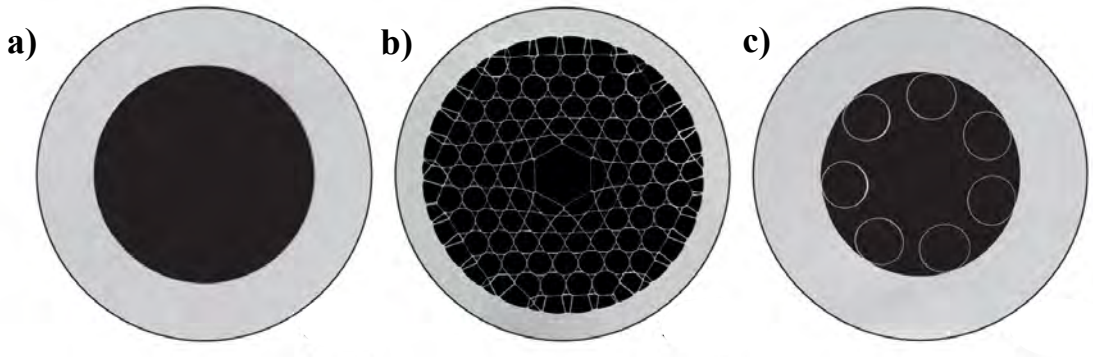

Figure 4.1 Geometrical depiction of different types of hollow-core fibers (not to scale). **a)** Capillary. **b)** Kagomé photonic crystal fiber. **c)** Single-ring photonic crystal fiber. Adapted from [88].

4.1.1 Soliton formation

The key feature of nonlinear fibers, as PCFs, is the simultaneous occurrence of nonlinearity (section 3.1.2) and anomalous dispersion (section 3.1.1) along the pulse propagation. These two effects are generally separated: in a solid core capillary or in a bulk medium, for example, the nonlinear effects in the medium broaden the spectrum of the incident pulse and the dispersion is compensated afterwards with additional optics, as chirped mirrors or gratings [38, 91].

If dispersion and nonlinearties compensate each other throughout the pulse propagation, the pulse does not change along its propagation direction or it exhibits a periodical behaviour. In this case, the pulse is called *soliton*. For simplicity, in what follows, only one-dimensional Schrödinger solitons, which are solutions of the one-dimensional NLSE, Eq. 3.14, will be discussed [93]. To explain the soliton formation, it is expedient to first describe dispersion and nonlinearity separately.

From the NLSE in absence of nonlinearities, it is possible to derive the *dispersion length*. This is the distance at which the envelope of a bandwidth-limited input pulse of duration τ_0 is broadened by a factor $\sqrt{2}$ in absence of nonlinearities. It is defined by

$$L_D = \frac{\tau_0^2}{|k_2|} \tag{4.1}$$

where k_2 describes the GDD. The nonlinear effects are described in a similar fashion. From the solution of the NLSE in absence of dispersion ($k_2 = 0$), it is possible to define the *nonlinear interaction length*

$$L_{NL} = \frac{1}{\gamma P_{\text{peak}}} \tag{4.2}$$

where P_{peak} denotes the peak power of the input pulse and γ is the nonlinear parameter, Eq. 3.15. Similarly to the dispersion length, the nonlinear interaction length describes the distance at which the input pulse is broadened in absence of dispersion [72, 73].

The evolution of a soliton is governed by the relative strength of dispersion and nonlinearity. The soliton order is defined by

$$N = \sqrt{\frac{L_D}{L_{NL}}} = \sqrt{\frac{\gamma P_{\text{peak}} \tau_0}{|k_2|}}\,. \tag{4.3}$$

Depending on the soliton order, linear pulses ($N \ll 1$), fundamental solitons ($N = 1$) and higher-order solitons ($N \geq 2$) can be distinguished. The peak power required to excite an Nth-order soliton is N^2 times the power for a fundamental soliton. For fundamental

solitons ($N = 1$), the nonlinear phase coming from SPM and the GDD exactly cancel each other and the soliton is propagation invariant [73]. Thus, the temporal pulse shape and spectrum do not change upon propagation. Higher-order solitons ($N \geq 2$) have a periodic evolution upon propagation. A remarkable feature of higher-order solitons is self-compression. This can be explained as follows: during the initial part of their propagation, the nonlinear phase coming from SPM is only partially compensated by the GDD coming from the anomalous dispersion. Therefore, the spectrum broadens. In the anomalous dispersion region, the low-frequency components generated by SPM at the leading edge of the pulse have a lower group velocity than the center of the pulse. Similarly, the high-frequency components generated at the trailing edge have a higher group velocity than the center of the pulse. As a result, both get shifted towards the center of the pulse, leading to temporal self-compression [88]. Soliton self-compression is a powerful process that allows direct generation of single-cycle pulses with octave spanning spectra [99].

4.1.2 Experimental setup

The experimental setup for the fiber-based compression scheme is shown in Fig. 4.2. The fiber is placed in a custom-made aluminium chamber formed by two connected parts. To adapt the length of the chamber to the fiber, the length of aluminium tube that connects the two parts of the chamber can be changed.

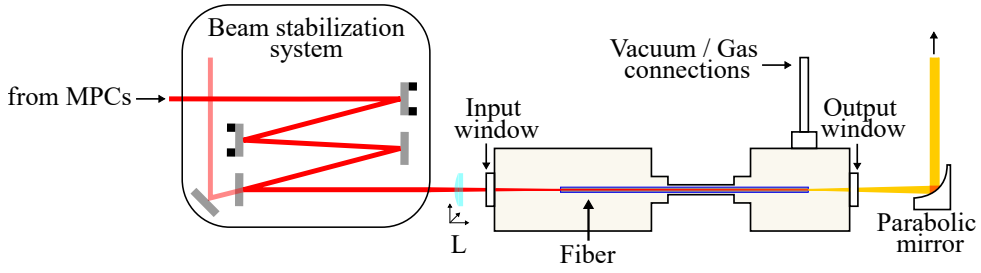

Figure 4.2 Schematic layout of the fiber-broadening setup. The beam from the multipass cells-based broadening is actively stabilized against beam pointing fluctuations and coupled into a two-part aluminium chamber. The chamber is connected to a vacuum pump and a gas inlet. After the chamber the beam is re-collimated by a parabolic mirror. An achromatic lens (L), on a three-axes manual translational stage, is used to focus the beam at the entrance of the fiber. The fiber used in this experiment is a single-ring hollow-core photonic crystal fiber with a core diameter of approximately 55 µm. The gas pressure used for this experiment is 10 bar of krypton.

The output of the first generation of MPCs-based compression, delivering 18 fs pulses with 60.5 W of average power, described in section 3.2.1, serves as input of this fiber-based broadening stage. The input beam is electronically stabilized against beam-pointing fluctuations (MRC Systems GmbH). The mirrors mounted in the actuators of the stabilization setup are chirped mirrors with $-110\,\mathrm{fs}^2$ GDD per bounce. In this way,

the GDD of the focusing lens and of the chamber window are pre-compensated and the MPCs pulses are compressed at the fiber entrance.

To focus the input beam at the entrance of the fiber an achromatic lens, $f = 100\,\text{mm}$ (AC254-100-B-ML Thorlabs Inc.), is used. The lens is mounted on a three dimensional stage (Elliot Scientific Ltd.) to adjust the alignment into the entrance of fiber. The entrance of the chamber is formed by an AR-coated 1-mm-thick fused silica window. The risk of damaging the window is minimized by placing the chamber close to the lens to reduce the peak intensity of the input pulses at the window position.

The second half of chamber has a system of connectors for gas and vacuum. This allows to control the gas pressure and to evacuate the chamber. The evacuation of the chamber prior to the gas filling, is especially relevant for operation at low gas pressures. The control of the nonlinear broadening effects in the fiber is strictly related to the nonlinear refractive index of the gas. Thus, the purity of the gas is a crucial parameter especially at lower pressures.

The output window of the chamber is an uncoated 0.5-mm-thick calcium fluoride (CaF_2) plate. After the fiber, the beam is divergent. To re-collimate the output beam without introducing additional GDD, an aluminium-coated parabolic mirror with a focal length of 200 mm is placed after the chamber.

In this broadening stage, the 75 % of the power from the first generation of MPCs is coupled to a 15 cm-long single-ring PCF (with a core diameter of $\approx$55 µm), filled with 10 bar of krypton for soliton self-compression [87]. The broadened spectrum is shown in Fig. 4.3c, it supports a FTL pulse duration of 4.5 fs. The optical efficiency has a remarkable value of 95 %. This corresponds to broadband pulses with energy as high as 3 µJ.

After the fiber, the re-collimated beam is coupled into a paired chirped mirrors compressor containing 4 mirror with an average GDD of $-150\,\text{fs}^2$ per pair. This compressor is compensating the dispersion along the beam path after the fiber output, including the output window and 1 m of beam path in air before the characterization setup. The temporal characterization of the broadened pulses is shown in Figs. 4.3a and 4.3b. It is performed by a SH-FROG with a 10 µm BBO. The G-error is 1.1 %. The retrieved temporal profile 4.3d shows a pulse duration of 9.6 fs. Although, the broadening is remarkable the temporal compression is not optimal. A prominent pedestal can be seen in the retrieved temporal profile.

In conclusion, the fiber-based pulse compression presented here has proven to

be a promising first attempt to reach the few-cycle regime with this laser source with a hybrid compression scheme. However, the low long-term stability (above 30 min) and the frequent damages of the fiber are the main limitation for the future applicability of this fronted. On contrary, an all-bulk-based approach have already shown to be a reliable tool to reach short pulse durations from this class of oscillators [37].

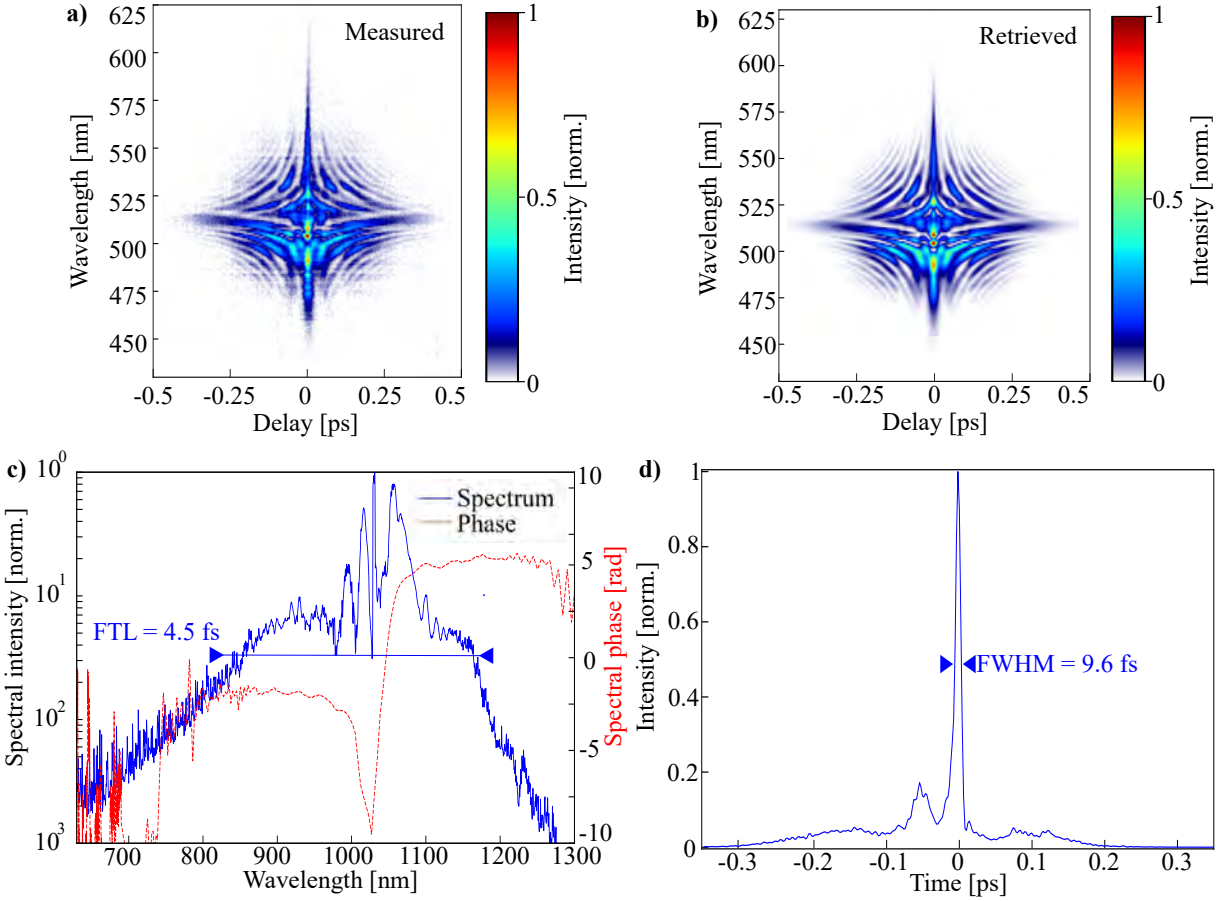

Figure 4.3 **a)** Measured and **b)** retrieved SH-FROG spectrograms of the single-ring PCF output (G-error = 1.1 %). **c)** Measured spectrum. The FTL reported in the graph is calculated from the FWHM of this spectrum and reported in the graph. **d)** Retrieved temporal profile. The FWHM of this curve, corresponding to the effective pulse duration, is reported in the graph.

4.2 Bulk-based compression

In the previous chapter, section 3.1.2, the Kerr-induced nonlinear phenomena were introduced by Eq. 3.17. Particular attention was given to the temporal variation of the refractive index, which leads to SPM. Nevertheless, the nonlinearites of a medium affect both the temporal and the spatial properties of the incident field of light. Any nonlinear interaction strong enough to affect the temporal pulse profile will also affect its transverse profile. In the following theoretical section, a general description of the (transverse) spatial variation of the refractive index, which leads to SF, is presented. A more complete

and rigorous description can be found in several textbooks, some examples are [71, 72, 81].

This theoretical description is followed by a detailed explanation of the experimental setup, including characterizations and simulations of the final results.

4.2.1 Self-focusing

The class of nonlinear optical phenomena in which a beam of light modifies its own propagation by interacting with a nonlinear material are generally called *self-action effects*. Depending on the intensity of the incident beam, three cases of self-action effects can be distinguished.

Self-focusing and self-defocusing. In this case an intense beam modifies the refractive index of a medium causing it to act as a lens. For a Gaussian transverse beam profile, the intensity is higher in the center of the beam and lower on the edge. If the nonlinear refractive index is positive $n_2 > 0$, the higher optical intensities in the centre of the spatial beam profile, as compared to the outer part, cause an effectively increased refractive index for the inner part of the beam. This modification of the refractive index distribution acts as a focusing lens and it is called *self-focusing*, Fig. 4.4a. If the nonlinear refractive index is negative $n_2 < 0$, the modification of the refractive index distribution acts as a defocusing lens, which is called *self-defocusing* on the contrary, Fig. 4.4b.

Self-trapping. In this case, a beam propagates in a nonlinear medium with a constant diameter as consequence of an exact balance between self-focusing and diffraction effects, Fig. 4.4c. This can occur only if the power of the incident beam P is exactly equal to the so-called *critical power for self-trapping*

$$P_{\mathrm{cr}} = \frac{\pi(0.61)^2\lambda_0^2}{8n_0n_2} \tag{4.4}$$

where λ_0 is the vacuum wavelength of the laser radiation, n_0 is the weak-field refractive index and n_2 is the nonlinear refractive index. Since self trapping occurs only for $P = P_{\mathrm{cr}}$, it is intuitive to understand that SF occurs when the incident power is larger than the critical power for self-trapping, $P > P_{\mathrm{cr}}$.

Laser beam breakup. This case occurs for $P \gg P_{\mathrm{cr}}$ as a consequence of imperfections on the laser wavefront and leads to the breakup of the beam into many components each carrying approximately P_{cr}, as in Fig. 4.4d. This process typically leads to the generation of a beam with a random intensity distribution and is often referred to as filamentation [71, 81].

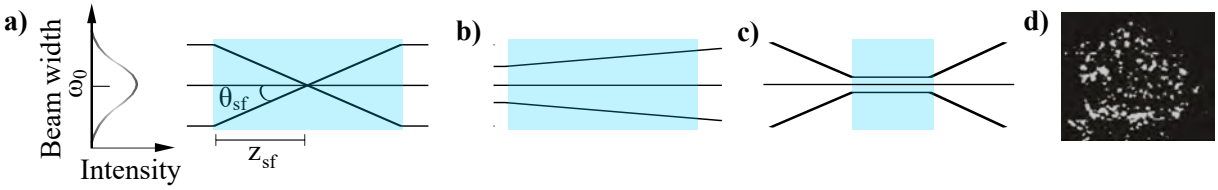

Figure 4.4 Geometrical depiction of different self-action effects. **a)** Self-focusing. For a medium (light blue) with positive nonlinear refractive index, $n_2 > 0$, the higher optical intensities in the center of the beam causes a decreasing refractive index gradient towards the outer parts of the spatial profile. This modification acts as a focusing lens. **b)** Self-defocusing. For a negative nonlinear refractive index, $n_2 > 0$, the higher optical intensities in the center of the beam, causes an increasing refractive index gradient towards the outer parts of the spatial profile. This modification acts as a defocusing lens. **c)** Self-trapping. A beam propagates in a nonlinear medium with a constant diameter as consequence of an exact balance between self-focusing and diffraction effects. **d)** Laser beam breakup. The imperfections on the laser wavefront lead to breakup of the beam into many components (adapted from [71]).

Neglecting diffraction, it is possible to outline a simple model to describe SF. This is justified if the power is sufficiently large to avoid self-trapping, as for the experiments outlined later in this chapter. Fig. 4.4a depicts a collimated beam with radius ω_0 incident onto a nonlinear optical material with positive n_2. In first approximation, it is possible to consider the refractive index along the marginal ray equal to n_0 and along the central ray equal to $n_0 + n_2 I_0$, where I_0 is the on-axis intensity. Employing Fermat's principle, which states that the optical path length of all rays traveling from a wavefront at the input face of the medium to the focus must be equal, it is possible to define the *self-focusing distance* z_{sf} as

$$(n_0 + n_2 I_0) z_{\mathrm{sf}} = \frac{n_0 z_{\mathrm{sf}}}{\cos\theta_{\mathrm{sf}}} \tag{4.5}$$

where θ_{sf} is the angle through which the incident beam is deviated by self-action effects, as in Fig. 4.4a. With the approximation $\cos\theta_{\mathrm{sf}} \approx 1 - \frac{1}{2}\theta_{\mathrm{sf}}^2$ it is possible to calculate

$$\theta_{\mathrm{sf}} = \sqrt{\frac{2 n_2 I_0}{n_0}} \tag{4.6}$$

and, since the ratio $n_2 I / n_0$ is generally small for optical material, the previous approximation is justified [71]. Using this angle, it is possible to derive the self-focusing distance as [71]

$$z_{\mathrm{sf}} = \frac{\omega_0}{\theta_{\mathrm{sf}}} = \omega_0 \sqrt{\frac{n_0}{2 n_2 I_0}} = \frac{2 n_0 \omega_0^2}{\lambda_0} \sqrt{\frac{P_{\mathrm{cr}}}{P}} \,. \tag{4.7}$$

For a beam which varies in both transverse directions, the wave equation describing SF cannot be solved analytically but numerical simulations need to be implemented. In general, for pulsed radiation the self-focusing distance z_{sf} varies according to the value of the instantaneous intensity $I(t)$ at the input facet. Thus, the focal point will sweep through the material as it follows the temporal evolution of the pulse intensity [81].

Previously, for the case of self-focusing and self-defocusing, only collimated beams were considered as input to the medium in which SF is calculated. Different beam divergences can be used at the input facet of the nonlinear medium. This allows to shift the focus position z_{sf} and control the intensity at the focus. Firstly, beam collapse due to laser beam breakup can be avoided if the length of the medium is smaller than z_{sf}. Equivalently, the input beam waist has to be large enough to avoid laser beam breakup but small enough to induce self-focusing. Secondly, the beam divergence can be adjusted to shift the self-focus position. In figure 4.5, three different cases are depicted. In the first case, Fig. 4.5a, the input beam is collimated. Here, for given laser parameters and medium length, z_{sf} can only be adjusted by the input beam waist size. In the second case, Fig. 4.5b, the medium is placed in a converging beam. There, the effect of SF is to shift the focus towards the input facet of the plate. In the last case, Fig. 4.5c, the medium is placed in a divergent beam. Thus, SF leads to a focus at a distance larger than the previous case. For a certain beam divergence and a certain medium thickness, z_{sf} can be outside the plate, as depicted in Fig. 4.5c.

The last case can be exploited in the experiment to shape the caustic of the incident beam such that the first plate leads to a second focus where another plate is placed, which self-focuses the beam again. This process can be repeated several times, until the pulse is stretched by material dispersion and the peak power falls below P_{cr}, such that no further SF can occur. This would lead to a periodic quasi-waveguide [39, 100].

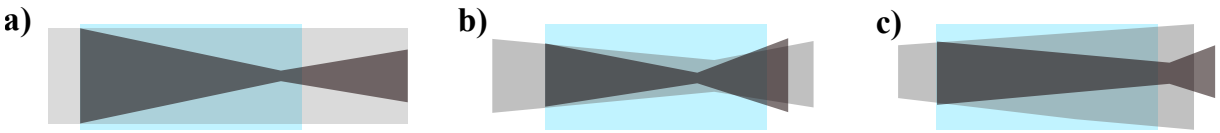

Figure 4.5 Different input-beam divergences (light gray) for self-focusing experiments. The effect of self-focusing is shown in dark grey and the medium in light blue. **a)** The medium is placed in a collimated input beam. **b)** The medium is placed in a focusing input beam where the self focus is shifted towards the input facet of the medium. **c)** The medium is placed in a defocusing input beam and the self-focus is shifted beyond the end facet of the medium.

4.2.2 Experimental setup

As input for this pulse compression setup, the pulses from the second generation of MPCs-based compression scheme, are used. The MPCs compression stage delivers pulses with 17 fs pulse duration, 4.6 µJ energy at 16 MHz repetition rate.

The research described in this chapter was motivated by the necessity to overcome the main limitation of the MPCs compression stage. For pulses shorter than 15 fs, the effects of higher-order dispersion from the bulk material become more pronounced

and the design of the dispersive optics coating for a multipass system is more complicated [101, 102]. Therefore, it can be advantageous to increase the nonlinearity per pass and reduce the amount of dispersive optics. This can be obained with quasi-waveguides that rely on SF [49].

Here, a quasi-waveguide geometry is used in a bulk-based pulse compression scheme to achieve sub-10 fs pulses. The setup can be seen in Fig. 4.6a. A series of four sapphire plates is placed after the focus of a lens with $f = 250\,\mathrm{mm}$. The plate thicknesses are 1 mm for the first plate and 0.5 mm for the other three plates, respectively. After the plates, the beam is re-collimated by a lens and sent to a chirped-mirrors compressor with a total GDD of $-75\,\mathrm{fs}^2$. The distance for each plate is carefully adjusted to balance dispersion effects and SF [84].

For the thin plates setup, the main broadening mechanism is SPM as for the MPCs [38, 39]. For the particular case of the quasi-waveguide shown here, the reduction of intensity due to material dispersion in the first plate is no longer compensated via dispersive optics as for the MPCs. In this case, it is achieved through a reduction of the focus size, equivalent to an increase of peak intensity, induced by the control of SF in each plate, as evident in the simulated caustic reported in Fig. 4.6b. The compensation of dispersion in the MPCs as well as the reduction of focus size in the thin plates are induced to maintain the peak intensity in each pass along the quasi-waveguide. For this reason this scheme can be called *intensity waveguide*. At the input facet of each plate, the beam is divergent, cf. Fig. 4.5c, where the self-focus occurs after the output facet. The propagation in each plate enables SPM and a reduction of the beam size after the plate due to SF. This circumvents the reduction of the peak intensity due to the elongation of the pulse duration induced by material dispersion accumulated during the propagation through the plate. The limit of a single quasi-waveguide setup is reached when the reduction of beam size does not suffice anymore to compensate the pulse chirp and the peak power falls below P_{cr} such that no further SF can occur. Once this point is reached, re-compression, e.g. via chirped mirrors, is required to achieve sufficient peak power to induce further nonlinear effects.

To design such a waveguide, the input peak power and beam divergence are the crucial parameter for choosing the mode size in the nonlinear material. The maximum peak power or equivalently the minimum beam waist for broadening experiments is defined as the value at which laser beam breakup occurs. At this value the beam profile is destroyed and also damage of the medium can occur. Preferably, the peak power should be below the damage threshold throughout the whole crystal. Additionally, Seidel et al. [50] showed that the maximum nonlinear broadening can be achieved by a divergent input

beam. In this way, the focal length of the first lens as well as the position of each plate can be defined. The material and the thickness of each plate, are other crucial parameters for the control of SF in this intensity waveguide. In the following, the material and the thickness studies conducted for this setup as well as the characterization of the system and a comparison between the experiments and simulations are reported [84].

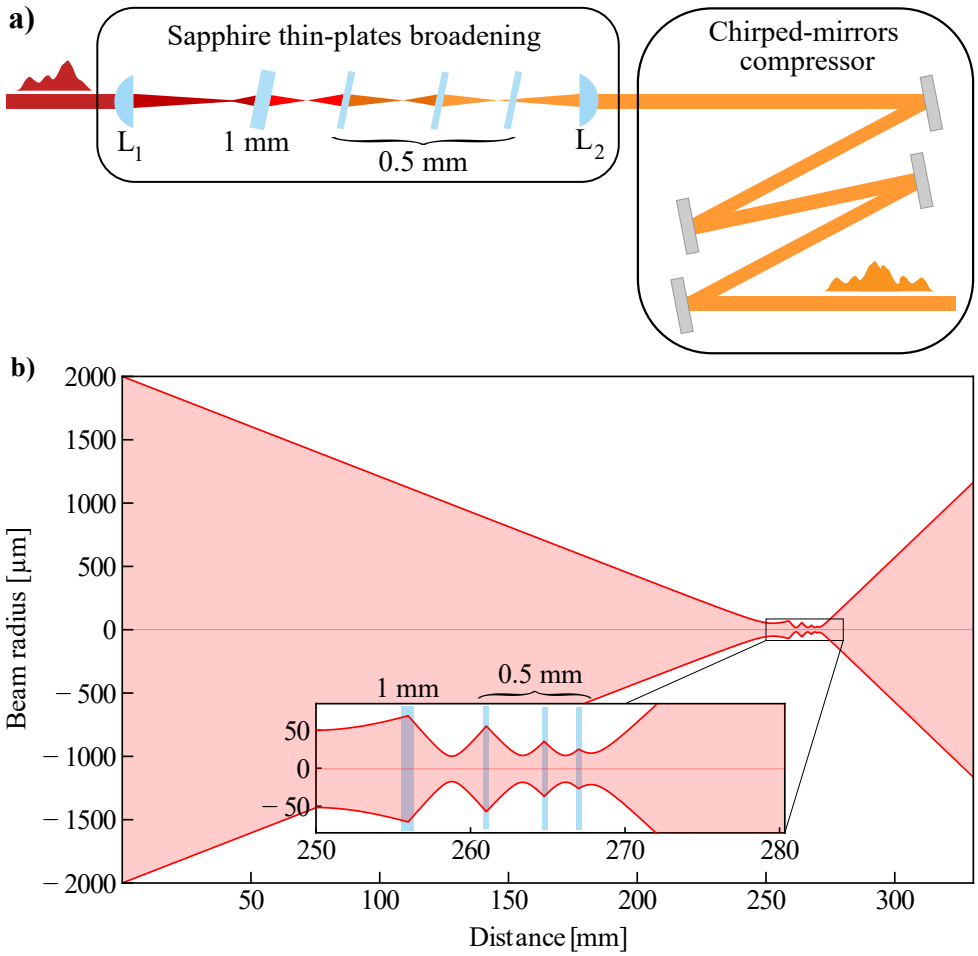

Figure 4.6 a) Thin plates broadening scheme. A series of four Sapphire plates are placed after the focus of a lens with focal length = 250 mm. The plate thicknesses are 1 mm for the first plate and 0.5 mm for the other three plates. After the plates, the beam is re-collimated by a lens and sent to a chirped-mirrors compressor with a total GDD of $-75\,\mathrm{fs}^2$. **b)** Simulated caustic of the input beam after the focusing lens, $f = 250\,\mathrm{mm}$, and along the thin plates setup. The mode radius along the quasi-waveguide is estimated with the software *ReZonator2* [67]. The beam waist at the plates position cannot be exactly measured due to the very small distance between each plate, but the focal length induced by self-focusing is analytically calculated. The input and output beam waists are simulated to reproduce the measured beam waists. In the inset, the positions of the plates are clarified. In the experiment the plates are placed under Brewster's angle, here not shown for simplicity.

4.2.2.1 Material selection

A great variety of materials can be used for spectral broadening. Generally, these materials also need to be easily available in good optical quality and exhibit low intrinsic

absorption in the region of emission. Another important material property is a high thermal conductivity, which avoids damage under high average power irradiation. This is particularly obvious for the case of SiO_2: when focusing a high power laser beam into a fused silica plate, a damage is usually observed after few seconds of high power irradiation; exchanging it with a quartz plate, the damage threshold is higher and, in the case of a damage, it occurs near instantly [49]. When comparing the thermal conductivities of different materials in Tab. 4.1, it is evident that quartz and sapphire are the most suitable choices for thin-plate broadening.

Material	**Composition**	$\mathbf{n_2}$ $[10^{20}\,\mathrm{m^2\,W^{-1}}]$	**k** $[\mathrm{W\,m^{-1}\,K^{-1}}]$
Yttrium Aluminium Garnet	$Y_3Al_5O_{12}$	7.5	13.4
Fused silica	SiO_2	2.19	1.38
Quartz	SiO_2	2.19	140
Sapphire	Al_2O_3	3	46

Table 4.1 Material properties of different bulk material commonly used in self-focusing broadening. Nonlinear refractive (n_2) measured at 1030 nm, thermal conductivity (k). Values taken from [103].

To choose the most suitable material for the quasi-waveguide setup, the broadened spectra obtained with single plates of different materials are compared. Each plate is placed after the focus of a lens with focal length $f = 250\,\mathrm{mm}$ and moved towards the focus till a damage occurs. This is assumed to be the laser beam breakup position. Afterwards the plate is rotated to avoid irradiation on a damage and moved away from this point till the maximum broadening is reached. The beam is re-collimated by an identical lens and a portion of it is sent to a spectrometer. The plates used for this experiment do not have an AR coating, and to avoid back-reflections the plates are placed at Brewster's angle. Broadened spectra from 3 mm plates of different materials are plotted in Fig. 4.7a. As reference, a spectrum with no plates is reported (black). The plates have 3 mm thickness except yttrium aluminium garnet which was only available in 2 mm thickness at the time.

As previously shown in the MPC broadening, fused silica is a suitable material for efficient nonlinear broadening. The low damage threshold, however, prevents achieving the highest broadening factor. Crystalline materials provide a higher thermal conductivity and allow enhancing the spectral broadening by using higher intensities. Theoretically, yttrium aluminium garnet should exhibit the strongest nonlinearities with the higher nonlinear refractive index. However, a strong emission of visible light, correlated with filamentation and damage, prevented the use of yttrium aluminium garnet at higher intensities. As a reasonable compromise between high damage threshold (related to high thermal conductivity) and highest broadening (related to high nonlinear refractive index), sapphire reached the strongest broadening and is therefore chosen as nonlinear material

for the intensity waveguide. Quartz, with the highest thermal conductivity, does not exhibit the highest broadening due to the lower nonlinear refractive index in comparison to sapphire (reported in Tab. 4.1).

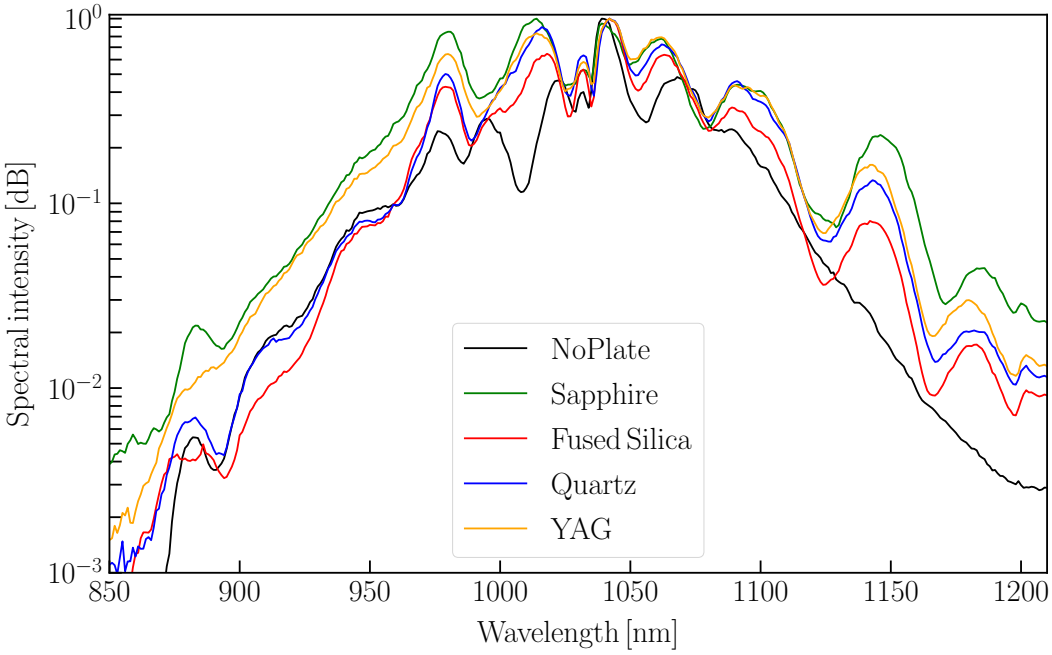

Figure 4.7 Broadest spectrum achieved for different plates: 3-mm-thick sapphire (green), 3-mm-thick fused silica (red), 3-mm-thick quartz (blue) and 2-mm-thick yttrium aluminium garnet (yellow). Each plate is placed after the focus of a lens with $f = 250\,\text{mm}$ and it is moved towards the focus till the broadest spectrum is reached. The beam is re-collimated by an identical lens and sent to a spectrometer. For reference a spectrum with no plate is reported (black).

4.2.2.2 Thickness selection

The thicknesses of the plates are strongly correlated with the waveguiding properties. In the final setup, each plate is placed such that it produces a focus outside its end facet and before the following plate, as previously outlined. Moreover, the dispersion induced by the material of the plate should be controllable such that the induced SF can generate a tighter focus after the plate and the longer pulse duration can be compensated by a decreased beam waist (higher peak power) at the following plate.

To choose suitable plates for an efficient intensity waveguide, different combinations of sapphire plates with thicknesses ranging from 5 mm to 0.25 mm are tested. The highest spectral broadening is achieved with a divergent input beam. The higher the divergence, the higher the required positioning precision for the plate along the beam path. This is a consequence of the smaller range between the two beam radii where the intensity is sufficient for self-focusing and where the intensity is enough for laser beam breakup. The lens focal length is chosen to be 250 mm for 1-mm-thick sapphire plate, such that laser

beam breakup only occurs at the focus for this plate. Additionally, the looser focusing guarantees that the setup is less sensitive to variations of the input power. The plates are positioned following the same procedure described above. Each of them is placed after the focus and moved towards the focus till the highest broadening is reached without resulting in laser beam breakup. At the end of this setup the beam is re-collimated by an identical lens and a portion of it is sent to a spectrometer.

In Fig. 4.8 the resulting spectra for two different combinations of two and three plates are shown. In Fig. 4.8a, the broadening after the second plate is evaluated. The broadening is not clearly higher with a 0.5-mm-thick than with a 1-mm-thick sapphire plate. However, this is more clear in Fig. 4.8b, where the comparison between the same thicknesses for the third plate is shown. The lower dispersion induced by the previous plate enables a broader spectrum for a larger focus size, due to the lower material dispersion. Additionally, less SF is induced, such that a more accurate positioning of the next plate is possible.

To achieve enough SF effects from a low pulse-energy frontend the relative positions between the plates are very small, on the order of 5 mm. This prevents the usual geometry with plates in reciprocal Brewster's angle, as in [102] for example. In this experiment, all the plates are positioned with the same tilting angle. This results in a lower throughput and demands AR-coated substrates for an upgrade of the system.

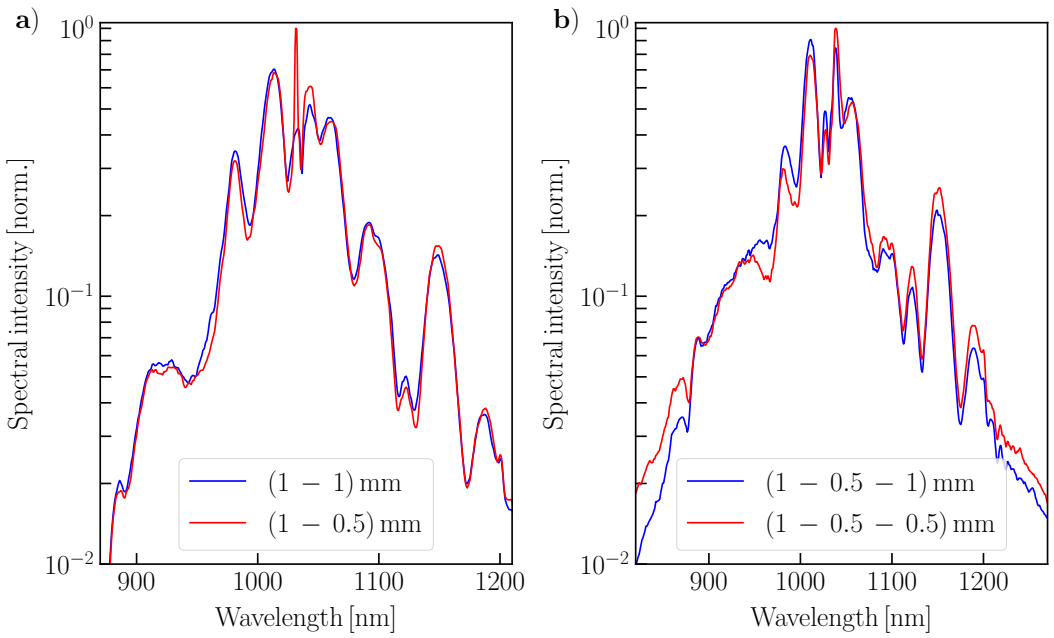

Figure 4.8 The resulting spectra for two different combinations of **a)** two and **b)** three plates. The input beam is focused before the first plate by a lens with focal length 250 mm. The beam after the plates is re-collimated by an identical lens and a portion of it is sent to a spectrometer. In **a)** the broadening in the second plate of the waveguide is evaluated. Similarly in **b)**, the broadening in the third plate is evaluated.

4.2.2.3 Characterization of the final quasi-waveguide setup

The final setup for the intensity waveguide in sapphire thin plates, as shown in Fig. 4.6a and explained previously, consist of four plates with thicknesses of 1 mm for the first one and 0.5 mm for the following three, respectively. Each plate is placed after the focus of the previous plate (except the first one). The output beam is re-collimated by a lens and its temporal profile is re-compressed by a chirped-mirrors compressor consisting of double-angle mirrors with a total GDD of $-75\,\mathrm{fs}^2$. This compensation is necessary to remove the material dispersion introduced by the plates at Brewster's angle, which stretches the pulses to 80 fs. The optical efficiency after the chirped-mirrors compressor is approximately 80 %.

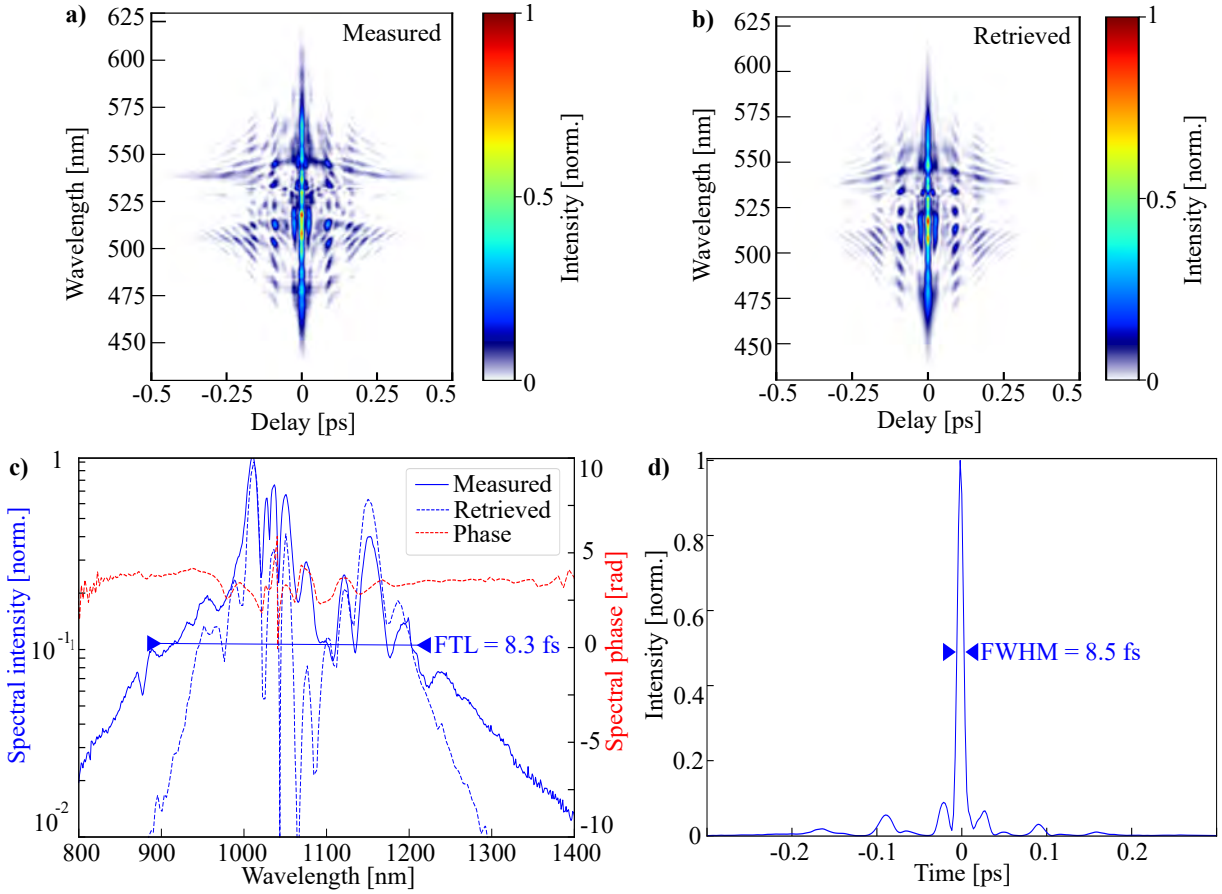

Figure 4.9 a) Measured and **b)** retrieved SH-FROG spectrograms of the thin plates intensity waveguide after the chirp-mirrors compressor (G-error = 0.67 %). **c)** Retrieved spectrum. The FTL reported in the graph is calculated from the FWHM of this spectrum and reported in the graph. The red dashed line represents the spectral phase. **d)** Retrieved temporal profile. The FWHM of this curve, corresponding to the effective pulse duration, is reported in the graph.

The characterization of the pulses after the chirped mirrors compressor is performed via SH-FROG. The measured and retrieved spectrograms, the spectrum and the temporal profile are shown in Fig. 4.9. The temporal profile shows that the pulses could be re-compressed to their Fourier-transform limit. From linearity of the residual spec-

tral phase, can be deducted that the material dispersion induced by the plates could be compensated by the by the chirped mirrors compressor.

In addition to a remarkable temporal re-compression, a high stability and reproducibility of the output is confirmed by the measurements. The average power RMS fluctuations are lower than 0.2 % over a time of one hour, after the system reached the thermal equilibrium (≈1 h). Similarly, the RMS beam pointing fluctuations are low, approximately 3 µrad within 1 hour. For this experimental setup the second beam stabilization systems, after the MPCs system, is not used.

Moreover, the improved spatial beam quality obtained in for the second generation of MPCs compression (cf. Fig. 3.14), is not substantially deteriorated by the SF effects employed for this quasi-waveguide setup. The output beam profile has an M^2 value of 1.290 and 1.401, in x and y axis respectively (ISO 11146 measured with M^2-200s, Ophir-Spiricon LLC), reported in Fig. 4.12. The M^2 value, could be further improved with an increased throughput of the thin plates setup. If a longer input focal length can be used, the distance between the radius at which laser beam breakup occurs and the one at which self-trapping occurs is longer. This would allow a better and easier positioning of the plates after the foci of the caustic, thus a finer control of distortions induced in the beam profile by the self-focusing effects [104].

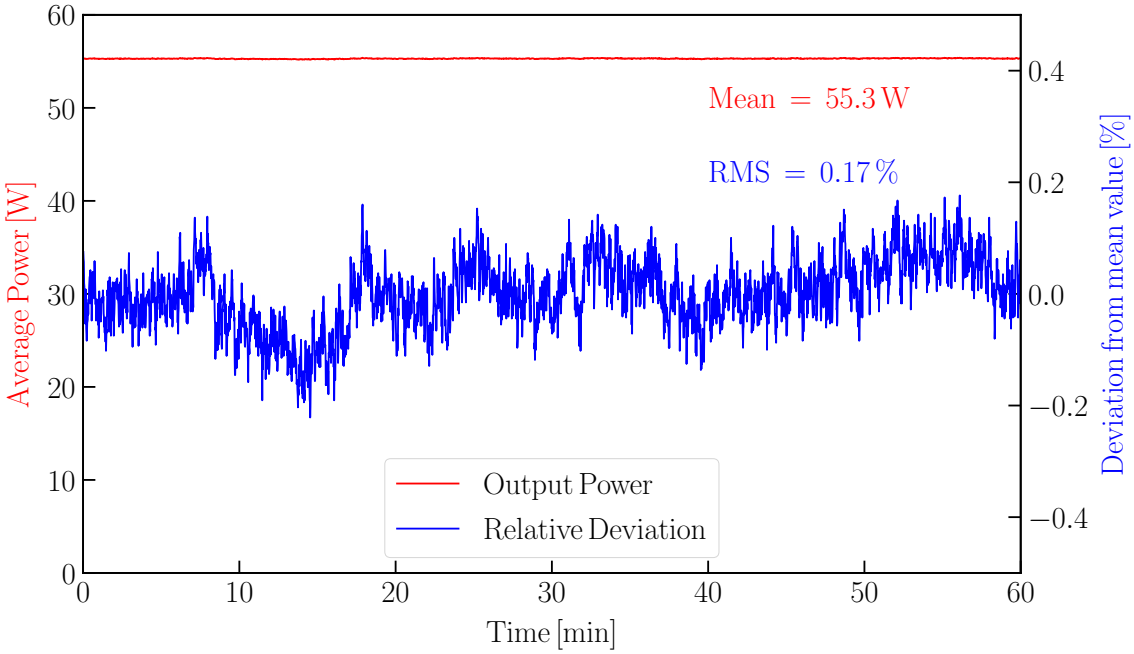

Figure 4.10 Average power fluctuations and relative deviation from mean value for thin plates setup over a time frame of 1 h. The data are taken after one hour of operation.

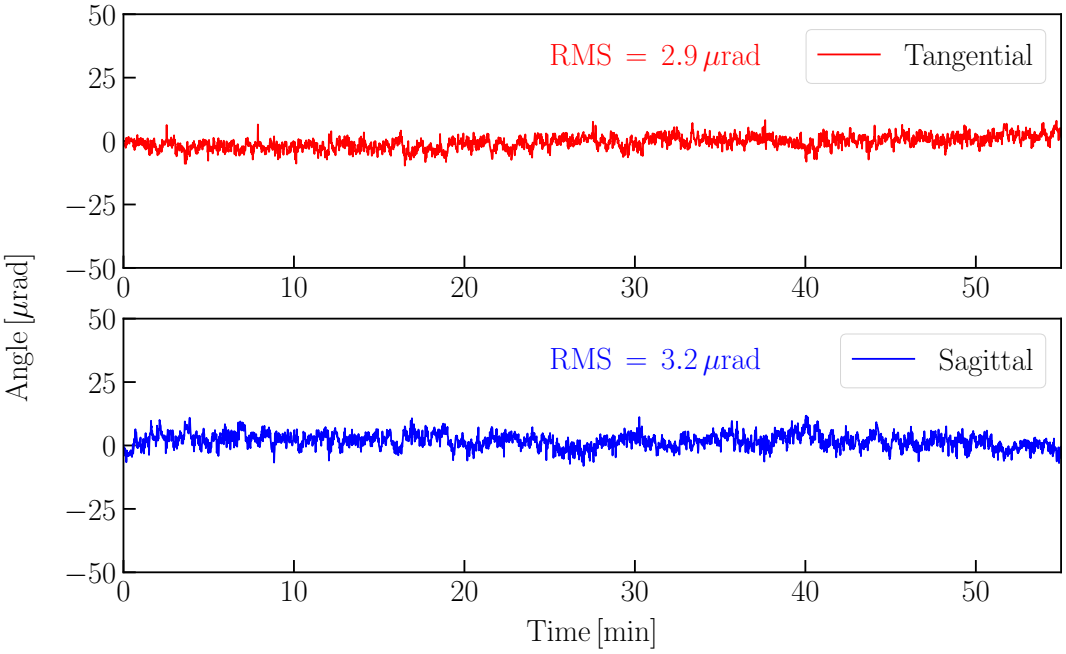

Figure 4.11 Sagittal and tangential angular beam pointing fluctuations for thin plates setup measured over a time frame of 1 h. The beam is recorded each second at the focus of a lens with 300 mm focal length.

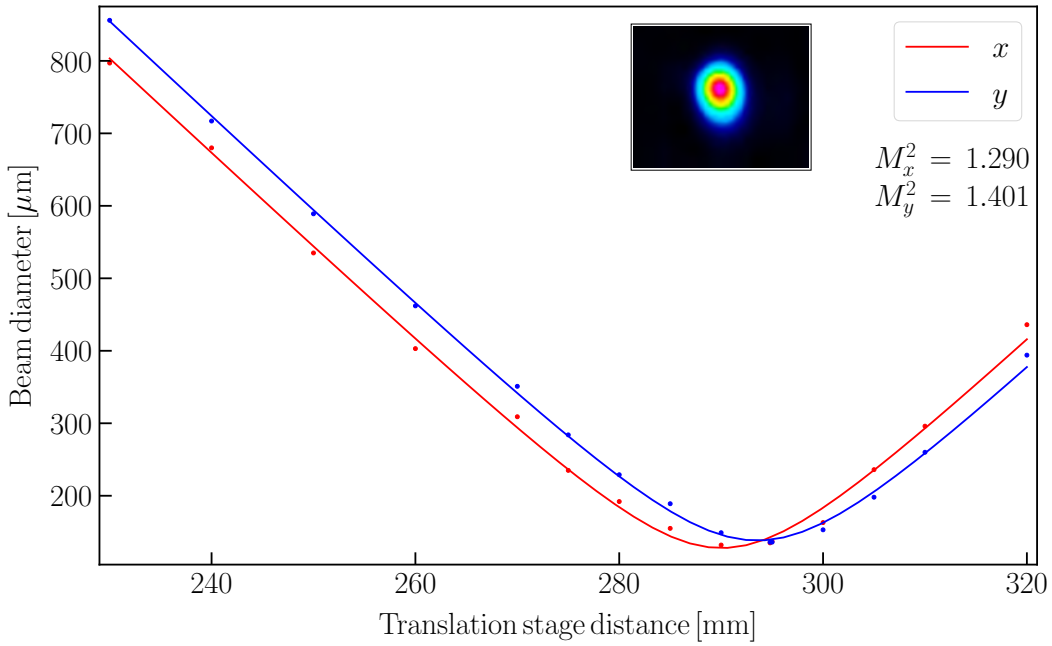

Figure 4.12 M^2 measurement for the thin plates setup. As reported in the graph, the values are 1.290 and 1.401, in x and y axis respectively.

4.2.3 Comparison with simulations

For the case of spatial effects, it is not possible to analytically predict the exact evolution of the beam at powers close to the critical power [71]. The spatio-temporal Gaussian characteristics of the beam are altered during propagation in the material and only numerical calculations can determine the final characteristics [81].

The simulations based on the split-step Fourier method described in section 3.1.1.1 may also be used for pulse propagation involving additional effects. An analogue of the split-step Fourier method can been used for simulating linear and nonlinear propagation of single-frequency spatial beams. For spatial problems, the algorithm is often termed *beam propagation method* [72]. Several libraries and software can be found, as for example *beampy* [105, 106]. The applicability of the split-step method to both temporal and spatial problems arises from the duality in the equations describing spatial and temporal propagation. Therefore, the split-step method may be employed for analysis of problems with propagation in space and time simultaneously, such as the nonlinear envelope equation [72]. Nevertheless, a more formal approach would require a full three-dimensional simulation of the wavefront propagation and, for shorter pulses, a full field approach where the SVEA is not applied.

For the experiment outlined in the previous section, the same simulation algorithm are used for the MPCs setup is employed, since the broadening mechanism for this type of waveguide is mainly SPM. The caustic of the input beam along the plates is modeled with the *ReZonator2* software [67], cf. Fig. 4.6b. This output is implemented in the *PyNLO*-based algorithm, and the broadening in each plate is simulated. The contribution of air between the plates is also taken into account. The comparison between simulations and measured data is shown in Fig. 4.13. From the comparison between measured data and simulations in the third and the forth plate, it is evident that the simulation has reached the limit of few cycle pulses, where the SVEA is no longer valid. Therefore, the agreement between simulations and data is lower. Additionally, the temporal profiles show that third order dispersion effects from the media are underestimated. The temporal profile at the exit of each plate for the simulations is not as distorted as for the experimental data. Nevertheless, the overall agreement with the data is remarkable since important simplification, as SVEA and treatment of spatial effect as temporal effects, are needed to make the algorithm applicable to this case.

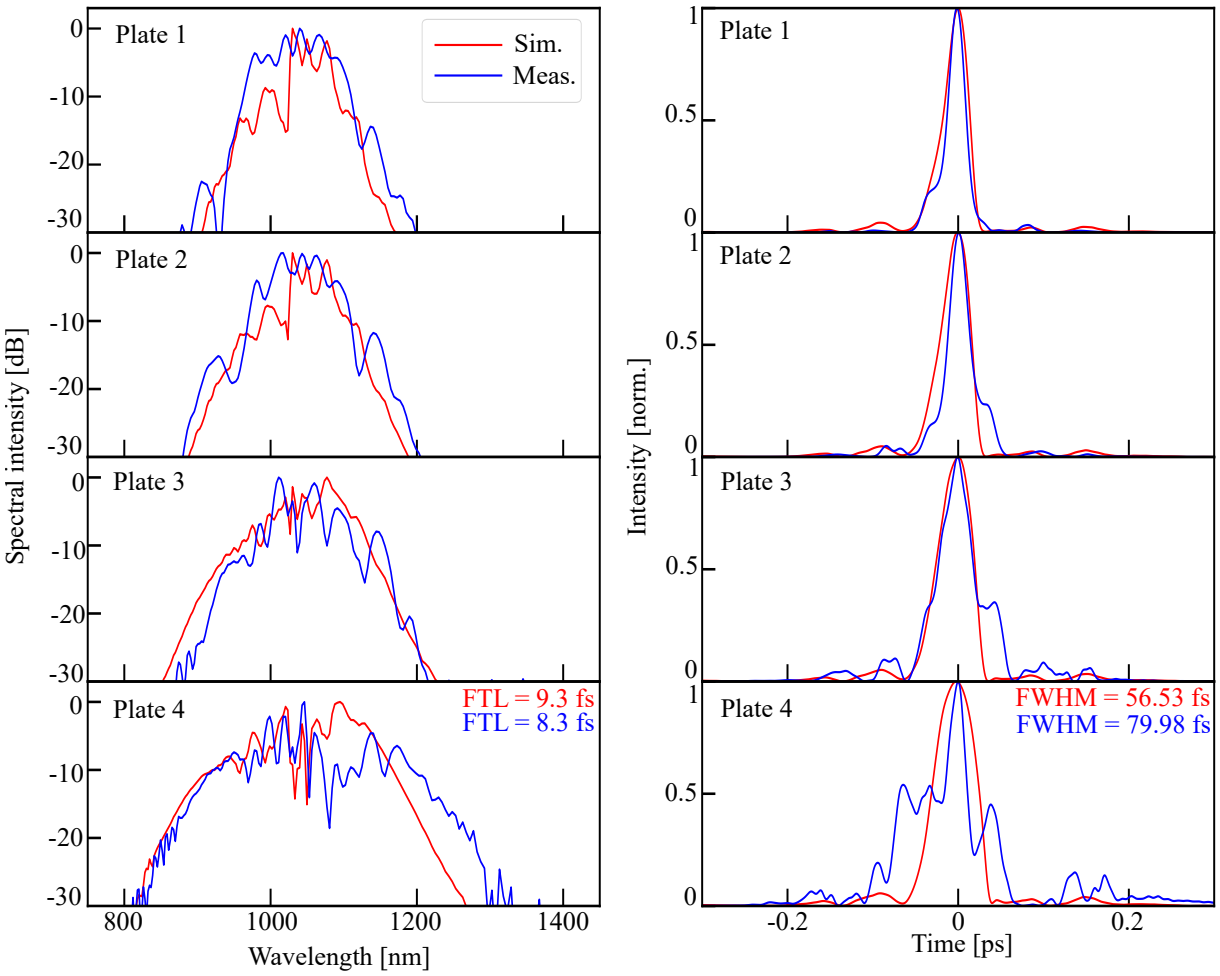

Figure 4.13 Comparison between simulated (red) and measured (blue) data for each plate. For each plate the spectra and the temporal profiles are shown. For the simulations results: the caustic is obtained with *ReZonator2* software [67], the output spectrum and temporal profiles are obtained with *PyNLO*-base code. The pulse duration and the FTL for the last plate are reported for comparison.

4.3 Conclusion

In this chapter, two different techniques to extend the spectral bandwidth of the frontend have been presented. The first technique, based on a single-ring PCF proved to be capable to deliver sub-5 fs FTL pulses with high efficiency and good beam quality. Nevertheless, this broadening technique is not yet reliable for day-to-day operation due to the sensitivity to alignment and frequent damages. The second technique, based on a thin-plates quasi-waveguide proved to be capable to deliver sub-10 fs pulses with a good beam quality and remarkable stability.

Both techniques proved to be invaluable and innovative tools to efficiently extend the bandwidth of the Yb:YAG-based fronted. Nevertheless, the fiber-based compression scheme proved to be a promising way for reaching the few- or even single-cycle regime,

further improvements of the fiber parameters are necessary for the long-term stability of the setup [84, 87]. For the future applications of the system, in particular for spectroscopy, the stability and day-to-day reproducibility of the frontend are key features. For these reasons, a system less prone to damage and to fluctuations, with lower complexity and more compact, as the thin-plates scheme presented above is preferred.

5 Terahertz and Mid-infrared generation

Broadband, intense sources of mid-infrared (MIR) and THz radiation are, nowadays, of great interest for applications in various fields, as bio-molecular analysis, material processing and absorption spectroscopy [3, 107].

In the last decade, thanks to the availability of high power solid state lasers, the generation of MIR pulses via intra-pulse difference-frequency generation (IP-DFG) gained more attractiveness. High power from the frontend translates into high power in the generated radiation. This mitigates the intrinsically low efficiency of the IP-DFG process. Moreover, the possibility to extend the limited bandwidth of the laser gain medium, as in the case of Yb-doped materials, made possible the generation of ultra-broadband MIR pulses, which is especially interesting for spectroscopic applications [3, 108].

Similarly, sources of broadband THz pulses operating at high average power and high repetition rates are seeing increasing interest as they benefit various applications, as non-destructive time-resolved molecular spectroscopy and imaging, THz communication and remote sensing [109].

For the different compression stages described in the previous chapter, only third-order nonlinear effects were described and exploited for experimental applications. To generate new frequencies in the MIR and THz spectral regions from near-infrared pulses, second-order nonlinear effects such as IP-DFG and optical rectification (OR) are required.

In this chapter, an overview of the second-order nonlinear processes is presented. The focus of this section is on IP-DFG, OR, and phase matching. A more detailed mathematical description of these phenomena can be found in [71, 72, 110]. Following this overview, the experimental work is presented. Firstly, OR in gallium phosphide (GaP)

crystals of the near-infrared pulses from the sub-20 fs frontend (section 3.2.1) is described. Secondly, the generation of MIR radiation in lithium iodate ($LiIO_3$) crystals via IP-DFG is described.

5.1 Second order nonlinear processes

For second order-nonlinear processes, the equation of nonlinear polarization, Eq. 3.6b, reduces to

$$\mathbf{P} = \mathbf{P}^{(2)} = \epsilon_0 \chi^{(2)} \mathbf{E}^2 = 2\epsilon_0 d_{\text{eff}} \mathbf{E}^2 \tag{5.1}$$

where d_{eff} is the effective nonlinear optical coefficient. This coefficient is related to the specific optical properties of the nonlinear medium and depends, for a certain input polarization geometry, on the non-vanishing components of the tensor $\chi^{(2)}$ [110]. Here, as in the previous chapters, the vectors $\mathbf{P}$ and $\mathbf{E}$ depend on the spatial component z and on the time component t.

To describe the field evolution in the case of second-order nonlinearities, it is convenient to write $\mathbf{E}$ as a superposition of three monochromatic waves at distinct frequencies, ω_1, ω_2 and ω_3, co-propagating along the direction z in a non-centrosymmetric medium

$$\mathbf{E} = \frac{1}{2}\left[A_1(z)e^{i(\omega_1 t - k_1 z)} + A_2(z)e^{i(\omega_2 t - k_2 z)} + A_3(z)e^{i(\omega_3 t - k_3 z)}\right] + \text{c.c.} \tag{5.2}$$

Using this equation in combination with Eq. 5.1, the explicit spectral contributions for the second order polarization response can be found. Each contribution contains different interacting frequencies: the components at $2\omega_1$, $2\omega_2$ and $2\omega_3$ describe the second-harmonic generation (SHG) process; the components at $\omega_1 + \omega_2$, $\omega_2 + \omega_3$ and $\omega_3 + \omega_1$ describe the sum-frequency generation (SFG) process; the components at $\omega_2 - \omega_1$, $\omega_3 - \omega_2$ and $\omega_3 - \omega_1$ describe the difference-frequency generation (DFG) process [71].

To describe each of these processes in detail, the simplified wave equation, Eq. 3.5, can be recalled. The term $\partial^2\mathbf{P}/\partial t^2$ of Eq. 3.5, in the case of second-order nonlinear processes, can be written as

$$\frac{\partial^2 \mathbf{P}}{\partial t^2} = -\epsilon_0 d_{\text{eff}}\, \omega_1^2 A_2^*(z) \cdot A_3(z) \cdot e^{i[\omega_1 t - (k_3 - k_2)z]} \tag{5.3a}$$

$$-\epsilon_0 d_{\text{eff}}\, \omega_2^2 A_1^*(z) \cdot A_3(z) \cdot e^{i[\omega_2 t - (k_3 - k_1)z]} \tag{5.3b}$$

$$-\epsilon_0 d_{\text{eff}}\, \omega_3^2 A_1(z) \cdot A_2(z) \cdot e^{i[\omega_3 t - (k_1 + k_2)z]} + \text{c.c.}\,. \tag{5.3c}$$

Using this expression in the wave equation, it is possible to derive the coupled wave equations, in the SVEA regime:

$$\frac{\partial A_1}{\partial z} = -i\sigma_1 A_2^* A_3 \cdot e^{-i\Delta k z} \tag{5.4a}$$

$$\frac{\partial A_2}{\partial z} = -i\sigma_2 A_1^* A_3 \cdot e^{-i\Delta k z} \tag{5.4b}$$

$$\frac{\partial A_3}{\partial z} = -i\sigma_3 A_1 A_2 \cdot e^{i\Delta k z} \tag{5.4c}$$

where $\sigma_j = d_{\text{eff}}\omega_j / c n_j$, $n_j = \sqrt{\epsilon_{rj}}$ is the refractive index and $\Delta k = k_3 - k_2 - k_1$ is the wave vector mismatch. Δk determines the energy flow among the beams. The first two equations are formally identical, thus ω_1 and ω_2 fields have the same role in the respective interactions and can be exchanged [110].

With the initial boundary condition $A_i(0) = 0$ $(i = 1, 2, 3)$, in Eq. 5.4, it is possible to describe different processes. $A_3(0) = 0$ describes a process in which two fields, $A_1(0)$ at ω_1 and $A_2(0)$ at ω_2, interact and generate a new field $A_3(0)$ at $\omega_3 = \omega_1 + \omega_2$. This process is called SFG. In the special case when $\omega_1 = \omega_2$, the process is called SHG. $A_2(0) = 0$ describes a process in which the fields $A_3(0)$ at ω_3 and $A_1(0)$ at ω_1 interact and generate a new field A_2 at $\omega_2 = \omega_3 - \omega_1$. This process is called DFG. The DFG usually involves two input fields with comparable intensities. When instead the process involves an intense pump field at ω_3 transferring energy to a weaker seed field at ω_1, therefore amplifying it and generating a new idler beam at frequency ω_2, it is called optical parametric amplification (OPA). In the special case in which $\omega_3 \approx \omega_1$, the OR process occurs. This process is commonly used to generate THz radiation [71, 72, 110].

5.1.1 Generation of mid-infrared radiation

Many experiments in time-resolved spectroscopy and high-field physics require femtosecond pulses with broadly tunable frequency. For example, in high-harmonic generation processes, driving pulses with longer wavelength are beneficial to extend the cutoff energy. Moreover, in MIR absorption spectroscopy, pulses for molecular excitation with few-cycle and phase-stable waveforms are a key point to enhance the sensitivity and the dynamic range [3, 8]. Second order nonlinear optical process, as IP-DFG, DFG and OPA, are suitable and widely-used techniques to extend laser bandwidths towards the MIR spectral region.

DFG is the second-order nonlinear process in which a pulse at frequency $\omega_2 = \omega_3 - \omega_1$ is generated by the interaction of two pulses at frequency ω_1 and ω_3 with com-

parable intensities in a nonlinear medium. Since ultra-short pulses are characterized by a broad spectrum, DFG could also occur between frequencies contained within the spectrum of a single pulse. This process is called IP-DFG. The IP-DFG of broadband pulses has been widely used for producing CEP-stable pulses due to its passive stabilization mechanism.

From the coupled wave equations, Eq. 5.4, it is possible to derive the generalised phase of the pulses involved in a generic DFG process as

$$\varphi_{\mathrm{DFG}} = \varphi_2 = \varphi_3 - \varphi_1 \tag{5.5}$$

If both the interacting frequencies are relatively fixed, up to a constant a both have the same CEP φ. Thus, for the case of IP-DFG the interacting frequency are from the same pulse and the phase is constant pulse to pulse. Therefore, the pulses generated by IP-DFG are passively CEP-stabilized [110]. Although, IP-DFG is a simple nonlinear optical approach to generate CEP-stable pulses in the MIR spectral region, it has a rather limited efficiency that is inherently associated with phase matching [108].

To understand the phase matching condition it is necessary to define the intensity of the wave generated in a second-order nonlinear process. From the wave equation for DFG, Eq. 5.4c, is possible to calculate the amplitude A_2 of the generated wave after a propagation distance L into a nonlinear crystal, as

$$A_2(L) = \frac{2id_{\mathrm{eff}}\omega_2^2}{c_0^2 k_2} A_3 A_1^* \int_0^L e^{i\Delta k z} dz = \frac{2d_{\mathrm{eff}}\omega_2^2}{c_0^2 k_2} A_3 A_1^* \left[\frac{e^{i\Delta k L} - 1}{\Delta k}\right] . \tag{5.6}$$

The intensity of a wave at frequency ω_i is $I_i = 2\epsilon_0 c_0 n_i |A_i|^2$. Therefore, the intensity of the generated pulse in a crystal length L is

$$I_2 = \frac{8d_{\mathrm{eff}}^2 \omega_2^2 I_3 I_1}{n_1 n_2 n_3 \epsilon_0 c^2} L^2 \,\mathrm{sinc}^2\left(\frac{\Delta k L}{2}\right) . \tag{5.7}$$

This equation has a maximum at $\Delta k = 0$. This condition is known as *perfect phase matching*. When it is fulfilled, energy is mostly efficiently transferred from the incident waves to the generated wave [71].

The phase matching condition, in the case of collinear beams, as for IP-DFG can be also written as

$$n_2\omega_2 = n_3\omega_3 - n_1\omega_1 . \tag{5.8}$$

From this formulation, it is clear that perfect phase matching is often difficult to achieve.

Considering an isotropic medium with positive dispersion ($\partial n/\partial\omega > 0$), if $\omega_1 < \omega_2 < \omega_2$, the refractive indexes have a similar relation $n_1 < n_2 < n_3$. Therefore, to achieve perfect phase matching is required $n_3 - n_2 > 0$ and $n_1 - n_2 < 0$. Hence, Eq. 5.8 has no solution. In other words, perfect phase matching is not achievable in isotropic media with positive dispersion since different refractive indices for the two interacting waves are required. This can derived also for isotropic media with negative dispersion.

Birefringence phase-matching, among other techniques, is commonly employed to achieve perfect phase-matching [110]. In this approach, precise angular orientation of the crystal with respect to the propagation direction of the incident light is used to adjust the refractive index. For simplicity the following description is restricted to uniaxial crystals but can be easily extended to biaxial crystals, as described in [71]. Uniaxial crystals are described by one optical axis and two principal refractive indices. When the beam interacting via DFG process pass through a uniaxial crystal, it splits into an ordinary and an extraordinary ray. Light polarized perpendicular to the plane containing the propagation vector k and the optic axis is called the ordinary ray. This ray experiences the ordinary refractive index n_0. Light polarized along the plane containing the propagation vector k and the optic axis is called the extraordinary ray and experiences a refractive index $n_\mathrm{e}(\theta)$ that depends on the angle θ between the optic axis and k and its value varies between n_o and n_e. This dependency can be expressed according to

$$\frac{1}{n_\mathrm{e}(\theta)^2} = \frac{\sin^2\theta}{n_\mathrm{e}^2} + \frac{\cos^2\theta}{n_\mathrm{o}^2}\,. \tag{5.9}$$

For $\theta = \pi/2$, $n_\mathrm{e}(\theta) = n_\mathrm{e}$ and for $\theta = 0$, $n_\mathrm{e}(\theta) = n_\mathrm{o}$. Therefore, the phase matching condition is achieved by adjusting the angle θ to obtain the value of $n_\mathrm{e}(\theta)$ for which Δk is minimized [71, 110].

Uniaxial crystals are classified into positive crystals ($n_o > n_e$) and negative crystals ($n_o < n_e$). According to the polarization of three interacting fields, there are three interaction configurations in a uniaxial crystal. These configurations are

$$n_2^o w_2 + n_1^o w_1 = n_3^e(\theta) w_3 \quad \text{type-I, ooe interaction} \tag{5.10a}$$

$$n_2^o w_2 + n_1^e(\theta) w_1 = n_3^e(\theta) w_3 \quad \text{type-II, oee interaction} \tag{5.10b}$$

$$n_2^e(\theta) w_2 + n_1^o w_1 = n_2^e(\theta) w_2 \quad \text{type-II, eoe interaction}\,. \tag{5.10c}$$

In the cases mentioned above, all the wave-vectors of the interacting beams are assumed to have the same direction. This is called *collinear configuration* [110]. For a negative uniaxial crystal, as Lithium iodate ($LiIO_3$), the phase matching condition cannot be satisfied if ω_3 is ordinary. Similarly, for a positive uniaxial crystal, the phase matching

condition cannot be satisfied if ω_3 is extraordinary.

From the considerations above is intuitive to deduce that the choice of the nonlinear medium as well as the choice of the experimental configuration are crucial parameters for the success of experiments involving a second order nonlinear process. For example, IP-DFG is a powerful tool to generate CEP-stable MIR radiation via birefringent phase-matching and the inherently low efficiency can be mitigate employing powerful sources. In the recent years, the generation of MIR pulses via IP-DFG of laser sources in the near-infrared region gained more attractiveness due to the availability of high power sources. However, the damage threshold of the nonlinear medium is the main limitation of this approach.

Yb-doped lasers are able to deliver average powers of hundreds of watts and peak powers of tens of megawatts directly from the oscillators [59, 60, 111]. Additionally, the availability of efficient extra-cavity broadening of these sources made it possible to overcome the narrowband emission of the Yb-doped material. The generation of always broader pump spectra at high powers makes these sources perfect candidates for the generation of intense, broadband MIR radiation via IP-DFG.

In addition to the choice of a suitable source, it is necessary to chose a suitable material to generate MIR radiation in the desired region with high efficiency. Possibility to achieve phase matching, absorption region and damage threshold are only some of the criteria for the choice of the suitable material. Yb-doped fiber amplifiers have been employed by Kanda et al. to generate MIR radiation spanning from 6.7-17.8 µm via IP-DFG in a 14 µm thick GaSe crystal [112]. Moreover, Pupeza et al. used an Yb:YAG oscillator with extra-cavity broadening to generate MIR radiation spanning from 6 µm to 12 µm at around 100 mW of average power via IP-DFG in a 1 mm thick $LiGaS_2$ crystal [3].

5.1.2 Generation and detection of THz radiation

Optical rectification and linear electro-optic effect (or Pockels' effect) from femtosecond laser pulses are widely-used second-order nonlinear optical techniques for the generation and detection of freely propagating sub-picosecond radiation with THz frequencies.

Research about OR in non-centrosymmetric crystals for the generation THz radiation started as early as in the 1970s [113, 114]. Later, in 1984, the generation of nearly single-cycle THz pulses by OR was first demonstrated [115].

As mentioned previously, OR is a second-order nonlinear optical process, which is a special case of DFG [71]. If two frequencies, ω and $\omega + \Omega$, from the same optical pulse are mixed by IP-DFG, a new spectral component at frequency Ω in the THz range is generated. The nonlinear polarization response induced by the pump pulses can be expressed by

$$\mathbf{P}_{\mathrm{NL}}(\Omega) = 2 \int_0^\infty d_{\mathrm{eff}} \mathbf{E}(\omega + \Omega) \mathbf{E}^*(\omega) d\omega \,. \tag{5.11}$$

Typically, the durations of the pump pulses used for OR range from below 30 fs to above 1.5 ps [13, 116]. Thus, the generated difference-frequency spectral components lie in the THz spectral range. From the previous equation can be seen that a narrowband pump pulse generates low THz frequencies, generally below 0.5 THz and a broadband pulse can generate a broad THz spectrum containing also higher THz frequencies, up to tens of THz [116]. As for the IP-DFG, the emitted THz radiation is CEP stable.

The generation of THz radiation via OR is mainly influenced by the dispersion of the medium. As for the DFG process, the energy is efficiently transferred from the pump pulses to the THz pulses via OR when the phase matching condition $\Delta \mathrm{k} = 0$ is fulfilled. In this case Δk is

$$\Delta k = k(\Omega) + k(\omega) - k(\omega + \Omega) \approx k(\Omega) - \left. \frac{\partial k}{\partial \omega} \right|_{\omega_0} \cdot \Omega \,. \tag{5.12}$$

The approximation in the third term of the equation is valid if $\Omega \ll \omega$, which is generally the case for THz generation by OR. In the case of collinear phase matching, recalling the identity $k = n\omega/c$, Eq. 5.12 can be written as

$$\Delta k = \left[n(\Omega) - n_{\mathrm{g}}(\omega_0) \right] \cdot \Omega / c \,, \tag{5.13}$$

here ω_0 is the pump central frequency, c is the speed of light in vacuum, and n and n_g are the refractive and group indices, respectively. Therefore, the phase-matching condition is satisfied when the phase velocity $v = c/n$ of the generated THz radiation equals the group velocity $v_g = c/n_g$ of the optical pump pulse along the propagation in the nonlinear medium. This can be expressed by the *velocity-matching condition* $v(\Omega) = v_{\mathrm{g}}(\omega_0)$ [116, 117].

Different classes of materials are suitable for generation of THz radiation via OR. Some examples are: semiconductors such as CdTe, GaAs, GaP, GaSe, or ZnTe; ferroelectric materials such as lithium niobate ($LiNbO_3$), or lithium tantalate ($LiTaO_3$); organic materials such as DAST, DSTMS and HMQ-TMS [118]. The selection of the suitable material for the experimental application is influenced by the velocity-matching condition but also by other crucial factors as the absorption range, the availability, and

the optical damage threshold. Thus, in the final analysis the choice of material is strongly related to the laser source driving the conversion.

In the recent years, growing interest has been shown in intense, broadband, and coherent light sources in the spectral region between 0.1 THz and 30 THz operating at high average power and high repetition rates [13]. Applications are, for example, time-domain THz spectroscopy and time-domain THz imaging. These techniques can access a great variety of research and technology fields as bio-molecular analysis, nondestructive testing, medical diagnosis and rapid screening in drug development [116, 117]. The availability of such sources relies on the choice of the medium used for the generation of the THz radiation as well as on the laser driving source for the generation of the pump pulses.

Two main classes of media to generate THz radiation can be distinguished: gaseous media and solid media. In gaseous media, the generated THz-radiation does not suffer from limited damage threshold or narrowband velocity-matching as in solids. In the last two decades, the growing availability of intense and broadband sources based on chirped-pulse amplification in Ti:sapphire gain media [119], greatly accelerated the progresses in the generation and the detection of broadband THz pulses in ionized gases [120–122]. However, the kHz repetition rate of these amplified sources limits the signal-to-noise ratio and increases the acquisition time for detection. Alternatively, as explained above, THz radiation can be generated in solid media via OR. Without suitable sources, this approach would suffers from the low damage threshold and the necessity of velocity-matching from the solid nonlinear medium. However, this approach greatly benefits from the availability of driving pulses with lower peak intensities, in the order of tens of $\mathrm{GW\,cm^{-2}}$. Diode-pumped Yb-doped oscillators, with their higher average and peak power [8], are promising sources for the generation of THz radiation via OR.

Nowadays, laser systems based on Yb-doped gain media deliver pulses with tens of micro-joules of energy and hundreds of watts of average power [111, 123], reaching up to 25 MW peak power at 16.3 MHz repetition rate without necessity of an amplification stage [62].

Due to velocity-matching at 1 µm wavelength and high damage threshold for high average power irradiance, a suitable choice of optical material for the generation of THz radiation from Yb-doped laser sources is gallium phosphide (GaP) [124, 125]. GaP is a III-V semiconductor with zincblend structure that has been extensively used as THz emitter in the region between 0.2 THz and 7 THz [117]. Yb-doped fiber amplifiers have been used to generate THz pulses via OR in GaP crystals with a cutoff frequency up to 3.5 THz at 6.5 µW average power [126–129]. However, in order to increase the bandwidth

and the average power of the generated THz pulses, pump pulses with higher peak power are desired. This translates in the research of driving systems with shorter pulses at higher average power, for repetition rates on the order of MHz. In 2018, Paradis et al. extended the bandwidth of the generated pulses to 5 THz by using 50 fs, 4 W pulses at 61 MHz repetition rate from an Yb-doped thin-disk oscillator [130]. Following this research, in 2019, Drs et al. extended the amplitude of the THz spectrum to 5 THz at 0.3 mW average power by using 95 fs-long pulsees from a similar source [131].

Additionally, the same crystal has been employed for broadband detection of THz pulses via electro-optic sampling (EOS). In 1997 Wu et al. firstly demonstrated EOS of THz pulses with a GaP crystal [132]. Broadband THz electro-optic sampling with GaP crystals was further developed by Leitenstorfer et al. [133].

The detection of freely propagating THz pulses is commonly performed by EOS [134]. This field-resolved detection technique measures the polarization change of a fs near-infrared pulses propagating through an electro-optic crystal simultaneously with the THz radiation. The THz electric field induces a phase modulation of the laser pulses through the linear electro-optic effect.

The linear electro-optic effect is described by the term $\mathbf{P}^{(2)} = \chi^{(2)}\mathbf{E}^2$ similarly to OR. To understand the correspondence between these two effects, it is necessary to describe the polarization response $\mathbf{P}$ and the electric field $\mathbf{E}$ by vectors, and the susceptibility χ by a third-rank tensor. The i-th component of the second-order nonlinear polarization response for the case of two laser beams with frequencies ω_2 and ω_1 impinging on a crystal, $\mathbf{P}_i^{\omega_1-\omega_2}$, is related to the components j and k of the electrical fields, $E_j^{\omega_1}$ and $E_k^{\omega_2}$, by

$$\mathbf{P}_i^{\omega_1-\omega_2} = \chi_{ijk}^{\omega_1-\omega_2} E_j^{\omega_1} E_k^{\omega_2} \,. \tag{5.14}$$

OR and the linear electro-optic effect resulting from the previous equation considering, respectively, the limits

$$\omega_2 \to \omega_1 \quad \mathbf{P}_i^0 = \chi_{ijk}^0 E_j^{\omega_1} E_k^{\omega_1} \tag{5.15a}$$

$$\omega_2 \to 0 \quad \mathbf{P}_i^{\omega_1} = \chi_{ijk}^{\omega_1} E_j^{\omega_1} E_k^0 \tag{5.15b}$$

where a strong electric field at frequency ω_1 induces a direct-current polarization $\mathbf{P}_i^0$ and a direct-current electric field E_k^0 induces a polarization response $\mathbf{P}_i^{\omega_1}$ at frequency ω_1. Further calculations can show that the susceptibility is identical in both effects under interchange of indices and frequencies, $\chi_{ijk}^0 = \chi_{jik}^{\omega_1}$ [117].

5.2 Experimental setup

In what follows, OR in gallium phosphide (GaP) crystals of the near-infrared pulses from the sub-20 fs frontend (section 3.2.1) and the generation of MIR radiation in lithium iodate ($LiIO_3$) crystals via IP-DFG is described.

5.2.1 THz generation in gallium phosphide crystals

The first generation of MPC-based nonlinear compression, section 3.2.1, has been used to generate THz radiation via OR in GaP crystals [13]. The schematic of the system is depicted in Fig. 5.1.

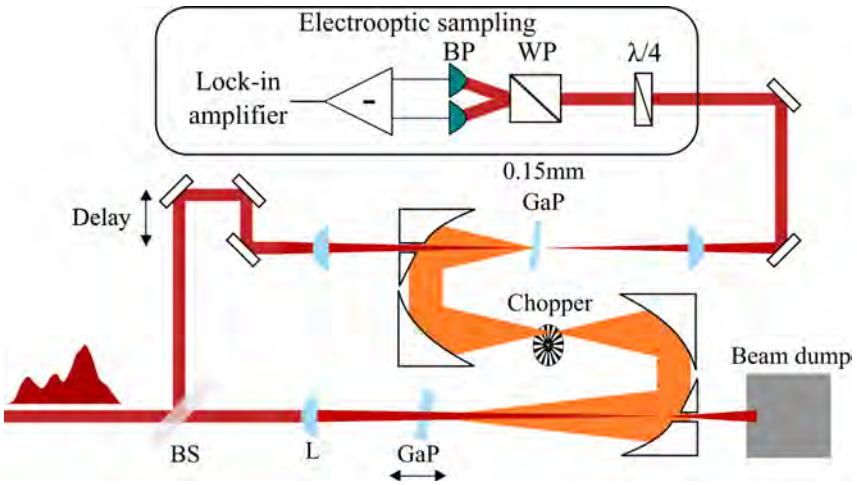

Figure 5.1 Schematic layout of the setup for the generation and the detection of THz pulses. The THz radiation is generated in GaP via OR of the near-infrared pulses from the first generation of multipass cells-based broadening scheme. The pulses incident on the GaP crystal are focused by a 250 mm-focal length lens (L). Different thicknesses crystals are placed before the focus. The generated THz radiation is separated from the pump radiation by an off-axis bare-gold coated, pierced, parabolic mirror. Less than 1 % of the incident pump power is separated by a calcium-fluoride wedge (BS) and is used as probe for EOS detection. A similar parabolic mirror is used to focus the THz radiation and combine it with the probe pulses onto a 0.15 mm-thick GaP crystal for EOS detection. Wollaston prism (WP), quarter waveplate ($\lambda/4$), balanced pthotdiodes (BP).

The first generation of MPCs described, delivered 18 fs pulses with a total energy of 3.8 µJ at 16 MHz repetition rate. The output pulses are used as pump pulses for the generation of THz radiation. The THz pulses are generated via OR of the pump pulses in uncoated, <110>-cut GaP crystals. In the crystals, the group velocity of the pump pulses is equal to the phase velocity of the emitted THz waves n_g(NIR)= n(THz) [135]. Therefore, velocity-matching is achieved.

The near-infrared pulses are focused using a convex lens with 250 mm focal length. Each GaP crystal is placed before the lens focus at a beam diameter of 700 µm ($1/e^2$), corresponding to 97 GW/cm^2 peak intensity and a fluence of 2 mJ/cm^2 at an average power of 60.5 W.

The generated THz beam is collimated by an off-axis bare-gold coated, pierced, parabolic mirror with a focal length of 101.6 mm. The near-infrared beam, instead, is transmitted through the hole in the center of the parabolic mirror. The reflected THz radiation is filtered from the remaining near-infrared radiation by a Teflon filter. Afterwards, it is directed towards an EOS setup for field-resolved detection.

Approximately 500 mW of the fundamental beam before the THz generation stage is separated by a calcium fluoride (CaF_2) plate and used as probe for the EOS. The 18 fs pulses have a temporal duration short enough to offer sufficient temporal resolution for field-resolved detection of the THz pulses. A second off-axis bare-gold coated, pierced, parabolic mirror with a focal length of 50.8 mm is used to recombine the probe and the THz beams. This parabolic mirror is also used to focus the THz beam into the EOS nonlinear crystal.

The two beams are overlapped and focused onto an uncoated 0.15 mm-thick, <110>-cut GaP crystal. Their relative delay is controlled by a motorized linear stage (Physik Instrumente Q-545). The linear electro-optic effect is used for detection. The refractive index of the 0.15 mm-thick GaP is modified proportionally to the strength of the THz field. These changes can be resolved by detecting the changes in the polarization state of the probe beam. The polarization is evaluated at each step of the motorized stage by using an ellipsometer. The ellipsometer consists of a quarter-wave plate (Thorlabs AQWP10M-980), a Wollaston prism (Thorlabs WP10), and a balanced photo-diode detector (Thorlabs PDB210A). The THz pulses were mechanically chopped at the frequency of 1 kHz at a focus of THz beam. The focus is obtained implementing a second pair of bare-gold-coated parabolic mirrors prior to the EOS setup. A lock-in amplifier (Stanford Research Systems SR830) is used for the readout. The resulting field traces are shown in Fig. 5.2.

The normalized power spectra for the three different thicknesses of GaP are compared in Fig. 5.3. As shown, the cutoff frequency of the THz pulses for the 0.2 mm-thick GaP extends to 5.7 THz, at 10^{-4} dynamic range.

For the THz pulses, in addition to the electric field, the power is measured by a commercial Golay cell detector (Tydex GC-1P) at the position of the EOS crystal. Fig. 5.4 shows the measured average power for the generated pulses in 2 mm, 1 mm,

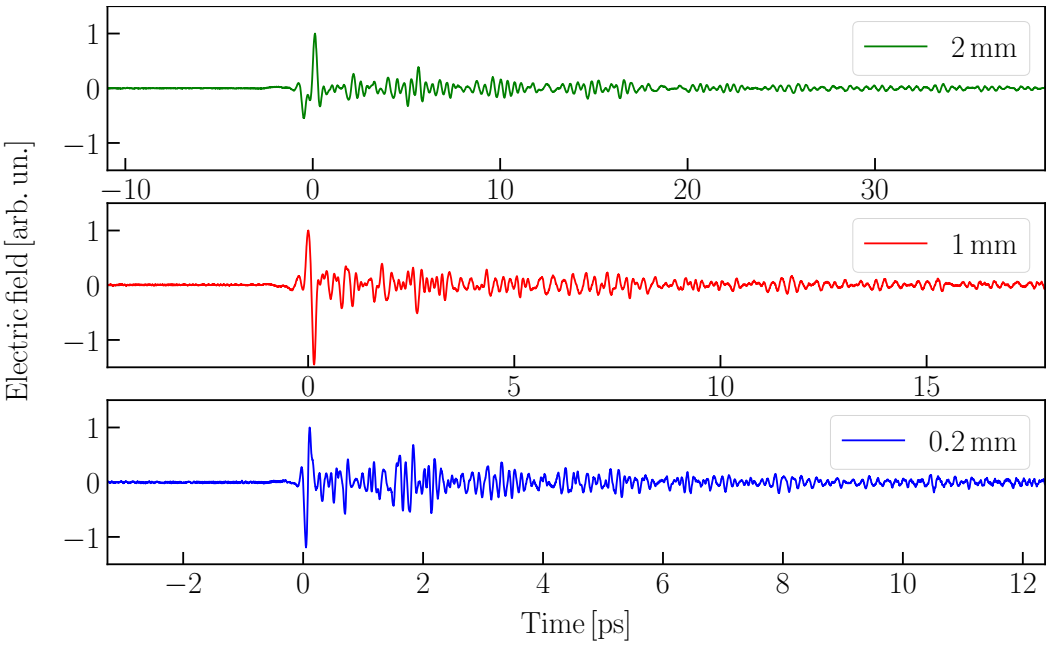

Figure 5.2 THz transient electric field generated in a 0.2 mm- (blue), 1 mm- (red) and 2 mm-thick (green) GaP crystal measured by an EOS setup containing a 0.15 mm-thick GaP crystal.

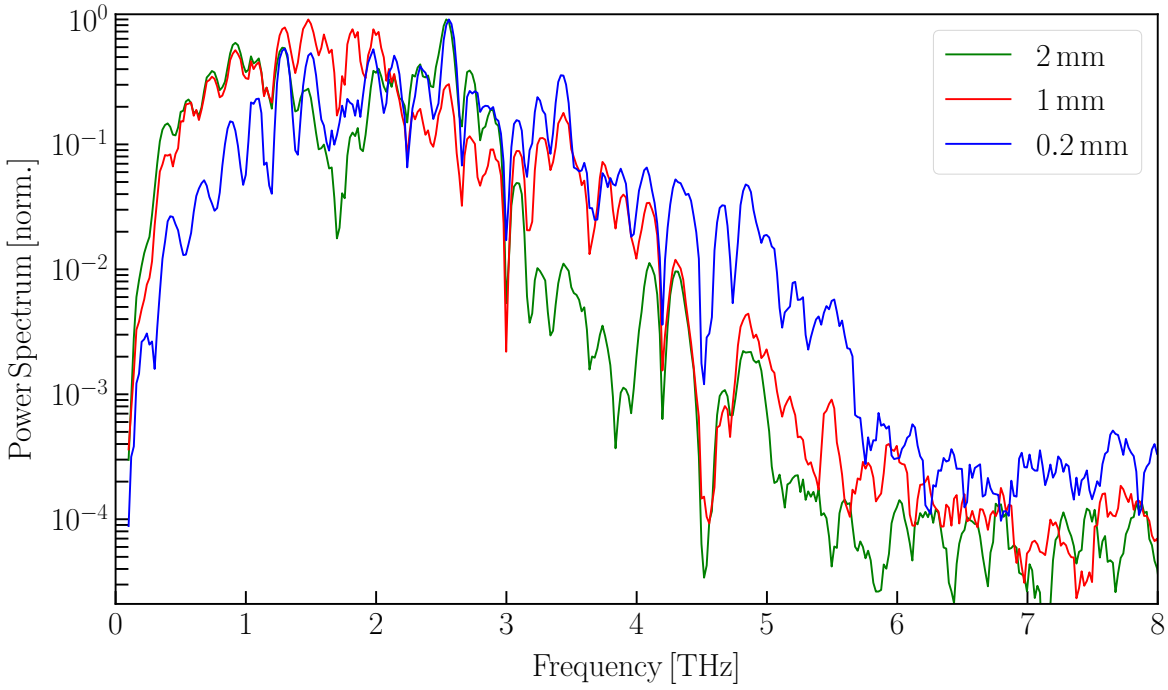

Figure 5.3 Power spectra of the generated THz pulses for different thicknesses of GaP. The corresponding EOS traces are recorded at 97 GW/cm^2 pump peak intensity.

and 0.2 mm-thick GaP crystal for different pump pulses intensities. In the calculation of the power, losses caused by the transmission of the Teflon filter and the reflections of the parabolic mirrors are taken into account. The data are interpolated with a second order polynomial curve. For the thinnest crystal, the power of the THz pulses tends to be exponentially proportional to the pump intensity. However, it is evident in the

interpolation for the 2-mm-thick GaP that, at higher conversion efficiencies and pump peak intensities beyond 70 GW cm^{-2}, the dispersion for the few-cycle pump pulses, and the temporal walk off between the generated THz pulses and the pump pulses become more prominent, resulting in a different behavior. Additionally, it is remarkable that at the maximum pump power, no extra cooling of the GaP crystal was required even after few hours of measurements. These curves shows the scalability of this process. Following the second-order dependency of the generated power from the pump intensity is reasonable to state that a high-power fronted could be beneficial in the generation of intense THz radiation.

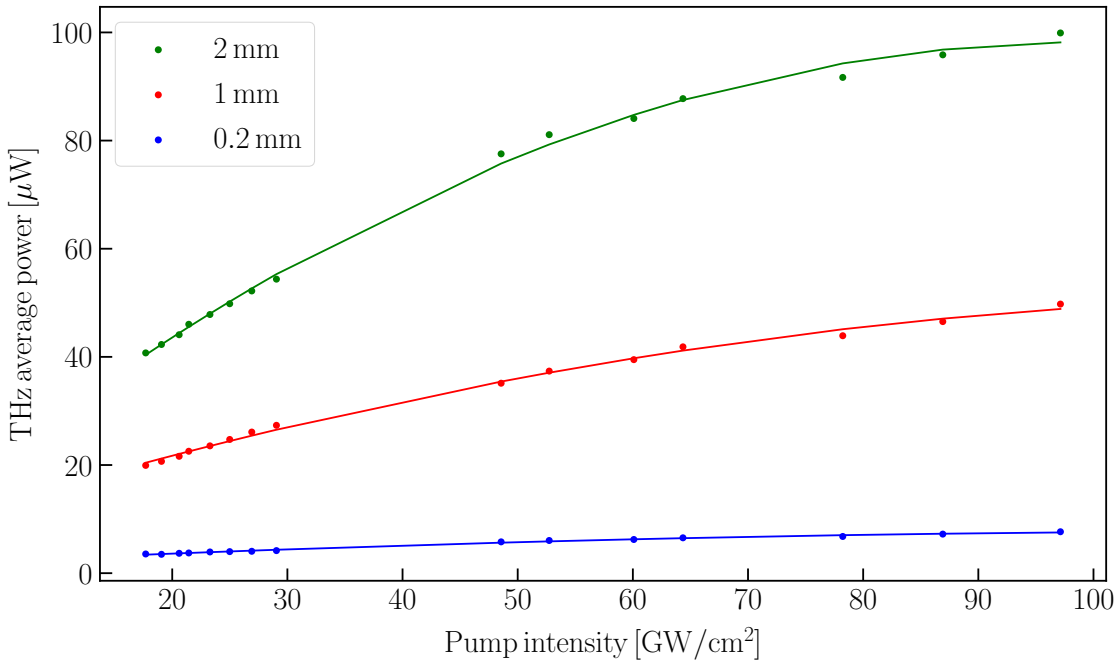

Figure 5.4 Measured power of the generated THz pulses versus the peak intensity of pump pulses for different thicknesses of GaP, obtained under ambient conditions. The points indicate the measurements and the lines are second order polynomial interpolation of the measured data.

In the laboratory environment, a relatively high air humidity ($\approx 46\,\%$) is present. Thus, absorption of the THz radiation by water vapor molecules [136] in air can be resolved. The Fourier transformed spectrum of the field shows several dips, which are in good agreement with the water absorption lines from the HITRAN database [129, 137], cf. Fig. 5.5. The 0.2 mm-thick GaP crystal delivers the broadest spectrum (blue) in these experiments. For each data set, a trace is acquired in 10 min-long EOS scan with 30 ms integration constant. The water vapor lines (red) are in agreement with the Fourier-transformed spectrum, with 10 GHz resolution up to 7 THz. The large amplitude of the free induction decay at the trailing edge of the electric field suggests high absorption of the generated THz pulses by water molecules. Therefore, operating the system in evacuated atmosphere will lead to higher output power of the generated THz radiation.

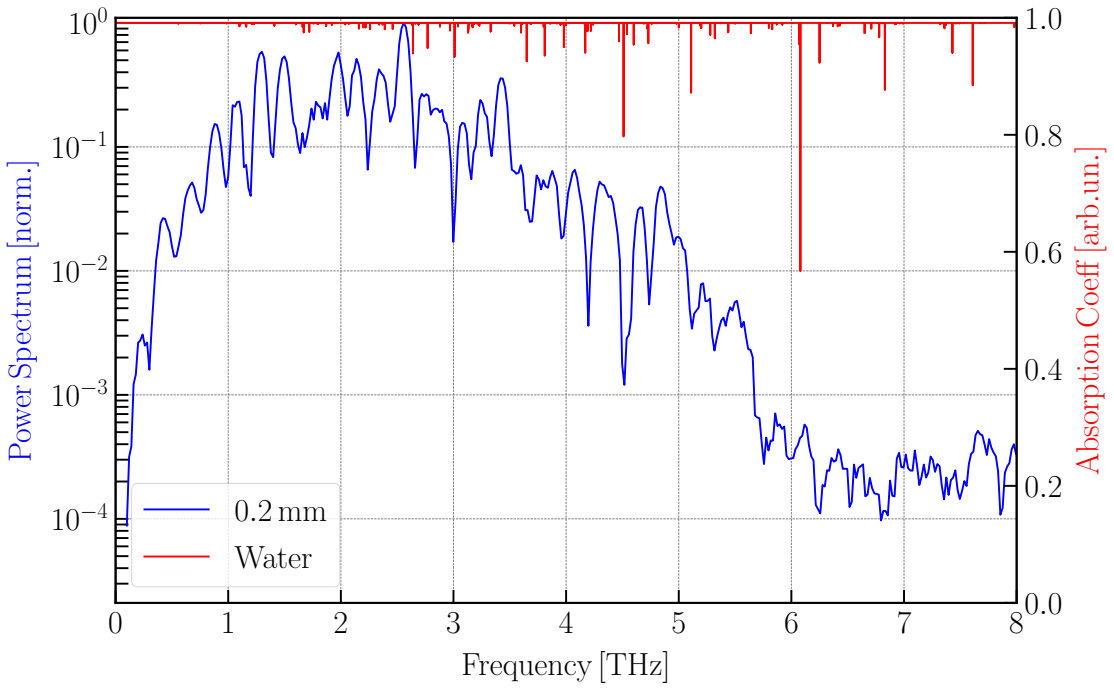

Figure 5.5 Fourier transformed spectrum from the electric field generated in a 0.2 mm-thick GaP crystal measured by electro-optic sampling containing a 0.15 mm-thick GaP crystal. The relative humidity in the laboratory at the time of the experiment was 46 %. In red the water absorption lines obtained from HITRAN database are shown.

5.2.2 Mid-infrared generation in lithium iodate crystals

Lithium iodate ($LiIO_3$) is a negative uniaxial crystal, commonly used for harmonics generation of driving pulses in the near-infrared spectral region. Despite its low effective nonlinearity of approximately d_{31} =4.4 pm V^{-1}, $LiIO_3$ has a wide transparency range (0.28-6 µm) [103]. The favorable phase matching and the wide transparency range made this material also suitable for low-wavelength MIR generation from 1 µm driving lasers via IP-DFG. The calculated phase matching factor, $\mathrm{sinc}^2\left(\frac{\Delta kL}{2}\right)$ from Eq. 5.7 [71], for three different thicknesses, 2 mm, 1 mm, 0.3 mm assuming pump pulses at 850 nm wavelength are shown in Fig. 5.6. This figure shows the possibility to generate MIR radiation, in thin crystals, spanning from 2.4 to 8 µm from pump pulses with pulse duration below 10 fs, as in the experiment outlined in this section. In the calculation, absorption effects are not taken into account, in Fig. 5.6 a gray shadow above 6 µm is indicating the region with strong absorption in $LiIO_3$ crystal.

The setup for MIR generation and detection is depicted in Fig. 5.7. The 8.5 fs pulses from the thin plates setups (section 4.2.2) are focused into $LiIO_3$ crystals of different thickness with a lens (f = 300 mm). The p-polarized input pulses evenly distribute along the extraordinary and the ordinary axes for type-I phase matching. The generated MIR

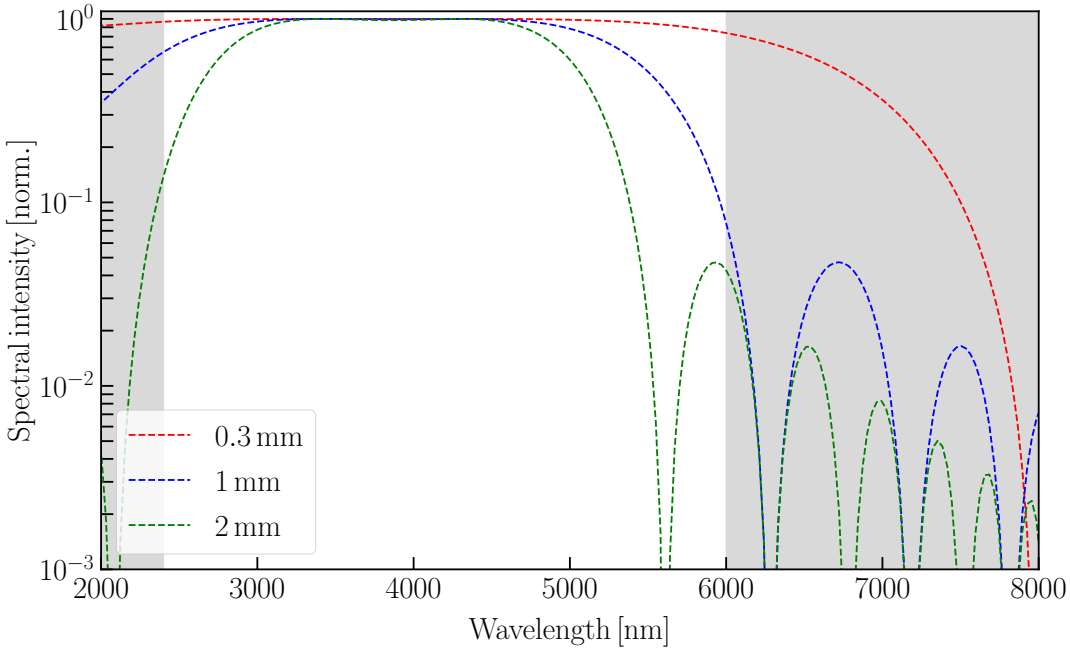

Figure 5.6 Calculated phase matching curves for IP-DFG in 0.3 mm (red), 1 mm (blue) and 2 mm (green) thick $LiIO_3$ crystals. The gray areas indicate: the region with stron absorption above 6000 nm [103] and wavelengths below 2400 nm that are not possible to phase match in the experiment outlined in this section.

radiation was separated by a tailored ZnSe beam splitter (UltraFast Innovations GmbH, F3-S161108) and then collimated by a gold-coated off-axis parabolic mirror with focal length of 101.6 mm. After collimation, different long-pass filters are used to remove the residual pump radiation transmitted by the beam splitter. After the long-pass filters the MIR radiation is sent to a power meter and a monochromator (Newport Cornerstone 260) for power and spectral measurement, respectively.

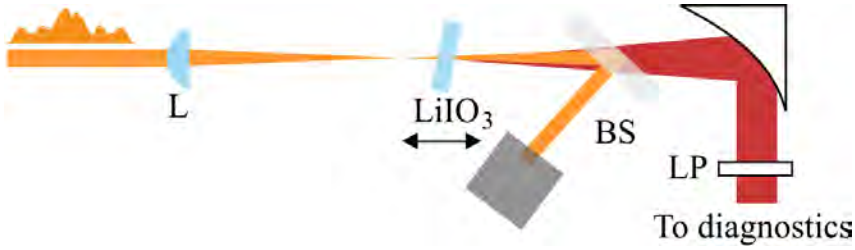

Figure 5.7 Schematic layout of the measurement setup. The MIR radiation is generated in $LiIO_3$ crystals via IP-DFG of the near-infrared pulses from the thin plates broadening scheme. The pulses incident on the crystal are focused by a 250 mm-focal length lens (L). Different thicknesses crystals are placed after the focus. The generated radiation is separated by the pump radiation by a beam splitter (BS) and re-collimated by a bare gold off-axis parabolic mirror to be sent to the diagnostics.

The crystals used for this experiment (EKSMA Optics, UAB) have different thicknesses: 2 mm (800-1300 nm protective coating), 1 mm (800-1300 nm protective coating) and 0.3 mm (700-1800 nm AR coating). Each crystal is placed after the focus of

the lens and moved towards the focus, to increase the peak intensity, till a damage occurs. This procedure establishes the damage threshold of the crystals and the maximum achievable average power for the MIR radiation. The highest average powers achieved with 2 mm, 1 mm and 0.3 mm $LiIO_3$ crystals, before damage, are 72 mW, 16 mW and 1.1 mW, respectively. The power is measured behind a 2.4 µm long-pass filter (LP2400-33-969, Edmund Optics Ltd.) at a peak intensity of approximately 250 GW cm^{-2}, for each crystal.

The choice of $LiIO_3$ crystals with pump pulses centered at 1030 nm made possible the generation of MIR radiation in the short wavelength range. In Fig. 5.8 the spectrum for each crystal thickness is reported. The generated radiation is focused by a ZnSe lens into the monochromator for the spectral measurement. To suppress second-order diffraction effects from the monochromator's grating, four long-pass filters with cut-off wavelengths at 1.5, 2.4, 4.5, and 7.3 µm are used, and three different spectra were recorded, respectively, and merged [108]. For the 0.3 mm crystal the spectral coverage spans for almost two octaves, from 2.4 µm to 8 µm within a 10^3 dynamic range.

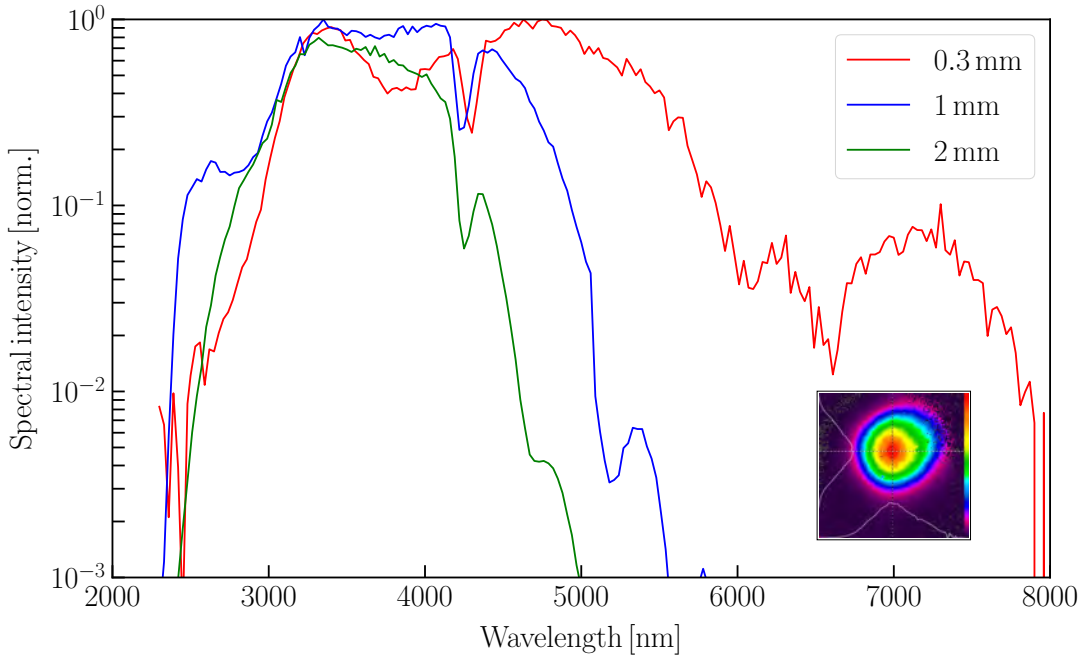

Figure 5.8 Spectra of the MIR radiation generated via IP-DFG in 0.3 mm (red), 1 mm (blue) and 2 mm (green) thick $LiIO_3$ crystals. The traces are recorded with a monochromator (Newport Cornerstone 260). In the inset the beam profile for the 2 mm crystal is shown. The lower spectral intensity above 6 µm is associated with the lower transmission of the crystal in that region [103].

The relatively high power and the broad spectral coverage of this setup demonstrated the possibility to efficiently convert the laser bandwidth to the short-wavelength MIR spectral region. Additionally, the remarkable power stability and the power scala-

bility of this setup paved the way for the application of this source in many fields where intense, CEP-stable short-wavelength MIR radiation would be beneficial, as in transient absorption spectroscopy.

5.3 Conclusion

In this chapter, two different techniques to convert the spectral bandwidth of the frontend towards the MIR and THz spectral region have been presented. The first technique, based on OR in GaP crystals of the pulses from the first generation of MPCs-based compression, was shown to be capable of generating THz radiation with cutoff frequency as high as 5.7 THz with a dynamic range of 10^4 and average power as high as 100 µW. The second technique is based on IP-DFG in $LiIO_3$ crystals of the pulses from the thin plates compression stage. This approach, benefitting from the shorter pulses and the higher stability of the second generation frontend, was shown to be capable of generating MIR radiation with a spectrum spanning for almost two octaves, 2.4-8 µm, with a dynamic range of 10^3, or with average power as high as 70 mW, with a spectrum spanning from 2.4 to 5 µm.

In conclusion, these two different techniques demonstrated the reliability of this system for the generation of radiation in the MIR and THz spectral regions. The power scalability of the frontend as well as of these two generation techniques made Yb:YAG, thin-disk based sources perfect candidates for driving the generation of intense pulses in the MIR to THz region. Additionally, the high dynamic range, robustness, and stability make this compact frontend a promising tool for applications in THz and MIR spectroscopy.

6 Summary and conclusions

In the framework of this thesis, different approaches to extend the bandwidth of a high-power, high-repetition rate Yb:YAG KLM TD oscillator are presented. These efficient broadening schemes for the generation of few-cycle pulses are promising tools to make this type of sources the new frontier of many applications, as the generation and efficient detection of intense and ultrabroadband MIR or THz radiation for biomolecular or chemical absorption spectroscopy [3, 12]. The central work of this thesis was the development of an efficient hybrid-pulse compression scheme to extend the bandwidth of the laser source to the few-cycle regime.

Firstly, the source is briefly presented: a Yb:YAG KLM TD oscillator [22]. It delivers 100 W at 16 MHz repetition rate, corresponding to pulses with 6.3 µJ energy at 220 fs pulse duration. Oscillators based on TD geometry represent, nowadays, the state-of-the-art of solid-state sources. These systems pose a valuable alternative to Ti:Sa lasers for spectroscopic applications thanks to their ability of delivering pulses with a duration of hundreds of femtoseconds at energies up to tens of microjoules with a repetition rate in the MHz range. The limited bandwidth of Yb:YAG-based frontends limits their direct applicability for applications in which broad spectra or ultra-short pulses are required. However, the high extra-cavity peak power and the short pulses directly from the oscillator, achieved with the TD geometry in combination with Yb:YAG gain material and solitonic KLM, has proven to be an ideal starting point for efficient extra-cavity spectral broadening [70]. Moreover, the remarkable stability and the high repetition rate, form the basis for further spectroscopic applications [13], where reproducibility and high signal-to-noise ratio within a reasonable measurement time are crucial.

Secondly, the first stage of nonlinear pulse compression, based on two MPCs is described. This scheme was able to efficiently compress the pulses to sub-18 fs. The first generation, delivering 18 fs at 60.5 W, was used to directly prove the feasibility and the reliability of this frontend and this compression technique for THz generation and

detection [13] as well as for a subsequent compression stage [70]. The second generation, optically and opto-mechanically improved in comparison to the first generation, was able to deliver 17 fs at 74 W. This generation also served as reliable frontend for a subsequent compression stage to extend the bandwidth coverage in spectroscopic applications. Both generations efficiently delivered stable sub-20 fs pulses at high average power and high repetition rate enabling further experiments. The results demonstrate the robustness of this scheme for high power applications and the suitability for the bandwidth extension of Yb-based frontends.

Thirdly, different approaches to reach the few-cycles regime are compared. The limitations in manufacturing multi-layer dispersive optics is the main restriction for extending the bandwidth of MPC-based setups. For further pulse compression, to overcome this limitation and reach the few- and even single-cycle regime, different techniques can be used. A common technique to generate few-cycle pulses is soliton self-compression in a gas-filled hollow-core PCF [31]. For this thesis, a state-of-the-art single-ring hollow-core PCF proved to be capable to deliver 4.5 fs pulses (FTL) with high efficiency and impeccable beam quality [87]. However, in case of small core diameters, ionization can easily occur and damage the fiber tip. In case of a fiber damage, replacement and coupling can be time consuming [84]. Additionally, fibers are very sensitive to in-coupling misalignments and power fluctuations of the input beam. If the desired parameters can only be reached in several compression stages, insensitivity to alignment becomes a key feature. Using a bulk-based compression scheme has some major advantages such as a simple operation, a high reproducible and a compact design [49]. For this reason a second all-bulk-based pulse compression scheme is demonstrated. This scheme is based on a four sapphire thin-plates quasi-waveguide and proved to be capable to deliver 8.5 fs pulses with a good beam quality, high day-to-day reproducibility and remarkable temporal re-compression. Both compression approaches proved to be invaluable and innovative tools to efficiently extend the bandwidth of the Yb:YAG-based sources in a hybrid compression scheme. However, for many applications, and in particular for spectroscopy, the day-to-day reproducibility and reliability of the frontend are key features [37]. For these reasons, a frontend less prone to damage, with lower complexity and more compact as the all-bulk based hybrid compression is preferred.

Finally, some applications, proving the potential of this system, have been presented. Firstly, THz generation via optical rectification in gallium phosphide crystals with the first generation of MPCs was presented. This experimental setup was able to deliver up to 100 µW in 2 mm-thick crystals and cutoff frequencies extending to 5.7 THz in 0.2 mm thick crystal. Secondly, the improvements of the first broadening stage and especially the stable and ultra-short pulses from the all-bulk based hybrid compression scheme

offered a promising platform to generate even broader and more intense pulses. A field where short, intense sources are gaining particular interest is the generation of broadband MIR radiation for spectroscopic applications [3]. Thus, the ability of this compact all-bulk-based frontend to extend the bandwidth coverage of MIR absorption spectroscopy in the short-wavelength region was proved. A spectrum spanning over two octaves in a 0.3-mm-thick $LiIO_3$ crystal and an average power up to 70 mW in a 2-mm-thick $LiIO_3$ crystal were obtained.

In conclusion, an efficient and reliable hybrid compression scheme for high power, high repetition rate sources is presented. The all-bulk-based scheme was able to extend the narrow bandwidth of the state-of-the-art Yb-based source to 8.5 fs. Thus, an unprecedented pulse duration but also a unique peak power of more than 380 MW without the need of further amplification of the laser frontend was achieved. Moreover, the high repetition rate combined with the high intensity and the remarkable stability of this system proved to be beneficial for extending the bandwidth and increasing the intensity of pulses in different spectral regions, paving the way for future applications.

Bibliography

[1] T. H. Maiman, "Stimulated Optical Radiation in Ruby," *Nat.*, vol. 187, no. 4736, pp. 493–494, 1960.

[2] B. P. Abbott, R. Abbott, T. D. Abbott, M. R. Abernathy, F. Acernese, K. Ackley, C. Adams, T. Adams, P. Addesso, R. X. Adhikari, V. B. Adya, C. Affeldt, M. Agathos, K. Agatsuma, N. Aggarwal, O. D. Aguiar, L. Aiello, A. Ain, P. Ajith, B. Allen, A. Allocca, P. A. Altin, and et al., "Observation of Gravitational Waves from a Binary Black Hole Merger," *Phys. Rev. Lett.*, vol. 116, p. 061102, 2016.

[3] I. Pupeza, M. Huber, M. Trubetskov, W. Schweinberger, S. A. Hussain, C. Hofer, K. Fritsch, M. Poetzlberger, L. Vamos, E. Fill, T. Amotchkina, K. V. Kepesidis, A. Apolonski, N. Karpowicz, V. Pervak, O. Pronin, F. Fleischmann, A. Azzeer, M. Žigman, and F. Krausz, "Field-resolved infrared spectroscopy of biological systems," *Nat.*, vol. 577, no. 7788, pp. 52–59, 2020.

[4] V. Sundström, "Femtobiology," *Annu. Rev. Phys. Chem.*, vol. 59, no. 1, pp. 53–77, 2008.

[5] A. H. Zewail, "Femtochemistry: Atomic-Scale Dynamics of the Chemical Bond Using Ultrafast Lasers (Nobel Lecture)," *Angewandte Chemie International Edition*, vol. 39, no. 15, pp. 2586–2631, 2000.

[6] D. E. Spence, P. N. Kean, and W. Sibbett, "60-fsec pulse generation from a self-mode-locked Ti:sapphire laser," *Opt. Lett.*, vol. 16, no. 1, pp. 42–44, 1991.

[7] P. F. Moulton, "Spectroscopic and laser characteristics of Ti:Al2O3," *J. Opt. Soc. Am. B*, vol. 3, no. 1, pp. 125–133, 1986.

[8] O. Pronin and J. Brons, "Kerr-Lens Mode-Locked High-Power Thin-Disk Oscillators," in *High Power Laser Systems* (M. Harooni, ed.), ch. 5, IntechOpen, 2018.

[9] D. Strickland and G. Mourou, "Compression of amplified chirped optical pulses," *Opt. Comm.*, vol. 56, no. 3, pp. 219–221, 1985.

[10] F. Krausz and M. Ivanov, "Attosecond physics," *Rev. Mod. Phys.*, vol. 81, pp. 163–234, 2009.

[11] A. Alismail, H. Wang, G. Barbiero, S. A. Hussain, W. Schweinberger, F. Krausz, and H. Fattahi, "Near-infrared molecular fieldoscopy of water," in *Multiphoton Microscopy in the Biomedical Sciences XIX*, vol. 10882, pp. 310–315, SPIE, 2019.

[12] F. Meyer, N. Hekmat, T. Vogel, A. Omar, S. Mansourzadeh, F. Fobbe, M. Hoffmann, Y. Wang, and C. J. Saraceno, "Milliwatt-class broadband THz source driven by a 112 W, sub-100 fs thin-disk laser," *Opt. Expr.*, vol. 27, no. 21, pp. 30340–30349, 2019.

[13] G. Barbiero, H. Wang, J. Brons, B.-H. Chen, V. Pervak, and H. Fattahi, "Broadband terahertz solid-state emitter driven by Yb:YAG thin-disk oscillator," *J. Phys. B: At. Mol. Opt. Phys.*, vol. 53, no. 12, p. 125601, 2020.

[14] P. Russbueldt, T. Mans, J. Weitenberg, H. D. Hoffmann, and R. Poprawe, "Compact diode-pumped 1.1 kW Yb:YAG Innoslab femtosecond amplifier," *Opt. Lett.*, vol. 35, no. 24, pp. 4169–4171, 2010.

[15] C. J. Saraceno, F. Emaury, O. H. Heckl, C. R. E. Baer, M. Hoffmann, C. Schriber, M. Golling, T. Südmeyer, and K. Keller, "275 W average output power from a femtosecond thin disk oscillator operated in a vacuum environment," *Opt. Expr.*, vol. 20, no. 21, pp. 23535–23541, 2012.

[16] M. Müller, M. Kienel, A. Klenke, T. Gottschall, E. Shestaev, M. Plötner, J. Limpert, and A. Tünnermann, "1 kW 1 mJ eight-channel ultrafast fiber laser," *Opt. Lett.*, vol. 41, no. 15, pp. 3439–3442, 2016.

[17] J. Weitenberg, A. Vernaleken, J. Schulte, A. Ozawa, T. Sartorius, V. Pervak, H.-D. Hoffmann, T. Udem, P. Russbüldt, and T. W. Hänsch, "Multi-pass-cell-based nonlinear pulse compression to 115 fs at 7.5 µJ pulse energy and 300 W average power," *Opt. Expr.*, vol. 25, pp. 20502–20510, Aug 2017.

[18] J. Weitenberg, T. Saule, J. Schulte, and P. Rusbuldt, "Nonlinear Pulse Compression to Sub-40 fs at 4.5 µJ Pulse Energy by Multi-Pass-Cell Spectral Broadening," *IEEE J. Quant. Electr.*, vol. 53, no. 6, pp. 1–4, 2017.

[19] S. Hädrich, M. Krebs, A. Hoffmann, A. Klenke, J. Rothhardt, J. Limpert, and

A. Tünnermann, "Exploring new avenues in high repetition rate table-top coherent extreme ultraviolet sources," *Light: Science & Applications*, vol. 4, no. 8, pp. e320–e320, 2015.

[20] I. Pupeza, S. Holzberger, T. Eidam, H. Carstens, D. Esser, J. Weitenberg, P. Rußbüldt, J. Rauschenberger, J. Limpert, T. Udem, A. Tünnermann, T. W. Hänsch, A. Apolonski, F. Krausz, and E. Fill, "Compact high-repetition-rate source of coherent 100 eV radiation," *Nat. Phot.*, vol. 7, no. 8, pp. 608–612, 2013.

[21] C. Gohle, T. Udem, M. Herrmann, J. Rauschenberger, R. Holzwarth, H. A. Schuessler, F. Krausz, and T. W. Hänsch, "A frequency comb in the extreme ultraviolet," *Nat.*, vol. 436, no. 7048, pp. 234–237, 2005.

[22] J. Brons, V. Pervak, D. Bauer, D. Sutter, O. Pronin, and F. Krausz, "Powerful 100-fs-scale Kerr-lens mode-locked thin-disk oscillator," *Opt. Lett.*, vol. 41, no. 15, pp. 3567–3570, 2016.

[23] J. Körner, V. Jambunathan, J. Hein, R. Seifert, M. Loeser, M. Siebold, U. Schramm, P. Sikocinski, A. Lucianetti, T. Mocek, and M. C. Kaluza, "Spectroscopic characterization of Yb^{3+}-doped laser materials at cryogenic temperatures," *App. Phys. B*, vol. 116, no. 1, pp. 75–81, 2014.

[24] J. Schulte, T. Sartorius, J. Weitenberg, A. Vernaleken, and P. Russbueldt, "Nonlinear pulse compression in a multi-pass cell," *Opt. Lett.*, vol. 41, no. 19, pp. 4511–4514, 2016.

[25] W. Liu, D. N. Schimpf, T. Eidam, J. Limpert, A. Tünnermann, F. X. Kärtner, and G. Chang, "Pre-chirp managed nonlinear amplification in fibers delivering 100 W, 60 fs pulses," *Opt. Lett.*, vol. 40, no. 2, pp. 151–154, 2015.

[26] Y. Liu, W. Li, D. Luo, D. Bai, C. Wang, and H. Zeng, "Generation of 33 fs 93.5 W average power pulses from a third-order dispersion managed self-similar fiber amplifier," *Opt. Expr.*, vol. 24, no. 10, pp. 10939–10945, 2016.

[27] C. Jocher, T. Eidam, S. Hädrich, J. Limpert, and A. Tünnermann, "Sub 25 fs pulses from solid-core nonlinear compression stage at 250 W of average power," *Opt. Lett.*, vol. 37, no. 21, pp. 4407–4409, 2012.

[28] A. Vernaleken, J. Weitenberg, T. Sartorius, P. Russbueldt, W. Schneider, S. L. Stebbings, M. F. Kling, P. Hommelhoff, H.-D. Hoffmann, R. Poprawe, F. Krausz, T. W. Hänsch, and T. Udem, "Single-pass high-harmonic generation at 20.8 MHz

repetition rate," *Opt. Lett.*, vol. 36, no. 17, pp. 3428–3430, 2011.

[29] H. Carstens, M. Högner, T. Saule, S. Holzberger, N. Lilienfein, A. Guggenmos, C. Jocher, T. Eidam, D. Esser, V. Tosa, V. Pervak, J. Limpert, A. Tünnermann, U. Kleineberg, F. Krausz, and I. Pupeza, "High-harmonic generation at 250 MHz with photon energies exceeding 100 eV," *Optica*, vol. 3, no. 4, pp. 366–369, 2016.

[30] S. Hädrich, A. Klenke, J. Rothhardt, M. Krebs, A. Hoffmann, O. Pronin, V. Pervak, J. Limpert, and A. Tünnermann, "High photon flux table-top coherent extreme-ultraviolet source," *Nat. Phot.*, vol. 8, no. 10, pp. 779–783, 2014.

[31] F. F Benabid, J. C. Knight, G. Antonopoulos, and P. S.-J. Russell, "Stimulated Raman scattering in hydrogen-filled hollow-core photonic crystal fiber," *Science*, vol. 298, no. 5592, pp. 399–402, 2002.

[32] F. Köttig, F. Tani, C. M. Biersach, J. C. Travers, and P. S. Russell, "Generation of microjoule pulses in the deep ultraviolet at megahertz repetition rates," *Optica*, vol. 4, no. 10, pp. 1272–1276, 2017.

[33] S. Gröbmeyer, J. Brons, M. Seidel, and O. Pronin, "Laser Stabilization: Carrier-Envelope-Offset Frequency Stable 100 W-Level Femtosecond Thin-Disk Oscillator," *Laser & Photonics Rev.*, vol. 13, no. 3, p. 1970017, 2019.

[34] J. R. Koehler, F. Köttig, B. M. Trabold, F. Tani, and P. S. Russell, "Long-Lived Refractive-Index Changes Induced by Femtosecond Ionization in Gas-Filled Single-Ring Photonic-Crystal Fibers," *Phys. Rev. Applied*, vol. 10, p. 064020, 2018.

[35] B. M. Trabold, M. I. Suresh, J. R. Koehler, M. H. Frosz, F. Tani, and P. S. J. Russell, "Spatio-temporal measurement of ionization-induced modal index changes in gas-filled PCF by prism-assisted side-coupling," *Opt. Expr.*, vol. 27, pp. 14392–14399, May 2019.

[36] F. Guichard, Y. Zaouter, M. Hanna, F. Morin, C. Hönninger, E. Mottay, F. Druon, and P. Georges, "Energy scaling of a nonlinear compression setup using passive coherent combining," *Opt. Lett.*, vol. 38, no. 21, p. 4437, 2013.

[37] M. Seidel, G. Arisholm, J. Brons, V. Pervak, and O. Pronin, "All solid-state spectral broadening: an average and peak power scalable method for compression of ultrashort pulses," *Opt. Exp.*, vol. 24, no. 9, pp. 9412–9428, 2016.

[38] C.-H. Lu, Y.-J. Tsou, H.-Y. Chen, B.-H. Chen, Y.-C. Cheng, S.-D. Yang, M.-C. Chen, C.-C. Hsu, and A. H. Kung, "Generation of intense supercontinuum in con-

densed media," *Optica*, vol. 1, no. 6, pp. 400–406, 2014.

[39] P. He, Y. Liu, K. Zhao, H. Teng, X. He, P. Huang, H. Huang, S. Zhong, Y. Jiang, S. Fang, X. Hou, and Z. Wei, "High-efficiency supercontinuum generation in solid thin plates at 0.1 TW level," *Opt. Lett.*, vol. 42, no. 3, pp. 474–477, 2017.

[40] K. Fritsch, M. Poetzlberger, V. Pervak, J. Brons, and O. Pronin, "All-solid-state multipass spectral broadening to sub-20 fs," *Opt. Lett.*, vol. 43, no. 19, pp. 4643–4646, 2018.

[41] M. Kaumanns, V. Pervak, D. Kormin, V. Leshchenko, A. Kessel, M. Ueffing, Y. Chen, and T. Nubbemeyer, "Multipass spectral broadening of 18 mJ pulses compressible from 1.3 ps to 41 fs," *Opt. Lett.*, vol. 43, no. 23, pp. 5877–5880, 2018.

[42] M. Kaumanns, D. Kormin, T. Nubbemeyer, V. Pervak, and S. Karsch, "Spectral broadening of 112 mJ, 1.3 ps pulses at 5 kHz in a LG_{10} multipass cell with compressibility to 37 fs," *Opt. Lett.*, vol. 46, no. 5, pp. 929–932, 2021.

[43] M. Ueffing, S. Reiger, M. Kaumanns, V. Pervak, M. Trubetskov, T. Nubbemeyer, and F. Krausz, "Nonlinear pulse compression in a gas-filled multipass cell," *Opt. Lett.*, vol. 43, no. 9, pp. 2070–2073, 2018.

[44] L. Lavenu, M. Natile, F. Guichard, Y. Zaouter, X. Delen, M. Hanna, E. Mottay, and P. Georges, "Nonlinear pulse compression based on a gas-filled multipass cell," *Opt. Lett.*, vol. 43, no. 10, pp. 2252–2255, 2018.

[45] P. Balla, A. B. Wahid, I. Sytcevich, C. Guo, A.-L. Viotti, L. Silletti, A. Cartella, S. Alisauskas, H. Tavakol, U. Grosse-Wortmann, A. Schönberg, M. Seidel, A. Trabattoni, B. Manschwetus, T. Lang, F. Calegari, A. Couairon, A. L'Huillier, C. L. Arnold, I. Hartl, and C. M. Heyl, "Postcompression of picosecond pulses into the few-cycle regime," *Opt. Lett.*, vol. 45, no. 9, pp. 2572–2575, 2020.

[46] E. Vicentini, Y. Wang, D. Gatti, A. Gambetta, P. Laporta, G. Galzerano, K. Curtis, K. McEwan, C. R. Howle, and N. Coluccelli, "onlinear pulse compression to 22 fs at 15.6 µJ by an all-solid-state multipass approach," *Opt. Expr.*, vol. 28, no. 4, pp. 4541–4549, 2020.

[47] S. Gröbmeyer, K. Fritsch, B. Schneider, M. Poetzlberger, V. Pervak, J. Brons, and O. Pronin, "Self-compression at 1 µm wavelength in all-bulk multi-pass geometry," *Applied Physics B*, vol. 126, no. 10, 2020.

[48] K. F. Mak, M. Seidel, O. Pronin, M. H. Frosz, A. Abdolvand, V. Pervak, A. Apolon-

ski, F. Krausz, J. C. Travers, and P. S. J. Russell, "Compressing µ J-level pulses from 250 fs to sub-10 fs at 38-MHz repetition rate using two gas-filled hollow-core photonic crystal fiber stages," *Opt. Lett.*, vol. 40, no. 7, pp. 1238–1241, 2015.

[49] J. Brons, *High-power femtosecond laser-oscillators for applications in high-field physics*. PhD thesis, Ludwigs-Maximilians-Universität München, 2017.

[50] M. Seidel, J. Brons, G. Arisholm, K. Fritsch, V. Pervak, and O. Pronin, "Efficient High-Power Ultrashort Pulse Compression in Self-Defocusing Bulk Media," *Scientific Reports*, vol. 7, no. 1, p. 1410, 2017.

[51] W. Koechner, *Solid-State Laser Engineering*. Springer Series in Optical Sciences, Springer, 2006.

[52] C. J. Saraceno, F. Emaury, C. Schriber, A. Diebold, M. Hoffmann, M. Golling, T. Sudmeyer, and U. Keller, "Toward Millijoule-Level High-Power Ultrafast Thin-Disk Oscillators," *IEEE J. Quantum Electron.*, vol. 21, no. 1, pp. 106–123, 2015.

[53] D. C. Brown and V. A. Vitali, "Yb:YAG Kinetics Model Including Saturation and Power Conservation," *IEEE J. Quantum Electron.*, vol. 47, no. 1, pp. 3–12, 2011.

[54] J. Brons, V. Pervak, E. Fedulova, D. Bauer, D. Sutter, V. Kalashnikov, A. Apolonskiy, O. Pronin, and F. Krausz, "Energy scaling of Kerr-lens mode-locked thin-disk oscillators," *Opt. Lett.*, vol. 39, no. 22, pp. 6442–6445, 2014.

[55] B. L. Volodin, S. V. Dolgy, E. D. Melnik, E. Downs, J. Shaw, and V. S. Ban, "Wavelength stabilization and spectrum narrowing of high-power multimode laser diodes and arrays by use of volume Bragg gratings," *Opt. Lett.*, vol. 29, no. 16, pp. 1891–1893, 2004.

[56] G. Huber, C. Kränkel, and K. Petermann, "Solid-state lasers: status and future," *J. Opt. Soc. Am. B*, vol. 27, no. 11, pp. B93–B105, 2010.

[57] A. Giesen, H. Hügel, A. Voss, K. Wittig, U. Brauch, and H. Opower, "Scalable concept for diode-pumped high-power solid-state lasers," *App. Phys. B*, vol. 58, no. 5, pp. 365–372, 1994.

[58] J.-P. Negel, A. Loescher, A. Voss, D. Bauer, D. Sutter, A. Killi, M. A. Ahmed, and T. Graf, "Ultrafast thin-disk multipass laser amplifier delivering 1.4 kW (4.7 mJ, 1030 nm) average power converted to 820 W at 515 nm and 234 W at 343 nm," *Opt. Exp.*, vol. 23, no. 16, pp. 21064–21077, 2015.

[59] T. Nubbemeyer, M. Kaumanns, U. Ueffing, M. Gorjan, A. Alismail, H. Fattahi, J. Brons, O. Pronin, H. G. Barros, Z. Major, T. Metzger, D. Sutter, and F. Krausz, "1 kW, 200 mJ picosecond thin-disk laser system," *Opt. Lett.*, vol. 42, no. 7, pp. 1381–1384, 2017.

[60] C. J. Saraceno, D. Sutter, T. Metzger, and A. A. Marwan, "The amazing progress of high-power ultrafast thin-disk lasers," *J. Eur. Opt. Soc.*, vol. 15, no. 1, 2019.

[61] J. aus der Au, G. J. Spühler, T. Südmeyer, R. Paschotta, R. Hövel, M. Moser, S. Erhard, M. Karszewski, A. Giesen, and U. Keller, "16.2-W average power from a diode-pumped femtosecond Yb:YAG thin disk laser," *Opt. Lett.*, vol. 25, no. 11, pp. 859–861, 2000.

[62] C. J. Saraceno, F. Emaury, C. Schriber, M. Hoffmann, M. Golling, T. Südmeyer, and U. Keller, "Ultrafast thin-disk laser with 80 µ J pulse energy and 242 W of average power," *Opt. Lett.*, vol. 39, no. 1, pp. 9–12, 2014.

[63] E. Fedulova, F. Fritsch, J. Brons, O. Pronin, T. Amotchkina, M. Trubetskov, F. Krausz, and V. Pervak, "Highly-dispersive mirrors reach new levels of dispersion," *Opt. Exp.*, vol. 23, no. 11, pp. 13788–13793, 2015.

[64] O. Pronin, J. Brons, C. Grasse, V. Pervak, G. Boehm, M.-C. Amann, A. Apolonski, V. L. Kalashnikov, and F. Krausz, "High-power Kerr-lens mode-locked Yb:YAG thin-disk oscillator in the positive dispersion regime," *Opt. Lett.*, vol. 37, no. 17, pp. 3543–3545, 2012.

[65] J. Zhang, J. Brons, N. Lilienfein, E. Fedulova, V. Pervak, B. Bauer, D. Sutter, Z. Wei, A. Apolonski, O. Pronin, and F. Krausz, "260-megahertz, megawatt-level thin-disk oscillator," *Opt. Lett.*, vol. 40, no. 8, pp. 1627–1630, 2015.

[66] V. Magni, "Multielement stable resonators containing a variable lens," *J. Opt. Soc. Am. A*, vol. 10, no. 4, 1987.

[67] N. I. Chunosov, "Rezonator2." `http://rezonator.orion-project.org/`, 2006-2020.

[68] K. W. DeLong, R. Trebino, J. Hunter, and W. E. White, "Frequency-resolved optical gating with the use of second-harmonic generation," *J. Opt. Soc. Am. B*, vol. 11, no. 11, pp. 2206–2215, 1994.

[69] J. Ratner, G. Steinmeyer, T. C. Wong, R. Bartels, and R. Trebino, "Coherent artifact in modern pulse measurements," *Opt. Lett.*, vol. 37, no. 14, pp. 2874–2876,

2012.

[70] G. Barbiero, R. N. Ahmad, H. Wang, F. Köttig, D. Novoa, F. Tani, J. Brons, P. S.-J. Russell, F. Krausz, and H. Fattahi, "Towards 45 Watt Single-Cycle Pulses from Yb:YAG Thin-Disk Oscillators," in *2019 Conference on Lasers and Electro-Optics Europe European Quantum Electronics Conference (CLEO/Europe-EQEC)*, pp. 1–1, 2019.

[71] R. Boyd, *Nonlinear Optics*. Elsevier Science, 2003.

[72] A. Weiner, *Ultrafast Optics*. Wiley Series in Pure and Applied Optics, Wiley, 2011.

[73] G. Agrawal, *Nonlinear Fiber Optics*. Optics and Photonics, Elsevier Science, 2013.

[74] M. Hanna, X. Délen, L. Lavenu, F. Guichard, Y. Zaouter, F. Druon, and P. Georges, "Nonlinear temporal compression in multipass cells: theory," *Journal of the Optical Society of America B*, vol. 34, no. 7, p. 1340, 2017.

[75] E. Goulielmakis, M. Schultze, M. Hofstetter, V. S. Yakovlev, J. Gagnon, M. Uiberacker, A. L. Aquila, E. M. Gullikson, D. T. Attwood, R. Kienberger, F. Krausz, and U. Kleineberg, "Single-Cycle Nonlinear Optics," *Science*, vol. 320, no. 5883, pp. 1614–1617, 2008.

[76] J. Hult, "A Fourth-Order Runge–Kutta in the Interaction Picture Method for Simulating Supercontinuum Generation in Optical Fibers," *J. Lightwave Technol.*, vol. 25, no. 12, pp. 3770–3775, 2007.

[77] S. Gröbmeyer. PhD thesis, Ludwigs-Maximilians-Universität München, 2020.

[78] D. Herriott, H. Kogelnik, and R. Kompfner, "Off-axis paths in spherical mirror interferometers," *Applied Optics*, vol. 3, no. 4, p. 523, 1964.

[79] B. Perry, R. O. Brickman, A. Stein, E. B. Treacy, and P. Rabinowitz, "Controllable pulse compression in a multiple-pass-cell raman laser," *Optics letters*, vol. 5, no. 7, pp. 288–290, 1980.

[80] R. Szipöcs, K. Ferencz, C. Spielmann, and F. Krausz, "Chirped multilayer coatings for broadband dispersion control in femtosecond lasers," *Opt. Lett.*, vol. 19, no. 3, pp. 201–203, 1994.

[81] J.-C. Diels and W. Rudolph, *Ultrashort Laser Pulse Phenomena Fundamentals*. Elsevier Science, 2006.

[82] V. Pervak, O. Pronin, O. Razskazovskaya, J. Brons, I. B. Angelov, M. K. Trubetskov, A. V. Tikhonravov, and F. Krausz, "High-dispersive mirrors for high power applications," *Opt. Express*, vol. 20, no. 4, pp. 4503–4508, 2012.

[83] F. DeMartini, C. H. Townes, T. K. Gustafson, and P. L. Kelley, "Self-Steepening of Light Pulses," *Phys. Rev.*, vol. 164, pp. 312–323, Dec 1967.

[84] M. Graßl, "Sub-10 fs Compression of MHz High-Power Yb:YAG Thin-Disk Oscillator Pulses," Master's thesis, Technische Universität München, 2021.

[85] D. Polli, V. Kumar, C. M. Valensise, M. Marangoni, and G. Cerullo, "Broadband coherent raman scattering microscopy," *Laser & Photonics Reviews*, vol. 12, no. 9, p. 1800020, 2018.

[86] S. Rahav and S. Mukamel, "Stimulated coherent anti-Stokes Raman spectroscopy (CARS) resonances originate from double-slit interference of two-photon Stokes pathways," *Proceedings of the National Academy of Sciences*, vol. 107, no. 11, pp. 4825–4829, 2010.

[87] F. Köttig, F. Tani, and P. S. Russell, "Modulational-instability-free pulse compression in anti-resonant hollow-core photonic crystal fiber," *Opt. Lett.*, vol. 45, no. 14, pp. 4044–4047, 2020.

[88] F. Köttig, *Strong-Field Nonlinear Fiber Optics*. PhD thesis, Friedrich-Alexander-Universität Erlangen-Nürnberg, 2018.

[89] J. C. Travers, W. Chang, J. Nold, N. Y. Joly, and P. S. J. Russell, "Ultrafast nonlinear optics in gas-filled hollow-core photonic crystal fibers [Invited]," *J. Opt. Soc. Am. B*, vol. 28, no. 12, pp. A11–A26, 2011.

[90] P. J. St. Russell, P. Hölzer, W. Chang, A. Abdolvand, and J. C. Travers, "Hollow-core photonic crystal fibres for gas-based nonlinear optics," *Nature Photonics*, vol. 8, no. 4, pp. 278–286, 2014.

[91] M. Nisoli, S. De Silvestri, and O. Svelto, "Generation of high energy 10 fs pulses by a new pulse compression technique," *Appl. Phys. Let.*, vol. 68, no. 20, pp. 2793–2795, 1996.

[92] E. A. J. Marcatili and R. A. Schmeltzer, "Hollow metallic and dielectric waveguides for long distance optical transmission and lasers," *The Bell System Technical Journal*, vol. 43, no. 4, pp. 1783–1809, 1964.

[93] F. Tani, *Extreme nonlinear optics in gas-filled hollow-core fibres.* PhD thesis, Friedrich-Alexander-Universität Erlangen-Nürnberg, 2014.

[94] S. Hädrich, M. Kienel, M. Müller, A. Klenke, J. Rothhardt, R. Klas, T. Gottschall, T. Eidam, A. Drozdy, P. Jójárt, Z. Várallyay, E. Cormier, K. Osvay, A. Tünnermann, and J. Limpert, "Energetic sub-2-cycle laser with 216 W average power," *Opt. Lett.*, vol. 41, no. 18, pp. 4332–4335, 2016.

[95] W. P. Leemans, B. Nagler, A. J. Gonsalves, C. Tóth, K. Nakamura, C. G. R. Geddes, E. Esarey, C. B. Schroeder, and S. M. Hooker, "GeV electron beams from a centimetre-scale accelerator," *Nat. Phys.*, vol. 2, no. 10, pp. 696–699, 2006.

[96] C. Markos, J. C. Travers, A. Abdolvand, B. J. Eggleton, and O. Bang, "Hybrid photonic-crystal fiber," *Rev. Mod. Phys.*, vol. 89, p. 045003, 2017.

[97] A. D. Pryamikov, A. S. Biriukov, A. F. Kosolapov, V. G. Plotnichenko, S. L. Semjonov, and E. M. Dianov, "Demonstration of a waveguide regime for a silica hollow - core microstructured optical fiber with a negative curvature of the core boundary in the spectral region > 3.5 µm," *Opt. Expr.*, vol. 19, no. 2, pp. 1441–1448, 2011.

[98] K. F. Mak, *Nonlinear optical effects in gas-filled hollow-core photonic-crystal fibers.* PhD thesis, Friedrich-Alexander-Universität Erlangen-Nürnberg, 2014.

[99] T. Balciunas, C. Fourcade-Dutin, G. Fan, T. Witting, A. A. Voronin, A. M. Zheltikov, F. Gerome, G. G. Paulus, A. Baltuska, and F. Benabid, "A strong-field driver in the single-cycle regime based on self-compression in a kagome fibre," *Nat. Comm.*, vol. 6, no. 1, p. 6117, 2015.

[100] S. Vlasov, E. Koposova, and V. Yashin, "Spectral broadening and compression of high-intensity laser pulses in quasi-periodic systems with Kerr nonlinearity," *Quantum Electron.*, vol. 42, 2012.

[101] C.-L. Tsai, F. Meyer, A. Omar, Y. Wang, A.-Y. Liang, C.-H. Lu, M. Hoffmann, S.-D. Yang, and C. J. Saraceno, "Efficient nonlinear compression of a mode-locked thin-disk oscillator to 27 fs at 98 W average power," *Opt. Lett.*, vol. 44, no. 17, pp. 4115–4118, 2019.

[102] M. Seo, K. Tsendsuren, S. Mitra, M. Kling, and D. Kim, "High-contrast, intense single-cycle pulses from an all thin-solid-plate setup," *Opt. Lett.*, vol. 45, no. 2, pp. 367–370, 2020.

[103] M. Weber, *Handbook of Optical Materials*. Laser & Optical Science & Technology, Taylor & Francis, 2002.

[104] Y. Zhang, X. Ji, H. Zhang, X. Li, T. Wang, H. Wang, and Y. Deng, "Self-focusing and group-velocity dispersion of pulsed laser beams in the inhomogeneous atmosphere," *Opt. Expr.*, vol. 26, no. 11, pp. 14617–14625, 2018.

[105] K. Okamoto, *Fundamentals of Optical Waveguides*. Electronics & Electrical, Elsevier Science, 2006.

[106] H. Oukraou, V. Coda, A. A. Rangelov, and G. Montemezzani, "Broadband photonic transport between waveguides by adiabatic elimination," *Phys. Rev. A*, vol. 97, p. 023811, 2018.

[107] C. J. Saraceno, "Mode-locked thin-disk lasers and their potential application for high-power terahertz generation," *J. Opt.*, vol. 20, no. 4, p. 044010, 2018.

[108] J. Zhang, Q. Wang, J. Hao, H. Liu, J. Yao, Z. Li, J. Liu, and K. F. Mak, "Broadband, few-cycle mid-infrared continuum based on the intra-pulse difference frequency generation with BGSe crystals," *Opt. Expr.*, vol. 28, no. 25, pp. 37903–37909, 2020.

[109] S. S. Dhillon, M. S. Vitiello, E. H. Linfield, A. G. Davies, M. C. Hoffmann, J. Booske, C. Paoloni, M. Gensch, P. Weightman, G. P. Williams, *et al.*, "The 2017 terahertz science and technology roadmap," *J. Phys. D: Applied Physics*, vol. 50, no. 4, p. 043001, 2017.

[110] C. Manzoni and G. Cerullo, "Design criteria for ultrafast optical parametric amplifiers," *J. Opt.*, vol. 18, no. 10, p. 103501, 2016.

[111] H. Fattahi, H. G. Barros, M. Gorjan, T. Nubbemeyer, B. Alsaif, C. Y. Teisset, M. Schultze, S. Prinz, M. Haefner, M. Ueffing, *et al.*, "Third-generation femtosecond technology," *Optica*, vol. 1, no. 1, pp. 45–63, 2014.

[112] N. Kanda, N. Ishii, J. Itatani, and R. Matsunaga, "Optical parametric amplification of phase-stable terahertz-to-mid-infrared pulses studied in the time domain," *Opt. Expr.*, vol. 29, pp. 3479–3489, Feb 2021.

[113] J. R. Morris and Y. R. Shen, "Far-infrared generation by picosecond pulses in electro-optical materials," *Opt. Comm.*, vol. 3, no. 2, pp. 81–84, 1971.

[114] K. H. Yang, P. L. Richards, and Y. R. Shen, "Generation of far-infrared radiation by picosecond light pulses in $LiNbO_3$," *App. Phys. Lett.*, vol. 19, no. 9, pp. 320–323,

1971.

[115] D. H. Auston, K. P. Cheung, J. A. Valdmanis, and D. A. Kleinman, "Cherenkov radiation from femtosecond optical pulses in electro-optic media," *Phys. Rev. Lett.*, vol. 53, no. 16, p. 1555, 1984.

[116] J. A. Fülöp, L. Pálfalvi, G. Almási, and J. Hebling, "High Energy THz Pulse Generation by Tilted Pulse Front Excitation and Its Nonlinear Optical Applications," *Journal of Infrared, Millimeter, and Terahertz Waves*, vol. 32, no. 5, pp. 553–561, 2011.

[117] I. Wilke and S. Sengupta, "Nonlinear optical techniques for terahertz pulse generation and detection optical rectification and electrooptic sampling," in *Terahertz spectroscopy: Principles and applications*, ch. 2, Chemical Rubber Company, 2007.

[118] J. A. Fülöp, L. Pálfalvi, G. Almási, and J. Hebling, "Design of high-energy terahertz sources based on optical rectification," *Opt. expr.*, vol. 18, no. 12, pp. 12311–12327, 2010.

[119] Y. Chu, X. Liang, L. Yu, Y. Xu, L. Xu, L. Ma, X. Lu, Y. Liu, Y. Leng, R. Li, *et al.*, "High-contrast 2.0 Petawatt Ti:Sapphire laser system," *Opt. Expr.*, vol. 21, no. 24, pp. 29231–29239, 2013.

[120] N. Karpowicz, J. Dai, X. Lu, Y. Chen, M. Yamaguchi, H. Zhao, X.-C. Zhang, L. Zhang, C. Zhang, M. Price-Gallagher, *et al.*, "Coherent heterodyne time-domain spectrometry covering the entire "terahertz gap"," *Appl. Phys. Lett.*, vol. 92, no. 1, p. 011131, 2008.

[121] X. Xie, J. Dai, and X.-C. Zhang, "Coherent Control of THz Wave Generation in Ambient Air," *Phys. Rev. Lett.*, vol. 96, p. 075005, 2006.

[122] T. Bartel, P. Gaal, K. Reimann, M. Woerner, and T. Elsaesser, "Generation of single-cycle THz transients with high electric-field amplitudes," *Opt. Lett.*, vol. 30, no. 20, pp. 2805–2807, 2005.

[123] Y. Hua, W. Liu, M. Hemmer, L. E. Zapata, G. Zhou, D. N. Schimpf, T. Eidam, J. Limpert, A. Tünnermann, F. X. Kärtner, *et al.*, "87-W 1018-nm Yb-fiber ultrafast seeding source for cryogenic Yb: yttrium lithium fluoride amplifier," *Opt. Lett.*, vol. 43, no. 8, pp. 1686–1689, 2018.

[124] N. Hekmat, T. Vogel, Y. Wang, S. Mansourzadeh, A. Omar, F. Aslani, M. Hoffmann, F. Meyer, and C. J. Saraceno, "Cryogenically cooled GaP for optical rectification at

high excitation average powers," *Opt. Mater. Express*, vol. 10, no. 11, pp. 2768–2782, 2020.

[125] T. Isao, S. Hiroyuki, I. Hiroshi, T. Hirokazu, A. Katsuhiro, R. Rakchanok, and U. Yuko, "7 Terahertz-wave generation from quasi-phase-matched GaP for 1.55 µm pumping," *Appl. Phys. Lett.*, vol. 88, no. 7, p. 071118, 2006.

[126] G. Chang, C. J. Divin, C.-H. Liu, S. L. Williamson, A. Galvanauskas, and T. B. Norris, "Power scalable compact THz system based on an ultrafast Yb-doped fiber amplifier," *Opt. Expr.*, vol. 14, no. 17, pp. 7909–7913, 2006.

[127] M. C. Hoffmann, K.-L. Yeh, H. Y. Hwang, T. S. Sosnowski, B. S. Prall, J. Hebling, and K. A. Nelson, "Fiber laser pumped high average power single-cycle terahertz pulse source," *Appl. Phys. Lett.*, vol. 93, no. 14, p. 141107, 2008.

[128] J. Li, L. Chai, J. Shi, B. Liu, B. Xu, M. Hu, Y. Li, Q. Xing, C. Wang, A. B. Fedotov, *et al.*, "Efficient terahertz wave generation from GaP crystals pumped by chirp-controlled pulses from femtosecond photonic crystal fiber amplifier," *Appl. Phys. Lett.*, vol. 104, no. 3, p. 031117, 2014.

[129] J. Xu, B. Globisch, C. Hofer, N. Lilienfein, T. Butler, N. Karpowicz, and I. Pupeza, "Three-octave terahertz pulses from optical rectification of 20 fs, 1 µm, 78 MHz pulses in GaP," *J. Phys. B: At. Mol. Opt. Phys.*, vol. 51, p. 154002, jul 2018.

[130] C. Paradis, J. Drs, N. Modsching, O. Razskazovskaya, F. Meyer, C. Kränkel, C. J. Saraceno, V. J. Wittwer, and T. Südmeyer, "Broadband terahertz pulse generation driven by an ultrafast thin-disk laser oscillator," *Opt. Expr.*, vol. 26, no. 20, pp. 26377–26384, 2018.

[131] J. Drs, N. Modsching, C. Paradis, C. Kränkel, V. J. Wittwer, O. Razskazovskaya, and T. Südmeyer, "Optical rectification of ultrafast Yb lasers: pushing power and bandwidth of terahertz generation in GaP," *J. Opt. Soc. Am. B*, vol. 36, pp. 3039–3045, Nov 2019.

[132] Q. Wu and X.-C. Zhang, "7 terahertz broadband GaP electro-optic sensor," *Appl. Phys. Lett.*, vol. 70, no. 14, pp. 1784–1786, 1997.

[133] A. Leitenstorfer, S. Hunsche, J. Shah, M. C. Nuss, and W. H. Knox, "Detectors and sources for ultrabroadband electro-optic sampling: Experiment and theory," *Appl. Phys. Lett.*, vol. 74, no. 11, pp. 1516–1518, 1999.

[134] M. Porer, J.-M. Ménard, and R. Huber, "Shot noise reduced terahertz detection via

spectrally postfiltered electro-optic sampling," *Opt. Lett.*, vol. 39, no. 8, pp. 2435–2438, 2014.

[135] H. J. Bakker, G. C. Cho, H. Kurz, Q. Wu, and X.-C. Zhang, "Distortion of terahertz pulses in electro-optic sampling," *J. Opt. Soc. Am. B*, vol. 15, no. 6, pp. 1795–1801, 1998.

[136] M. van Exter, C. Fattinger, and D. Grischkowsky, "Terahertz time-domain spectroscopy of water vapor," *Opt. Lett.*, vol. 14, no. 20, pp. 1128–1130, 1989.

[137] I. Gordon, L. Rothman, C. Hill, R. Kochanov, Y. Tan, P. Bernath, M. Birk, V. Boudon, A. Campargue, K. Chance, B. Drouin, J.-M. Flaud, R. Gamache, J. Hodges, D. Jacquemart, V. Perevalov, A. Perrin, K. Shine, M.-A. Smith, J. Tennyson, G. Toon, H. Tran, V. Tyuterev, A. Barbe, A. Császár, V. Devi, T. Furtenbacher, J. Harrison, J.-M. Hartmann, A. Jolly, T. Johnson, T. Karman, I. Kleiner, A. Kyuberis, J. Loos, O. Lyulin, S. Massie, S. Mikhailenko, N. Moazzen-Ahmadi, H. Müller, O. Naumenko, A. Nikitin, O. Polyansky, M. Rey, M. Rotger, S. Sharpe, K. Sung, E. Starikova, S. Tashkun, J. V. Auwera, G. Wagner, J. Wilzewski, P. Wcisło, S. Yu, and E. Zak, "The HITRAN2016 molecular spectroscopic database," *J. Quant. Spectrosc. Radiat. Transf.*, vol. 203, pp. 3–69, 2017. HITRAN2016 Special Issue.

Acknowledgments

Many people, in many different ways, contributed to this work. Without them, nothing of what has been achieved in this thesis would have been possible.
Firstly, I would like to thank Prof. Dr. Ferenc Krausz and Prof. Dr. Matthias F. Kling for giving me the opportunity to join the Attoworld team and especially for providing your invaluable guidance and continuous support along my entire PhD. My research skills dramatically benefited from both your extensive knowledge and your vision.
My deep gratitude goes to Dr. Hanieh Fattahi for being my direct supervisor for more than half of my PhD. Thanks for constantly encouraging me (also remotely) and for teaching me so much.
I would like to especially thank Dr. Haochuan Wang for being a wonderful team mate, for patiently reading my thesis and patiently telling me once more how phase matching works. Your calm character, your optimistic perspective and your deep knowledge about physics and optics changed me, in better.
My gratitude goes also to the other two members of the *Raman Team*: Dziugas Kimbaras and Martin Graßl. You contributed differently to my project but without you nothing would have been the same.
I also would like to thank Dr. Jonathan Brons, for leaving me time to learn alone but always being present on the other side of the phone. You taught me so many valuable skills. Thanks also to Dr. Thomas Nubbemeyer, he watched me growing up without interfering but always being there in case I needed help. A special thanks goes to the whole *Kling's group*. You all accepted me as part of your team without any hesitation.
My gratitude goes also to with Felix Köttig at the Max-Planck-Institute for the Science of Light who collaborated with out team for the fiber-based compression approach.
I would also like to thank all the people in the *Attoworld* framework and in the *IMPRS-APS* graduate school for the continuous support and the many ideas, which came out from the uncountable talks I attended.
A special thanks goes to the technical and administrative staff, especially to Dr. Hans F. Wirth, Florian Saran, LMU mechanical workshorp, Katharina Adler and Klaus Franke. Your support was very important during the past years.
Of course, nothing of this would ever been possible without my mother and my sister. Thanks for your unwavering support and your warming love from across the Alps.

Data Archiving

The measured raw data, the data processing files, and the original figure files utilized in this thesis can be reached via the Data Archive Server (DAS) at the Max Planck Institute of Quantum Optics (MPQ): `/afs/ipp-garching.mpg.de/mpq/lap/publication_archive/new_publications/`.

According to the thesis structure, the archive materials are divided in several folders corresponding to each chapter. This contains all of the relevant files such as: the raw data in .txt, .dat, .csv, .jpg, .png format, Python scripts in .py format and the figure in .pdf format. The structure of the archive materials is summarized in the following table as:

Figure	Folder	.txt/.dat/.csv/.png/.jpg	.py	.pdf
2.1	2	YbYAG_abs_293K, YbYAG_emi_293K	OSC_CrossSection	OSC_YbYAG
2.2	2			OSC_TD
2.3	2			OSC_KLM
2.4	2			OSC_Scheme
2.5	2	OSC_Cavity	OSC_Cavity	OSC_Cavity
2.6	2/pynlo_OSC/example/OSC	OSC_Spectrum, OSC_Time, OSC_FROG_Measured, OSC_FROG_Retrieved	OSC_Characterization	OSC_Characterization
2.7	2	OSC_PowerFluctuations	OSC_PowerFluctuations	OSC_PowerFluctuations
2.8	2	OSC_BeamPointing	OSC_BeamPointing	OSC_BeamPointing
2.9	2	OSC_M2, OSC_BP	OSC_M2	OSC_M2
3.1	3		MPCs_SVEA	MPCs_SVEA
3.2	3		MPCs_SPM	MPCs_SPM
3.3	3			MPCs_HCs
3.4	3			MPCs_CMs
3.5	3		MPCs_Steepening	MPCs_Steepening
3.6	3			MPCs_Raman
3.7	3			OldMPCs_Scheme
3.8	3/pynlo_MPCs/example/OldMPCs	PC1691, PC1611, PC1821	OldMPCs_Coatings	OldMPCs_Coatings
3.9	3/pynlo_MPCs/example/OldMPCs	OldMPC1_Spectrum, OldMPC1_Time, OldMPC1_FROG_Measured, OldMPC1_FROG_Retrieved	OldMPC1_Characterization	OldMPC1_Characterization

Figure	Folder	.txt/.dat/.csv/.png/.jpg	.py	.pdf
3.10	3/pynlo_-MPCs/example/OldMPCs	OldMPC2_Spectrum, OldMPC2_Time, OldMPC2_-FROG_Measured, OldMPC2_-FROG_Retrieved	OldMPC2_Characterization	OldMPC2_Characterization
3.11	3			OldMPCs_Scheme
3.12	3/pynlo_-MPCs/example/NewMPCs	PC1841, PC162, PC1843	NewMPCs_Coatings	NewMPCs_Coatings
3.13	3	OldMPCs_M2, OldMPCs_BP	OldMPCs_M2	OldMPCs_M2
3.14	3	NewMPCs_M2, NewMPCs_BP	NewMPCs_M2	NewMPCs_M2
3.15	3/pynlo_-MPCs/example/NewMPCs	NewMPC1_Spectrum, NewMPC1_Time, NewMPC1_-FROG_Measured, NewMPC1_FROG_Retrieved	NewMPC1_Characterization	NewMPC1_Characterization
3.16	3/pynlo_-MPCs/example/NewMPCs	NewMPC2_Spectrum, NewMPC2_Time, NewMPC2_-FROG_Measured, NewMPC2_FROG_Retrieved	NewMPC2_Characterization	NewMPC2_Characterization
3.17	3/pynlo_-MPCs/example/NewMPCs	NewMPC1_Time, NewMPC2_-Time, PC1611	NewMPC2_Simulation, sim_-param_NewMPC2	NewMPC2_Simulation
3.18	3	OldMPCs_BeamPointing	OldMPCs_BeamPointing	OldMPCs_BeamPointing
3.19	3	NewMPCs_BeamPointing	NewMPCs_BeamPointing	NewMPCs_BeamPointing, NewMPCs_BeamPointing
4.1	4			PCF_Fibers_Types
4.2	4			PCF_Scheme
4.3	4/pynlo_-PCFTPs/example/PCF	PCF_Spectrum, PCF_Time, PCF_FROG_Measured, PCF_FROG_Retrieved	PCF_Characterization	PCF_Characterization
4.4	4			SF

Figure	Folder	.txt/.dat/.csv/.png/.jpg	.py	.pdf
4.5	4			SF_Cases
4.6	4	TPs_Caustic	TPs_Caustic	TPs_Caustic
4.7	4/pynlo_-PCFTPs/example/TPs	noPlate, Sapphire, Quartz, YAG, FS	TPs_Material	TPs_Material
4.8	4/pynlo_-PCFTPs/example/TPs	1_0p5, 1_1, 1_0p5_1, 1_-0p5_0p5	TPs_Thickness	TPs_Thickness
4.9	4/pynlo_-PCFTPs/example/TPs	TPs_Spectrum, TPs_Spectrum_2 TPs_Time, TPs_-FROG_Measured, TPs_-FROG_Retrieved, Calibration_1, Calibration_2,	TPs_Characterization	TPs_Characterization
4.10	4	TPs_PowerFluctuations	TPs_PowerFluctuations	TPs_PowerFluctuations
4.11	4	TPs_BeamPointing	TPs_BeamPointing	TPs_BeamPointing
4.12	4	TPS_M2, TPs_BP	TPs_M2	TPs_M2
4.13	4/pynlo_Simulation-sTPs/example/TPs	noPlate, Plate1, Plate2, Plate3, Plate4, TPs_Caustic	TPs_Simulations, sim_-param_TPs	TPs_Simulations
5.1	5			OldMPCs_THz_Scheme
5.2	5	OldMPCs_THz_2mm, OldM-PCs_THz_1mm, OldMPCs_-THz_0p2mm	OldMPCs_THz_Field	OldMPCs_THZ_Field
5.3	5	OldMPCs_THz_2mm, OldM-PCs_THz_1mm, OldMPCs_-THz_0p2	OldMPCs_THz_Spectra	OldMPCs_THZ_Spectra
5.4	5	P_peak	OldMPCs_THz_Scaling	OldMPCs_THZ_Scaling
5.5	5	Water, OldMPCs_THz_0p2	OldMPCs_THz_Water	OldMPCs_THZ_Water
5.6	5	PM	TPs_MIR_Spectra	TPs_MIR_PM
5.7	5			TPs_MIR_Scheme

Figure	Folder	.txt/.dat/.csv/.png/.jpg	.py	.pdf
5.8	5	TPs_MIR_2mm, TPs_MIR_-1mm, TPs_MIR_0p3mm, TPs_MIR_BP	TPs_MIR_Spectra	TPs_MIR_Spectra